Comprehensive Gamma-ray Spectroscopy Studies of ^{62}Zn

LICENTIATE THESIS

Jnaneswari Gellanki
Department of Physics

LUND UNIVERSITY

2011

Comprehensive Gamma-ray Spectroscopy Studies of ^{62}Zn
Jnaneswari Gellanki

Division of Nuclear Physics
Department of Physics
Lund University
Box 118
SE-221 00 Lund
Sweden

LUNFD6(NFFR-3112)/1-73/(2011)

Typeset by the author using LaTeX 3.141592

List of included papers

PAPER I: **Characterization of superdeformed bands in ^{62}Zn**
J. Gellanki *et al.*
Phys. Rev. C **80** *051304(R) (2009).*

PAPER II: **High spin structure studies in ^{62}Zn**
J. Gellanki *et al.*
Proceedings NCNP 2011 - Accepted for Phys. Scr. T.

PAPER III: **Extensive γ-ray spectroscopy of rotational band structures in $^{62}_{30}$Zn$_{32}$**
J. Gellanki *et al.*
To be submitted to Phys. Rev. C.

Contents

Chapter 1

Introduction

1.1 High-Spin Physics

The atomic nucleus is a quantum mechanical many body system. To understand such a system is the challenging task in nuclear physics. The discovery in 1911 by Ernest Rutherford and his group found that almost all of the mass in an atom is made up from the protons and neutrons, and the contribution from the orbiting electrons is very small. The arrangement of the electrons outside the nucleus gives the chemical properties of a substance, whereas the arrangement of nucleons inside the nucleus determines the stability of the nucleus.

The nucleons (proton and neutrons) occupy well-defined orbitals inside the nucleus, which specify the energy, angular momentum and the different modes of shapes of the nucleus. Since the nuclear forces are strong and short range, a nucleon will only interact with neighbouring nucleons. So the nucleons inside the nucleus are tightly bound, whereas the nucleons on the surface are lightly bound. A nucleus with magic numbers, 2, 8, 20, 28, 50, 82 and 126 protons or neutrons, is usually more stable than neighbouring nuclei. By adding valence nucleons or valence holes relative to a shell closure, nuclei start to become deformed. The high-spin states of atomic nuclei refer to the quantal states with high angular momentum. In case of spherical or nearly spherical nuclei, these states are formed from the alignment of spin vectors of excited particles step by step, which leads to an irregular level structure. The case with deformed nuclei, where a group of nucleons is involved in nuclear rotation, is generally referred to as collective motion. Here, the entire nucleus can rotate about an axis perpendicular to the symmetry axis, leading to a regular level structure, with a rotational energy which is approximately a quadratic function of angular momentum.

Some of the ”hot topics” in the high-spin study of nuclei are, for example, shape coexistence, superdeformation, band termination and octupole correlations. The present work on ^{62}Zn involves some of the mentioned phenomena like band termination and superdeformation. Some details on these phenomena are reported below.

1.1.1 Band Termination

The interplay between collective and non-collective degrees of freedom is important at high-spin studies. According to the mean-field approximation, each nucleon occupies a well-defined orbital. For a fully paired spherical core, the total angular momentum contribution

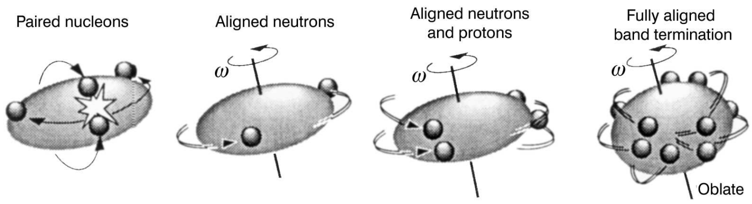

Figure 1.1: Schematic illustration of the building of angular momentum in a rotational band from the collective rotation to non-collective terminating state. Figure taken from [1]. See text for details.

Figure 1.2: Possible nuclear shapes in the $A \sim 60$ mass region. Picture taken from [2].

from the core is almost vanishing. Here, the addition of valence nucleons can only contribute a finite amount of angular momentum. The maximum spin will be determined by the maximal coupling of the single-particle spins for the particles outside the inert core.

Nuclei which have a small number of valence nucleons outside the core will have a small collectivity. On the other hand, a higher number of nucleons outside the core will lead to high collectivity at low or intermediate spin values. At rapid rotation of the nucleus, a combination of classical mechanical forces, like Coriolis and centrifugal, can break the pairs of valence nucleons and align the spin vectors of the individual nucleons along the rotational axis, in accordance with the Pauli exclusion principle. For high angular momentum, more valence nucleon pairs need to be broken. Once all nucleons are aligned along the rotational axis, they tend to polarize the nucleus towards an oblate shape, corresponding to a non-collective state. So, the nuclei evolve from collective rotation at low or medium spin to a non-collective or single-particle mode at high-spin corresponding to a " band termination" [1]. Figure 1.1 shows the building of angular momentum in a rotational band ending up in a fully aligned terminating state. Here, the motion is collective at low-spin with paired nucleons, while at intermediate spin, nucleon pairs are broken and start to align their spin vectors along the rotational axis and finally, at high-spin, fully aligned nucleons which is called a terminating state. Band termination is normally referred to as a specific nucleonic configuration. Different configurations can terminate at different I_{max} spin states. At large deformations, sometimes the specific band configuration may not terminate due to mixing between j-shells [3, 4].

1.1.2 Superdeformation

Figure 1.2 illustrates possible shapes experimentally found or predicted by theoretical models in the $A \sim 60$ mass region. They range from spherical nuclei to quadrupole deformed,

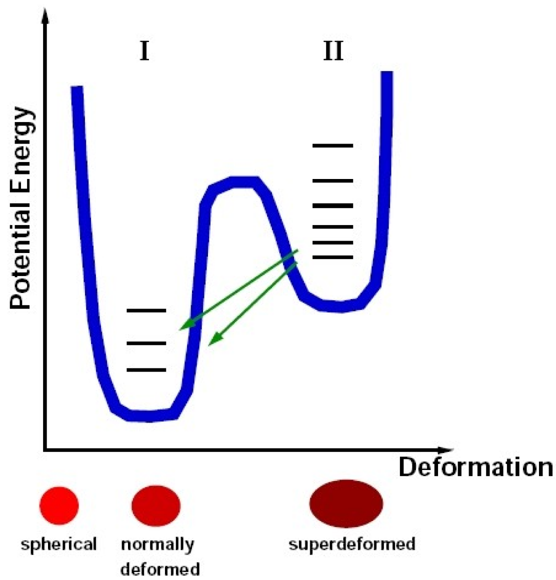

Figure 1.3: The potential energy of a nucleus versus the deformation. Picture taken from [6].

highly and superdeformed (SD) nuclei. At fast rotation, some nuclei prefer elongated shapes having an axial deformation corresponding to a major-to-minor axis ratio $\sim$ 2:1. These are called superdeformed nuclei, and have large quadrupole moments. The existence of superdeformed shapes in nuclei was first time observed at low-spin in actinide fission isomers [5].

The regions where superdefomed nuclei have been observed are those nuclei with proton and neutron numbers which correspond to large shell gaps at large prolate deformation in the deformed shell-model potential. Theoretical existence of SD structures was explained by the existence of secondary energy minima in the nuclear potential energy surface at a higher quadrupole deformation than the nuclear ground state. Figure 1.3 shows the separation of the first and second minimum of the nuclear potential by an energy barrier. The linking transitions between SD bands and normal deformed (ND) states can be used to determine the fundamental properties of the SD states, like spin, parity and excitation energy. The decays within superdeformed bands are experimentally characterised by very fast and long cascades of regularly spaced $E2$ transitions. These decay transitions correspond to large $\mathcal{J}^{(2)}$ moments of inertia, and highly collective and large transitional quadrupole moments. The linking transitions are very difficult to observe due to their low intensity. So far more than 300 superdeformed rotational bands have been observed and studied in different regions across the nuclear mass range. For instance, in each of the mass regions, $A \sim 40$ [7], $A \sim 60$ [8], $A \sim 80$ [9], $A \sim 110$ [10], $A \sim 130$ [11], $A \sim 150$ [12] and $A \sim 190$ [13] superdeformed bands have been observed.

1.1.3 Why $A \sim 60$ mass region interest

An interesting feature in the $A \sim 60$ mass region is that the same nuclei can exhibit various kinds of the nuclear high-spin phenomena, like band termination, highly deformed bands, superdeformed bands, prompt proton decays and shape changes [14, 15, 16, 17, 18]. To generate the high-spin states required for the observation of most of the collective phenomena, it is necessary to break the $N = Z = 28$ core and to excite nucleons into the intruder $1g_{9/2}$ subshell. Starting at normal deformation (ND) with a few particles in the upper fp shell outside the doubly magic $N = Z = 28$ ^{56}Ni core, the nuclei in this mass region become highly deformed and superdeformed (SD), when the number of holes in the $1f_{7/2}$ orbital and particles in the $1g_{9/2}$ orbital rapidly increase with spin and excitation energy. The superdeformed band in ^{60}Zn [19] built on the SD shell gaps at $N = Z = 30$, is treated as doubly-magic SD core in the $A \sim 60$ region.

For the rotational sequences of the nuclei in the $A \sim 60$ mass region, one can expect "smooth band termination" [20] with a smaller number of valence particles than in the heavier nuclei. The "smooth band termination" was first discovered in the $A \sim 110$ [21] mass region. It is characterized by a continuous transition within one configuration from large collectivity at low or intermediate values to a non-collective terminating state at the highest possible spin value. The nuclei in the $A \sim 60$ mass region exhibit a variety of excitations, both single-particle and collective with different shapes, namely prolate, oblate and triaxial. In contrast to the other mass regions, almost all superdeformed bands in the second minima of nuclear potential can be connected with the normal deformed, or spherical states in the first minimum of the nuclear potential. There are some differences between the $A \sim 60$ mass region and other heavy mass regions. For example, in the $A \sim 190$ mass region, the observed decay-out is dominated by $E1$ transitions expected in a statistical decay process, whereas in the $A \sim 60$ mass region, the observed decay-out transitions are mainly of stretched $E2$ character with a non-statistical mechanism [19]. Superdeformed nuclei in this mass region are also of interest because they are the fastest rotating nuclei ($\hbar\omega \geq 2.0$ MeV). They are self-conjugate or nearly self-conjugate, which allows the investigation of isospin sensitive properties in SD nuclei.

Chapter 2

Experimental Tools

2.1 Fusion-evaporation Reactions

Nuclear high-spin and superdeformed states are populated experimentally in fusion-evaporation reactions. When a beam particle hits a target nucleus, two nuclei can fuse with a certain probability and form a compound nucleus. The fusion process will occur only if the incident kinetic energy of the beam particles is higher than the Coulomb barrier in order to overcome the Coulomb repulsion between two positively charged nuclei. The kinetic energy of the collision in the center of mass frame is partly converted into excitation energy of the compound system. The amount of angular momentum transferred to the compound nucleus is simply $l = mvb$, where mv is the linear momentum of the beam particles and b is the impact parameter. Thus higher incident beam energies result in larger angular momentum transfer to the compound system. Figure 2.1, shows the process of the fusion-evaporation reaction.

A highly excited compound nucleus is formed with the excitation energy

$$E_{ex} = E_{CN} + Q \tag{2.1}$$

where Q is the Q value of the reaction and E_{CN} is the kinetic energy of the collision which is transferred to the compound system. It is calculated from the formula

$$E_{CN} = E_B(\frac{M_T}{M_T + M_B}) \tag{2.2}$$

where E_B is the kinetic energy of the beam, while M_B and M_T are the masses of the beam and target nucleus, respectively. The maximum angular momentum, l_{max}, that can be transferred to the compound nucleus is

$$l_{max} = \sqrt{2}(\frac{R}{\hbar})(\sqrt{\mu(E_{CN} - V_c)}) \tag{2.3}$$

where R is the maximum nucleus-nucleus distance for which a reaction can occur. The reduced mass of the system μ, is given by

$$\mu = \frac{M_B M_T}{M_B + M_T} \tag{2.4}$$

and V_c is Coulomb barrier energy. The present study is mainly based on data from a fusion-evaporation reaction using a 122 MeV ^{28}Si beam on a ^{40}Ca target, which gives the compound

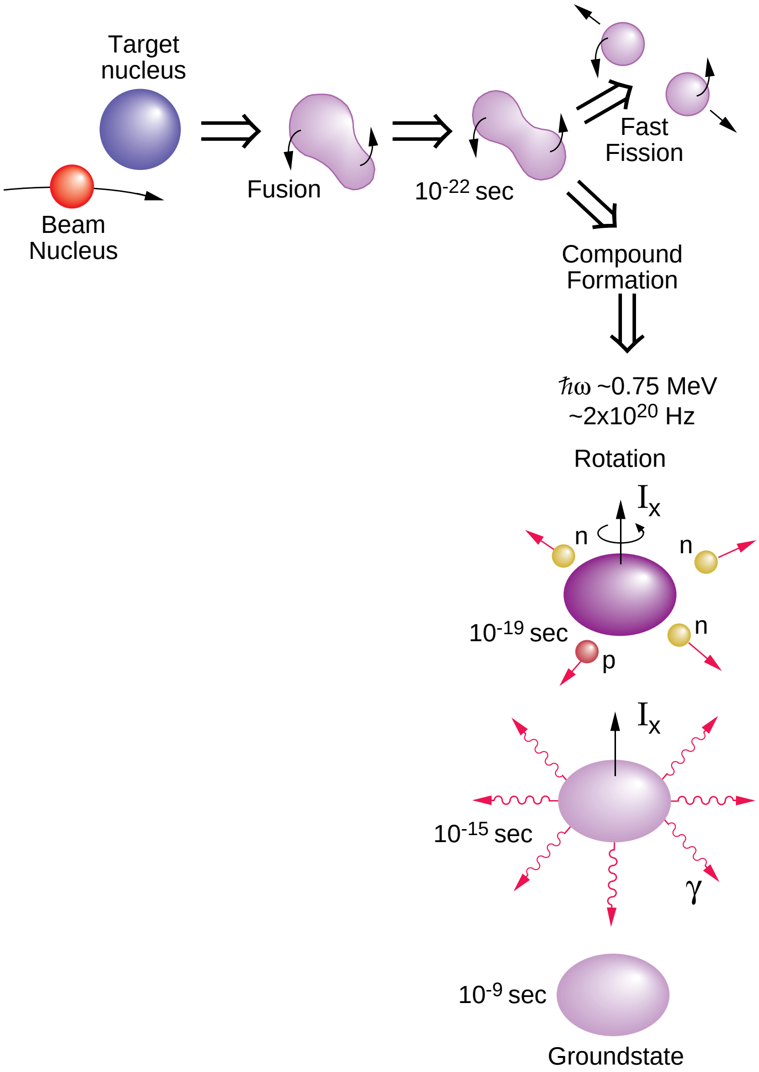

Figure 2.1: Schematic drawing of the fusion evaporation reaction process. Picture taken from [22].

nucleus ^{68}Se. The Q value for this reaction is -2 MeV and using Eq. 2.2 we get $E_{CN} \approx 71$ MeV. The excitation energy of the compound nucleus then becomes ≈ 69 MeV and the maximum angular momentum, l_{max}, that can be transferred to the compound nucleus is 42 $\hbar$.

The compound nucleus which is at high excitation energy, cools down by evaporating light particles such as protons, neutrons and α-particles leading to different residual nuclei. The cooling process is an efficient way of reducing the excitation energy in the compound nucleus, since the evaporated particles take away energy from the compound system for example, α particles take away ≈ 15 MeV, protons ≈ 6 MeV and neutrons ≈ 2 MeV. The species of the residual nuclei depend on the appropriate kind and number of evaporated particles. The overall time taken for this process is approximately 10^{-19} s. Since the evaporated light particles can only carry away a few units of angular momentum, the residual nucleus is typically left in an excited state with high angular momentum at large excitation energy.

In the neutron deficient $A \sim 60$ region, the evaporated protons and α-particles are more likely to be emitted than neutrons. This is due to the higher neutron separation energy of $\approx$ 15 MeV, compared to the proton separation energy of $\approx$ 5 MeV. In our study, the compound nucleus ^{68}Se evaporates one α and two proton particles leading to the nucleus of interest ^{62}Zn. The highly excited residual nucleus de-excites to the ground state by sending out first statistical and then, as the nucleus approaches the yrast line, discrete γ-rays. The yrast line is the line connecting the yrast states. The yrast state is the lowest energy state for a given value of angular momentum. The time scale for the nucleus to reach its ground state is about 10^{-9} s, as long as the decay does not follow any long lived, isomeric states. The discrete γ-rays are detected in the experiment making it possible to find out the nuclear structure properties of residual nuclei.

2.2 Gamma-Ray Detection

Germanium detectors are a popular choice for resolving the collection of γ-rays emitted from the residual nuclei of interest because of their high energy resolution. In the mass $A \sim 60$ region the interesting γ-rays energy is ranging from 0.1 MeV to 6.0 MeV. Cylindrically closed ended coaxial shaped Ge detectors are most frequently used as opposed to planar and open-ended coaxial shaped detectors. The sensitive volume in the former one is larger than in the other two, resulting in smaller leakage current at the front surface of the detector [23]. Normally, for a cylindrically shaped Ge detector with diameter and length of 7-9 cm, the energy resolution is about 2 keV at an incident γ-ray energy of 1 MeV.

The three major interaction mechanisms of γ-rays in matter are photoelectric absorption, Compton scattering and pair production. In all these interactions the incident γ-ray photon transfers its energy partially or completely to an electron or a positron which transfer their kinetic energy to the detector material. Photoelectric absorption is favoured for low-energy γ-rays, whereas pair production is favoured for high-energy γ-rays, and Compton scattering lies in between these energy extremes [23].

In the photoelectric absorption the incident γ-ray photon is completely absorbed in the germanium crystal and disappears. In a Compton scattering process the incident γ-ray photon transfers a portion of its energy to the germanium crystal electrons. The remaining part can escape the detector volume. This escaped photon energy results in a large Compton continuum background events. A BGO ($Bi_4Ge_3O_{12}$) shield around the Ge detector can be used to suppress this background. This shield acts as a veto for Compton events which scatter out of the germanium detector. If the γ-ray energy exceeds 1.02 MeV, i.e twice the rest mass energy of an electron, then the pair production process is energetically possible. In this interaction, the γ-ray photon disappears and the excess energy carried in by the photon above 1.02 MeV appears in the form of kinetic energy shared by the electron-positron pair.

Practically, it is impossible to measure all of the individual γ-rays in a cascade with 100% efficiency. Recently, over the last few years this problem has been minimized by using modern germanium detector arrays such as GAMMASPHERE [24], EUROBALL [25] and GASP [26]. The present data analysis with the ^{62}Zn nucleus has been studied with the GAMMASPHERE array.

Figure 2.2: Ge detectors in the Gammasphere array [24]. Picture taken from [22].

2.3 GAMMASPHERE

The Ge-detector array, GAMMASPHERE, is presently located at Argonne National Laboratory in the U.S.A. At the time of the experiment the array contained 103 high purity germanium detectors shielded by Compton-suppressing BGO detectors. The Ge detectors are arranged in a 4π geometry. Figure 2.2 shows the structure of the array. If the γ-ray multiplicity is high, it is possible that two, or more, emitted γ-rays hit the Ge detector and its surrounding BGO shield at the same time. The BGO detector will then veto a good event. To minimise this possibility Heavimet absorbers can be placed in front of the BGO detectors. The Gammasphere array has a full-energy peak efficiency of $\sim 9\%$ at a γ-ray energy of 1.33 MeV, and the overall energy resolution is typically about 2.6 keV at the same γ-ray energy.

2.4 Charged Particle Balls

For a very neutron deficient compound nuclear system, it is easier for protons and α-particles to tunnel through the Coulomb barrier due to their small separation energies compared to the compound nuclei closer to stability. This means that the emission of charged particles will dominate over neutron emission. This leads to the population of a large number of different nuclei with different cross sections in a single reaction. In order to detect the particular nuclei of interest, reaction channel selection methods are used. The main job of channel selection methods is the selection of a specific reaction channel by gating on the appropriate

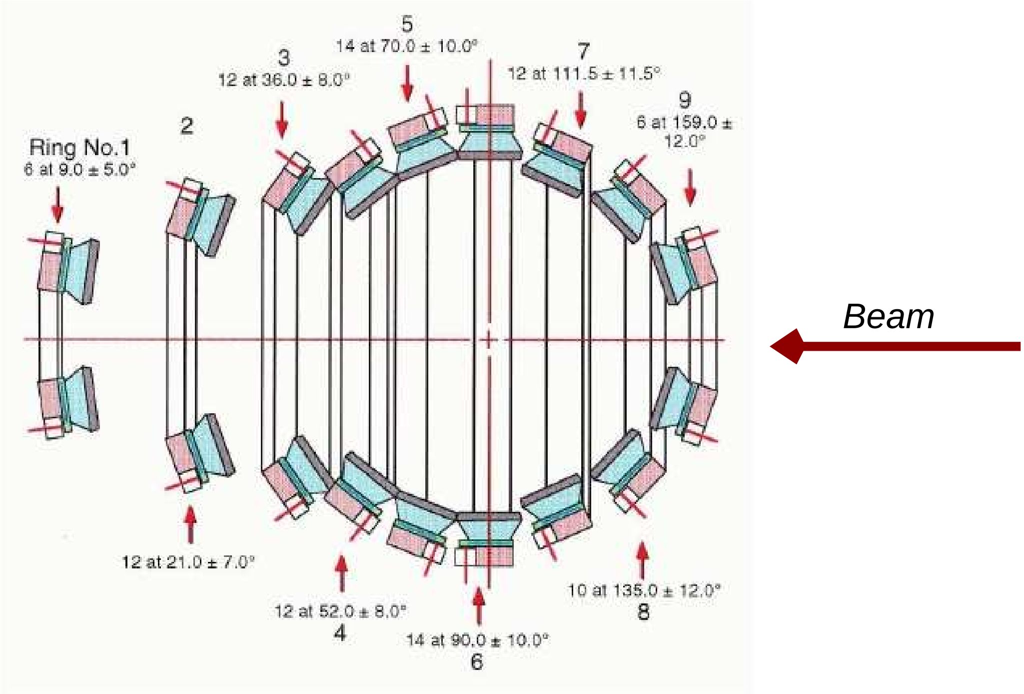

Figure 2.3: Schematic drawing of the CsI Microball detector array. Picture taken from [28].

kind and number of evaporated particles. For this purpose, charged particle balls are used to detect and discriminate evaporated charged particles from the compound nucleus.

2.5 Microball

Scintillation detectors are often used for charged-particle detection due to their large light output with high efficiency. Microball is a scintillator detector array consisting of 95 CsI(Tl) elements which are situated in 9 rings in a 4π geometry (see Fig. 2.3). The array is located in the center of GAMMASPHERE. The 9 rings of detectors cover the angles between 4.0° and 171° with respect to the beam axis. The reaction kinematics produces particles which are strongly focused at forward angles. Therefore, the two most forward rings of detectors are positioned at large distances from the target resulting in a higher granularity. The Microball detector measures the energies and the directions of the emitted charged particles. The charged particles are discriminated by pulse shape techniques [27]. CsI(Tl) detectors provide different decay times for evaporated charged particles. The decay time from the CsI(Tl) detector has a slow and fast component, where the latter but not the former depends on the detected particle type. A charge ratio is measured between these components which is thus used to separate the charged particles [6]. The average total efficiency of Microball in the present experiments is about 80% for protons and 70% for α- particles. Thick Pb or Ta absorber foils were placed in front of the CsI(Tl) detectors to stop heavy high-energy particles, like scattered beam and target particles.

2.6 Overview of the Experiments

The γ-ray transitions of the ^{62}Zn nucleus under study were resolved by using the combined statistics of four different experiments performed at Argonne and Lawerence Berkelery National Laboratories. These transitions were used to construct the level scheme of the nucleus. A brief overview of the experiments is given in Table 2.1. More detailed explanations about these experiments are given in [15, 17, 29, 30, 31].

Table 2.1: Details of the fusion-evaporation reaction experiments which the present work is based on.

GSFMA66	GS54	GSFMA42	GSFMA138
^{28}Si+ ^{40}Ca	^{36}Ar+ ^{28}Si	^{36}Ar+ ^{28}Si	^{36}Ar+ ^{28}Si
E_B = 122 MeV	E_B = 143 MeV	E_B = 148 MeV	E_B = 134 MeV
Compound nucleus (CN): ^{68}Se	CN: ^{64}Ge	CN: ^{64}Ge	CN: ^{64}Ge
channel: 1α 2p	channel: 2p	channel: 2p	channel: 2p
Gammasphere(103 Ge)	Gammasphere(82 Ge)	Gammasphere(86 Ge)	Gammasphere(77 Ge)
Microball	Microball	Microball	Microball
	neutron detectors	neutron detectors	neutron detectors
		Si- strip detectors	Si- strip detectors
$\sigma_{rel} \approx 30$ %	$\sigma_{rel} \leq 1\%$	$\sigma_{rel} \leq 1\%$	$\sigma_{rel} \leq 1\%$

2.6.1 GSFMA66 Experiment

The 0.5 mg/cm^2 thin ^{40}Ca target was enriched to 99.975 %. It was sandwiched between two thin layers of Au to prevent oxidation. The beam consisted of ^{28}Si and was accelerated to an energy of 122 MeV. In this reaction the compound nucleus was ^{68}Se, and ^{62}Zn was populated in the 1α2p channel. The experimental setup consisted of the Gammasphere array in conjunction with the Microball array. The Heavimet collimators were removed from the Ge detectors to enable γ-ray multiplicity and sum-energy measurements [32] and additional channel selectivity based on total energy conservation requirements [33]. No neutron detectors were used in this experiment.

The population cross section for the ^{62}Zn nucleus is $\approx 30\%$ of the total cross section. The statistics from this experiment is called data set 1. This experimental data is the primary source used to construct the level scheme of ^{62}Zn, i.e it is used to identify the different structures and rotational bands, including the superdeformed bands and their decay-out transitions.

2.6.2 GS54, GSFMA42, GSFMA138 Experiments

All three experiments utilize fusion-evaporation reactions with the same beam, ^{36}Ar, and target nuclei, ^{28}Si, and similar beam energies, $\sim$ 140 MeV. Evaporated charged particles were detected in different combinations of charged-particle detectors. The relative yield for ^{62}Zn is very small in these three experiments. The combined statistics of these data sets is called data set 2, and was used to add the highest-spin states of the superdeformed bands.

Chapter 3

Data Analysis Tools

3.1 Energy Calibration Sources

Energy calibration of a detector is the process of determining the energies of the unknown with known energy sources. Different types of calibration sources were used in the experiments mentioned in Section 2.6 in Table 2.1. The energy and efficiency calibrations of the GAMMASPHERE detectors were done using γ-ray energies from ^{56}Co, ^{133}Ba, ^{152}Eu and ^{228}Th γ-ray sources. The Microball detector calibration has been made by using the peaks produced from the elastic scattering of a beam of protons and α-particles with energies 12 and 48 MeV on ^{197}Au and inelastic scattering of the same beam energies on a ^{12}C target.

3.2 $\gamma\gamma$ and $\gamma\gamma\gamma$ Coincidence Analysis

The events in all the specified experiments in Table 2.1, were sorted offline into various E_γ projections, $E_\gamma - E_\gamma$ correlation matrices and $E_\gamma - E_\gamma - E_\gamma$ cubes subject to appropriate evaporated-particle conditions. Gating $E_\gamma - E_\gamma$ matrices create a spectrum containing the γ-rays which are in coincidence with the transition chosen to be gate. These matrices contain a large amount of statistics but they generally comprise a high background level due to doublets or some remaining contamination from other reaction channels. In the case of the $E_\gamma - E_\gamma - E_\gamma$ cube, the gated spectrum contains the coincidence events with two γ-ray transitions which are also in coincidence with each other. The triple coincidences naturally result in a cleaner analysis but require a larger amount of events. The present analysis was restricted to events in which all of the evaporated charged particles, that is, two protons in the case of data set 2 and an additional α particle for data set 1, were detected. For data set 1, in total $2 \cdot 3 \cdot 10^9$ coincidence events were collected, with a $\gamma\gamma\gamma\gamma$ trigger condition.

Figure 3.1 shows the coincidence γ-ray spectrum resulting from the γ-ray gate on the 1232 keV transition, which depopulates the state at an excitation energy 2186 keV in ^{62}Zn. The spectrum is created via the $E_\gamma - E_\gamma$ matrix. The ground state γ-ray transition at 954 keV has the highest coincidence rate with the 1232 keV transition. Other intense transitions at 557, 910, 1161, 1177, 1197, 1340, 1522, 1586, 1604, 1791 and 1857 keV are marked. Several low intensity coincidences are also clearly visible in the figure.

The study of ^{62}Zn relies on a $\gamma\gamma\gamma$ cube created with data set 1 and analyzed with the RADWARE analysis package [34]. To confirm low-intensity or ambiguous transitions, certain parts of the decay scheme are focused on during the analysis by specific $\gamma\gamma$ matrices,

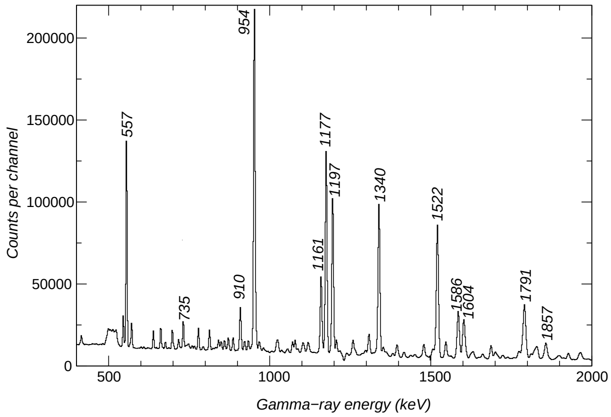

Figure 3.1: Coincidence γ-ray spectrum with a transition at 1232 keV, which depopulates the state at an excitation energy of 2186 keV in ^{62}Zn. See text for details.

which are preselected by γ-rays originating from a certain rotational band or decay sequence within the complex ^{62}Zn excitation scheme. For data set 2, a $\gamma\gamma$ matrix was created, which focuses on the high-lying entry states in ^{62}Zn by requiring at least 14 detected γ rays with at least an energy of 16.5 MeV total energy and less than 19 MeV particle energy [31]. For the γ-ray spectrum analysis, the code TV developed at the University of Cologne [35], was used in the current analysis.

3.3 Doppler Shifts and Doppler Broadening

When the recoiling nuclei emit γ-rays, the energies will be Doppler shifted. The shifted energy, $E_\gamma(\theta)$, is related to the unshifted energy, E_0, by the relation

$$E_\gamma(\theta) = E_0(1 + (v/c)\cos\theta) \tag{3.1}$$

Here v is the recoil velocity of the nucleus of interest and θ is the first approximation angle at which the γ ray is emitted, i.e. the detector position relative to the beam direction. The shift is largest for the most forward and backward angles, while there is no shift at $\theta = 90°$. The recoil velocity of the nucleus, v, in the laboratory frame is typically a few percent of the velocity of light, c.
The finite opening of the γ-ray detector leads to a Doppler broadening. If the opening angle of the detector is $\Delta\theta$, then the partial derivative of Eq. 3.1 gives

$$\Delta E_\gamma = E_0(v/c)\sin\theta\Delta\theta \tag{3.2}$$

The Doppler broadening is maximum for $\theta = 90°$. The Doppler broadening can be minimized by using segmented Ge detectors, where the effective solid angle $\Delta\theta$, is reduced at the front face of the detector.

Another considerable contribution to the Doppler shift arises from the velocity variation of the recoiling nuclei due to energy-loss straggling of the projectiles in the target, as well as the emission of evaporated particles (see Sec. 3.4). It means that the recoiling nuclei have different velocity vectors from the velocity along the beam axis. Since the corresponding

Doppler shift depends on the detector angle as $\cos\theta$, this is most important for detector angles close to 0° and 180°.

The feeding times of low-spin yrast nuclear states are generally slow ($\approx 10^{-10}$s), and their decays take place outside the target where a proper velocity distribution is defined for the recoiling nuclei. In this case the Doppler shift can be corrected for using the average velocity. On the other hand the superdeformed states or highest spin states may decay while still in the target material due to their very short lifetimes and feeding times. This causes larger and variable Doppler shifts which requires additional Doppler corrections compared with the γ-rays emitted by low-spin yrast states.

3.4 Kinematic Corrections for Doppler Effects

The velocities and directions of the evaporated charged particles from the compound nucleus change the velocity and direction of the recoil nucleus. This may result in worsened energy resolution of the γ-ray detected mainly in the thin target experiments, in which the target material does not have any backing foils to stop the recoils. This problem is more prononuced for neutron-deficient nuclei which are formed by emission of α-particles.

This problem has been tackled by measuring charged particle energies and angles with the Microball detector array, and thereby defining the momenta of the recoiling residual nuclei for each event. Thus the change in direction and velocity of the recoil due to the charged particle emission can be calculated, and used to improve the γ-ray energy resolution. More details are given in [6, 36].

In addition, the γ-rays originating from the SD bands and highly deformed rotational bands are likely to be emitted while the residual ^{62}Zn nuclei are still slowing down inside the thin target foil. Assuming an average deformation of the rotational bands in ^{62}Zn and simulating the slowing-down process in the thin target layer, so called additional fractional Doppler shifts can be derived as a function of γ-ray energy [37]. Taking this into account, a more accurate Doppler-shift correction of the γ-rays originating from deformed structures can be obtained.

3.5 Channel Selection Methods

Because of the existence of several exit channels with significant population cross sections of residual nuclei in the mass $A \sim 60$ region, one should use specific channel selection methods in order to eliminate the competing reaction channels and to improve the total peak-to-background ratio of the γ-ray spectra belonging to the specific nuclei of interest. The most basic employed channel selection method is the gating on the number of evaporated particles in the specific reaction channels. More details on this method are already discussed in section 2.4.

The charged-particle gating method is not good enough to use, where the higher particle multiplicity channels with larger cross-sections dominate over the low particle multiplicity channel with less population cross section. In order to overcome these difficulties in a study of weakly populated channels, a method called Total Energy Gating (TE- Gating) was introduced in [33]. This method is based on the γ-ray multiplicity and sum-energy measurements [32].

The main concept of the TE-gating method is that the total energy of the γ rays and emitted particles should essentially be constant for all events, as the compound nucleus always obtains approximately the same energy. The total energy for a given reaction channel, E_{CN}, is given by $E_{CN} = H_\gamma + T_{part}$, where H_γ is the total γ-ray energy and T_{part} is the total kinetic energy of the emitted partciles. Because E_{CN} is constant for a given channel, a plot of the total particle kinetic energy vs the total γ-ray energy gives information about the events corresponding to a specific channel. In this plot a non-identified particle will lead to a too low value of parameter T_{part}. The TE-gating can hence discard such an event.

Figure 3.2 shows a schematic Total Energy Plane (TEP). Only events with one α- particle

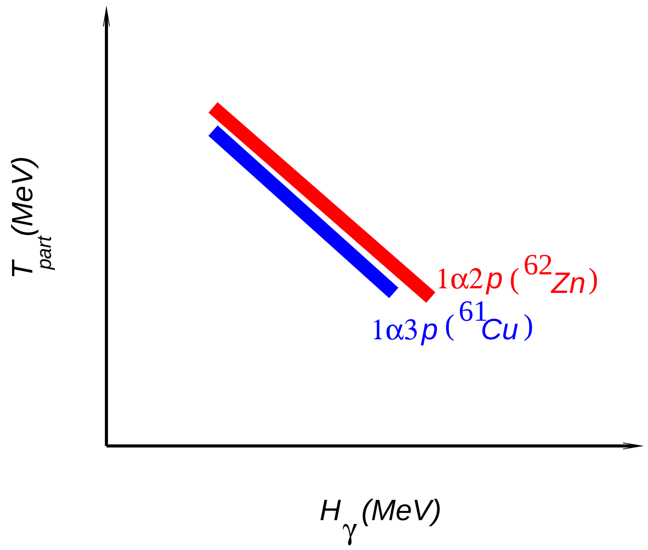

Figure 3.2: Schematic Total Energy Plane (TEP) for events in coincidence with one α and two protons detected in Microball. Here the red line indicates the events corresponding to the $1\alpha2p$ channel (where ^{62}Zn is populated), while the blue line shows events in the $1\alpha3p$ channel (where ^{61}Cu is populated) and one proton escaped detection.

and two protons detected in Microball are considered. The events corresponding to $1\alpha2p$ channel ^{62}Zn are lying on the red line, whereas the events belong to the $1\alpha3p$ channel ^{61}Cu are expected on the blue line. Now, consider a $1\alpha3p$ event that appears in the $1\alpha2p$-gated data because one of the protons was missed. First, as seen from the position of the two lines, the total energy for the $1\alpha3p$ channel is smaller than that for the $1\alpha2p$ channel by the binding energy of the third proton. Secondly, the kinetic energy of the missed proton is absent from the T_{part}. Therefore, if only events along the red line in Fig. 3.2 corresponding to ^{62}Zn are accepted, the contamination from ^{61}Cu can essentially be eliminated.

3.6 DCO Ratios

Assignments of spin and parity of the excited levels were based on the analysis of 1α2p-gated directional $\gamma\gamma$ correlations of oriented states (DCO ratios). The Ge-detectors of Gammasphere were grouped into three ”pseudo” rings called ”30”, ”53”, and ”83”, which correspond to an average angle for the respective sets of detectors while accounting for γ-ray emission symmetry with respect to the $90°$- plane perpendicular to the beam. Three combinations of angles were chosen and sorted into matrices, namely (30 - 83), (30 - 53), and (53 - 83); for instance, for the (30 - 53) matrix, γ rays detected at $30°$ were sorted on one axis and those detected at $53°$ placed on the other axis of the correlation matrix.

The DCO ratios for almost all experimentally observed γ-rays in ^{62}Zn could be determined with the (30- 83) $E_\gamma - E_\gamma$ matrix. In this matrix, the experimental DCO ratios were extracted [38] according to the formula

$$R_{DCO} = \frac{I(\gamma_1 \text{ at } 30°;\ \text{gated with } \gamma_2 \text{ at } 83°)}{I(\gamma_1 \text{ at } 83°;\ \text{gated with } \gamma_2 \text{ at } 30°)}.$$

The intensities I were extracted from a $1\alpha 2p$- and TE-gated γ-γ matrix with γ-rays detected at 30° sorted on one axis and 83° on the other axis of the matrix. The list of DCO ratios for the γ-ray transitions observed in ^{62}Zn is given in paper III, Table 1 [18]. The DCO ratios of some of the γ-rays could not be measured, mainly because of their low intensities. The DCO ratios for the (30- 53) and (53- 83) matrices are defined accordingly.

Typical values for R_{DCO}, when gating on a stretched E2 transition, are

$$\begin{aligned}
&R_{DCO} = 1.0 \text{ for } E2 \text{ transitions;}\\
&R_{DCO} \sim 0.9 \text{ for } \Delta I = 0 \text{ transitions;}\\
&R_{DCO} \sim 0.6 \text{ for stretched } \Delta I = 1 \text{ transitions.}
\end{aligned}$$

However, ΔI = 1 transitions can show deviations from the expected value due to quadrupole admixtures, i.e., nonzero $\delta(E2/M1)$ mixing ratios. $M2$ and higher order than quadrupole transitions are neglected due to their low probabilities.

An analysis of the mixing ratios, $\delta(E2/M1)$, was performed for several $\Delta I = 1$ transitions based on DCO-ratios arising from the three different angle combinations. The phase convention of Rose and Brink [39] is used for the mixing ratios. The alignment coefficients, α_2 were estimated through the relation [40].

$$\alpha_2 = 0.55 + 0.02 \cdot E_x \text{ [MeV]}, \Delta\alpha_2 = \pm 0.05 \tag{3.3}$$

Figure 3.3 shows two spectra in coincidence with the gating transition at 1586 keV, corresponding to the $16^+ \rightarrow 14^+$ ($E2$ transition) of structure ND6b. The spectrum in panel (a) is obtained by gating on the y-axis (83°) and projecting the coincident events onto the x-axis (30°). The spectrum in panel (b) is produced in the opposite way. The transitions at, for example, 954, 1232, 1340, 1522 and 1791 keV have stretched $\Delta I = 2$ character, which can already be seen by observing that these transitions have basically same intensity in the spectra of both panel (a) and (b) ($R_{DCO} \approx 1.0$). The R_{DCO} value of a γ-ray transition is obtained by fitting the peaks present in each spectrum, dividing their intensities and then correcting the result with the γ-ray efficiency. The peaks at 557 and 1161 keV which are marked in blue, have known pure electric dipole character. For these peaks the intensities are higher in panel (b) than in panel (a). The peak at 1821 keV corresponds to a mixed $E2/M1$ character, R_{DCO}(1821) = 0.35(3).

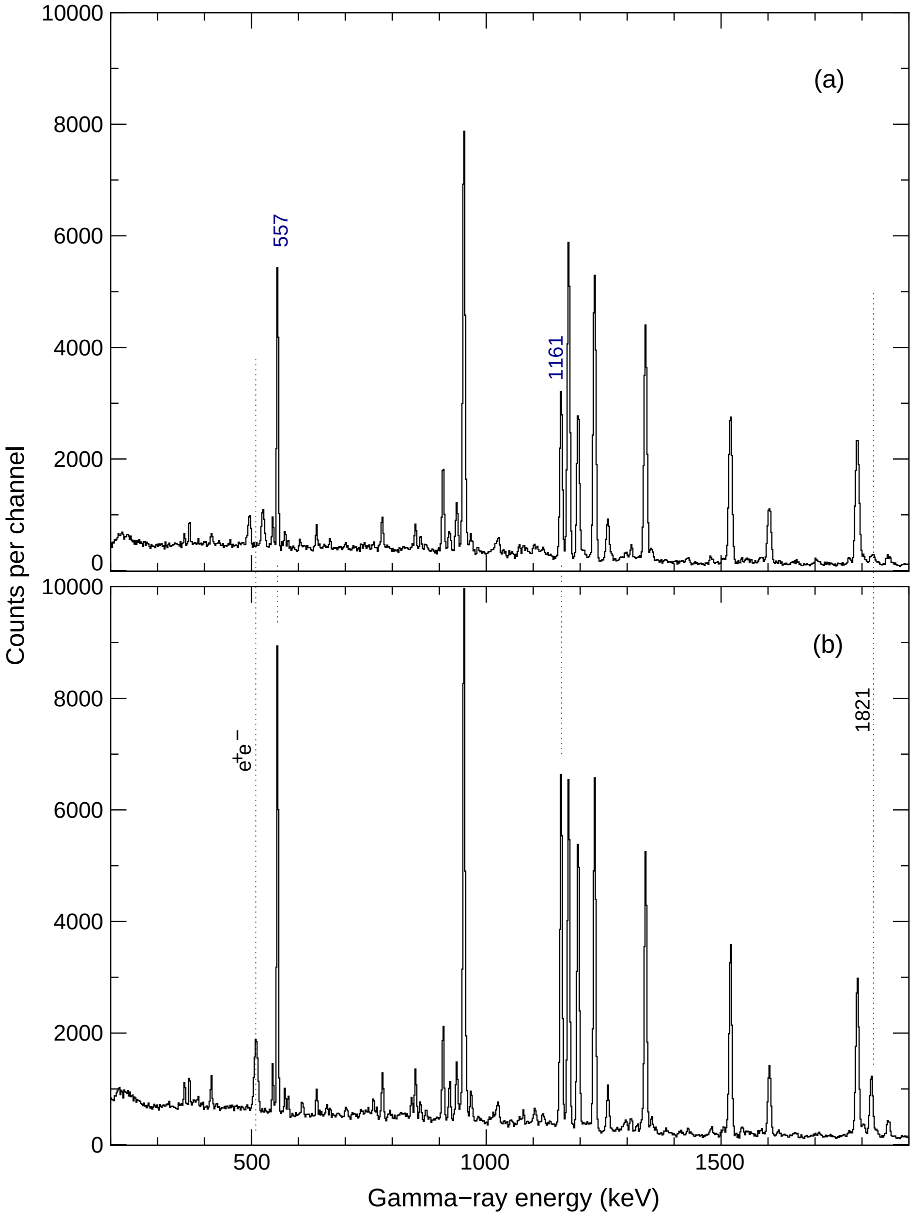

Figure 3.3: γ-ray spectra in coincidence with the $16^+ \rightarrow 14^+$ yrast transition at 1586 keV. (a) Gating on the y-axis (83°) and projecting the events onto the x-axis (30°). (b) Gating on the x-axis (30°) and projecting the events onto the y-axis (83°). See text for details.

Chapter 4

Results on ^{62}Zn

Previously, high spin states in ^{62}Zn have been studied in [8, 20, 41, 42, 43, 44, 45]. The present level scheme of ^{62}Zn was established by using the combined statistics of four different experiments. It is shown in Fig. 4.1. It was constructed on the basis of coincidence relations, intensity balance and summed energy relations. Due to the complexity of the level scheme of ^{62}Zn, each structure or rotational band labelled in Fig. 4.1 is going to be presented separately. The low-spin normal deformed part is shown in Fig. 4.2, with the labels ND1-ND9. The two previously known terminating bands are labelled as TB1 and TB2 [20]. All ′ well-deformed ′ bands are labelled WD1-WD10. The superdeformed bands are labelled SD1-SD5. In addition, the signature partner structures are noted with extra labels, 'a' for $\alpha = 1$ signature band and 'b' for $\alpha = 0$ signature band. The spin and parity assignments of the γ-ray transitions are obtained from the analysis of the DCO ratios. The DCO ratios of some of the γ-rays could not be measured, mainly because of their low intensities. The level energies, the corresponding depopulating γ-rays, their relative intensities, their angular correlation ratios, and resulting spin-parity assignments are given in [18]. The ground-state transition is normalised to 10,000 units of intensity

The spins and parities of the few normal deformed structures and for TB1 and TB2 were already known from the earlier studies [8, 20]. The DCO ratios of the transitions from these levels obtained in this experiment are in agreement with these assignments. The observed highest spin deduced from these results for states with known spin values is 24^- at $E_x = 23179$ keV [8, 20]. Our recent publication [45] revealed more information about three superdeformed bands, SD1-SD3, and one well-deformed band WD1. The observed highest spin from this study is 35^- at $E_x = 42.5$ MeV.

In the following, the different sections of the extensive new decay scheme are are introduced and discussed by means of a few selected γ-ray spectra and R_{DCO}-values. The normally deformed region is described in sect. 4.1. This region reaches up to the 15705 keV $I^\pi = 19^-$ energy level and comprises the states not included in any of the more collective structures. The two previously known terminating structures are described in sect. 4.2 and the well-deformed and superdeformed structures are briefly described in sect. 4.3. Furthermore, the high quality of data set 1, is demonstrated in sect. 4.3. The intensities of most of the γ transitions were deduced from the $\gamma\gamma$ matrices. All excited rotational bands were connected to the low-spin normal deformed states via one or more linking transitions. In most cases, this allowed for firm, but sometimes only tentative spin and parity assignments to the lowest states in the bands. The tentative spin and parity assignments to the states near the top of the bands are based on their regular rotational behaviour.

4.1 The Low-spin Normally Deformed Region

Figure 4.2 shows the low-spin normal deformed part of the present decay scheme, which adds the five new structures ND4, ND5, ND7, ND8 and ND9 in addition to the previously known structures ND1, ND2, ND3 and ND6 [20]. All the near yrast energy level assignments made in the previous works are in agreement with the present results.

4.1.1 Structures ND1 and ND2

The previously known structures were extended from the level energies at 3708 keV to 5911 keV (ND1), 5144 keV to 6965 keV (ND2a) and 4348 keV to 6445 keV (ND2b) by adding the 2203, 1821 and 2097 keV γ-ray transitions on top of the structures ND1, ND2a and ND2b, respectively. For the structure ND1, the 0^+, 2^+, 4^+ and 6^+ states were observed previously. The previously placed topmost two transitions, at 1774 keV ($8^+ \rightarrow 6^+$) and 2018 keV ($10^+ \rightarrow 8^+$), were now rearranged as side feeding transitions. The newly added transition at 2203 keV has an $E2$ behaviour. The ND1 structure is fed by strong transitions, at 557, 641 and 851 keV from the ND2b structure. The DCO values for these γ-rays are consistent with ΔI=0 character. Here, the 557 keV transition is doublet with the same energy of the $E1$ transition which depopulates the level at 4905 keV. Interestingly, these two transitions are also in coincidence with each other. However, by putting gates on different $E2$ transitions, it is possible to distinguish their multipolarities (see paper III Table 1 [18]).

The structure ND2 consists of two signature partner bands, ND2a ($\alpha = 1$) and ND2b ($\alpha = 0$). These are connected to each other via $E2/M1$ transitions at 360, 761, 796 and 843 keV. ND2a and ND2b both feed into the ND1 structure through highly intense γ-ray transitions at 851, 1805 keV (ND2b) and 1431 keV (ND2a) accordingly. The spin and parity assignment for the lowest state of the ND2a structure was determined by the rather intense transition at 1431 keV with a R_{DCO} value indicating an $E2/M1$ character. This assignment is further supported by the 580 keV transition, which is also of $E2/M1$ character. The spin and parity assignment of the lowest state of the ND2b structure was defined by the R_{DCO} values of the 851 and 1805 keV transitions, R_{DCO}(851)= 0.93(6) with ΔI=0 behavior, and R_{DCO}(1805)= 1.12(9) with $E2$ behavior, respectively. The large uncertainties in the R_{DCO} value for the 2097 keV γ-ray transition, which depopulates the state at 6445 keV, makes the state spin and parity assignments tentative (8^+). The multipolarity assignments of all known states in ND1, ND2a, and ND2b have been verified.

4.1.2 Structure ND3

The earlier known structure ND3a ($\alpha = 1$) and the new structure ND3b ($\alpha = 0$) are considered signature partners. They are connected via relatively intense 1088, 1209, 1341, 1512 and 1603 keV γ-ray transitions. The DCO ratios for all these transitions are consistent with mixed $E2/M1$ character, which indicates that these structures must have the same parity. The maximum spin is I = 13^- at E_x = 9214 keV for structure ND3a and I = 14^- at E_x = 10725 keV for structure ND3b. Structure ND3a has seven connecting transitions to the low spin

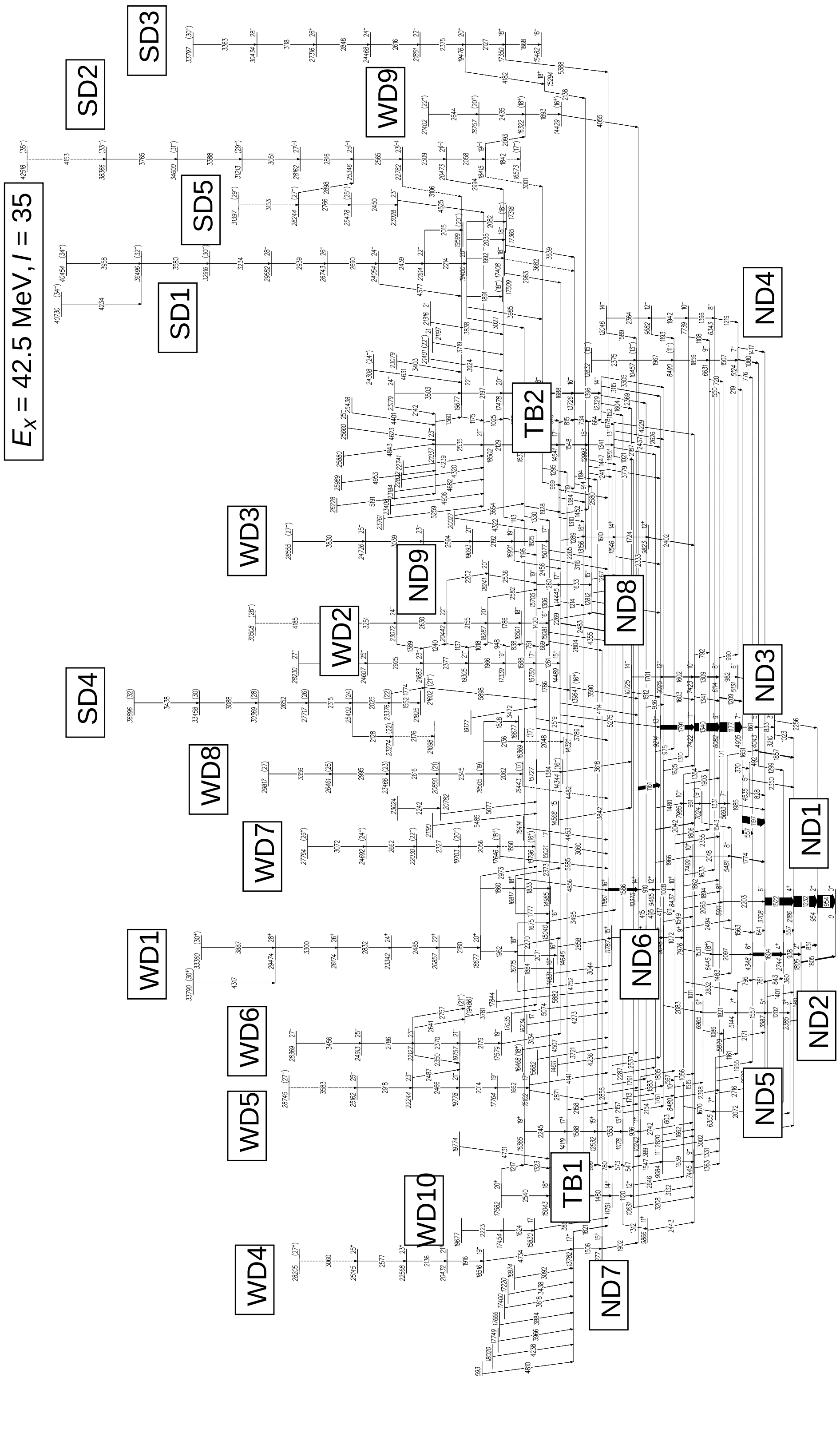

Figure 4.1: Proposed high-spin level scheme of ^{62}Zn. Energy labels are in keV and the intensities of the transitions are here indicated by the relative thicknesses of the arrows. Tentative levels and transitions are dashed.

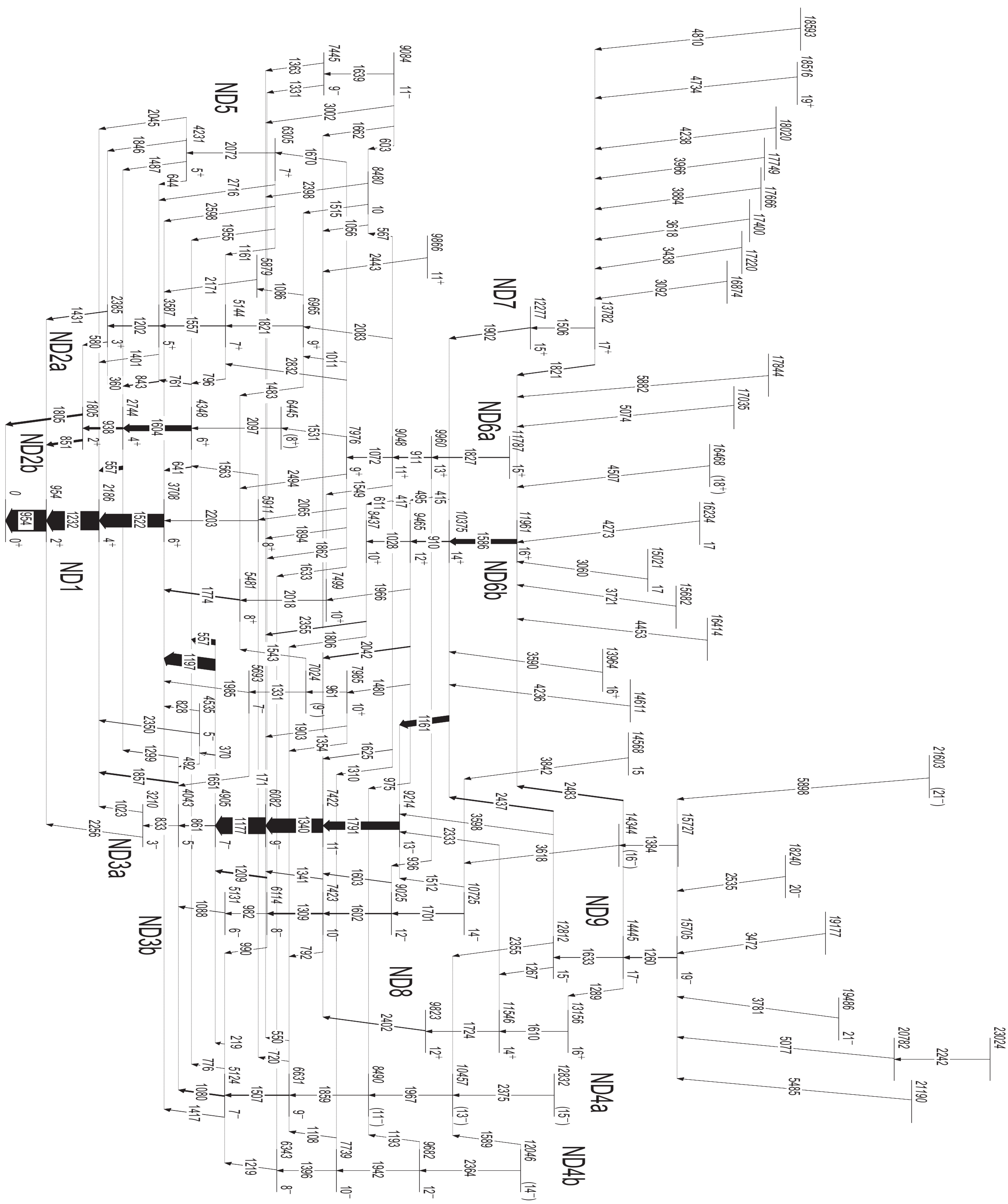

Figure 4.2: Normally deformed region of the proposed level scheme of ^{62}Zn. Energy labels are in keV. See text for details.

levels. Four of these, at 1023 ($3^- \rightarrow 4^+$) , 1197 ($7^- \rightarrow 6^+$) , 1857 ($5^- \rightarrow 4^+$) and 2256 ($3^- \rightarrow 2^+$) keV, decay into structure ND1, and the transitions at 557 ($7^- \rightarrow 6^+$) and 1299 ($5^- \rightarrow 4^+$) keV instead decay into ND2b.

The 370 keV γ-ray depopulates the 7^- state at E_x = 4905 keV, and decays into the 5^- state at E_x = 4535 keV. The R_{DCO} value of the 370 keV γ-ray, R_{DCO}(370) = 0.92(7), indicates an $E2$ character. This defines the spin and parity assignment, $I = 5^-$, for the state at 4535 keV. Among all these transitions, the intense 557 and 1197 keV transitions carry out $\sim$ 90 % of the intensity from structure ND3a.

As already mentioned, the 557 keV $E1$ transition which depopulates the state at 4905 keV, is a doublet with the same energy as the mixed $\Delta I = 0$ transition, depopulating the level at 2744 keV. The lowest states of ND3a and ND3b were determined by the R_{DCO} values of the 1023 and 1088 keV γ-rays, respectively. The two weak transitions, at 792 and 990 keV, from ND3b are connecting to the other part of the low-spin region. The in-band transitions of ND3a and ND3b are consistent with $E2$ character. They define the spin and parity assignments within the structure.

The two doublet transitions, at 1602 keV and 1603 keV, and 1340 keV and 1341 keV were placed in parallel according to $\gamma\gamma\gamma$ coincidences and R_{DCO} values. The measured DCO ratios for the 1602 and 1340 keV transitions indicate their quadrupole nature. Due to the doublet structure of these transitions with almost the same energies, it is then difficult to confirm the multipolarites of 1603 and 1341 keV transitions with their R_{DCO} values, which suggest as $E2$ transitions. However, these two transitions are connecting between the same parity bands and thus confirmed them as mixed $E2/M1$ character.

A γ-ray spectrum in coincidence with the gated transition at 1209 keV, which depopulates the 8^- state at E_x = 6114 keV, is presented in Fig. 4.3, panel (a). The strong coincidences at 954, 1232 and 1522 from ND1 and the transition at 938 from ND2b, 861 keV from ND3a and the in-band transitions at 1309, 1602 and 1701 keV of ND3b are clearly visible. The weak transition at 2350 keV, from the 5^- state at 4535 keV to the yrast 4^+ state at 2186 keV is also seen. From the 11^+ state at 9048 keV of ND6a, there is a transition of 1625 keV connecting to ND3b. The in-band transitions at 911 and 1827 keV of ND6a, including the 1625 keV transition are also labelled in the spectrum. The intense decay-out transitions at 851 and 1805 keV from ND2b and decay-out transition at 1857 keV from ND3a are also marked. Many other low intensity coincidences are also visible in the figure. The inset shows the high-energy portion of this spectrum including the low-intensity 4355 and 4734 keV transitions, which are the main linking transitions to two high-spin band structures (WD2b and WD4).

4.1.3 Structure ND4

The ND4 structure comprises two new structures, which are signature partners labelled as ND4a ($\alpha = 1$) and ND4b ($\alpha = 0$). ND4a ranges from the 5124 keV 7^- state to the 12832 keV (15^-) state, whereas ND4b corresponds to a set of states from 8^- at 6343 keV to (14^-) at 12046 keV. The $I^\pi = 7^-$ assignment to the band head of structure ND4a at 5124 keV was fixed by the stretched $E2$ character of the 1080 keV transition connecting to the 5^- state at E_x = 4043 keV. The spin and parity assignment to the 9^- state at E_x = 6631 keV is based on the $E2$ character of the 1507 keV transition, with an R_{DCO} (1507) = 1.05(6). The assignments of the (11^-), (13^-) and (15^-) states at 8490, 10457 and 12832 keV, respectively, is based on the apparent regular increase of their excitation energies.

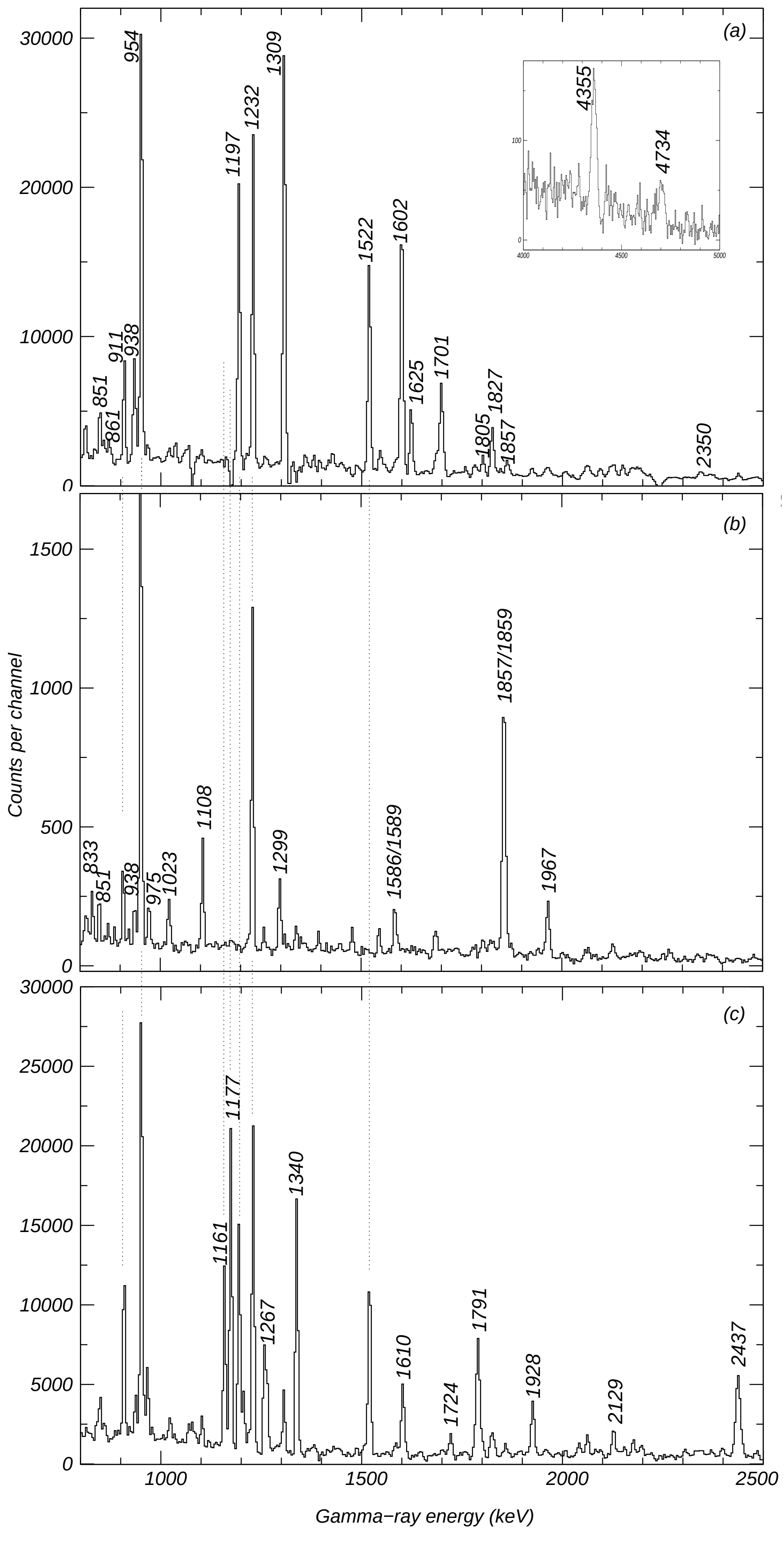

Figure 4.3: Spectra taken in coincidence with (a) the 1209 keV γ-ray transition, (b) both the 1080 and 1507 keV γ-ray transitions, and (c) both the 1260 and 1633 keV γ-ray transitions. See text for details.

The two lowest states at 6343 and 7739 keV of ND4b decay into the states at 5124 and 6631 keV of ND4a via intense $E2/M1$ transitions at 1108 and 1219 keV, respectively. The other two states at 9683 and 12046 keV of ND4b decay into states at 8490 and 10457 keV of ND4a via weak $E2/M1$ transitions at 1193 and 1589 keV. The lowest level at 6343 keV in ND4b is established as $I^{\pi} = 8^{-}$ state based on the mixed $E2/M1$ nature of the 1219 keV line. The in-band structure transitions at 1396 and 1942 keV have $E2$ character. The topmost state, I^{π} = (14^{-}) at 12046 keV, is added based on regular rotational character.

Figure 4.3 panel (b) shows the γ-ray spectrum in coincidence with transitions at 1080 or 1507 keV. The in-band transitions at 1859 and 1967 keV of ND4a and the intense connecting transition at 1108 keV between ND4a and ND4b, are clearly seen. The relevant peaks belonging to normal deformed structures are identified with dashed lines. The normal deformed region transitions at 833, 851, 938, 975, 1023, 1299 and 1586 keV from the other part of the level scheme are also visible.

4.1.4 Structure ND5

Structure ND5 is an irregular structure with a lot of positive-parity states in the range $E_x \sim 4 - 9$ MeV. Except for the transition at 1774 keV ($8^{+} \rightarrow 6^{+}$), the intensities of all such γ-rays are on the level of a percent or less. The 9^{+} state at 7976 keV of ND6a decays to the level at 6305 keV by a 1670 keV γ-ray transition. R_{DCO} (1670)= 1.32(22) is consistent with an $E2$ character, and defines the state at 6305 keV to be 7^{+}. The state at 6305 keV decays to both a 5^{+} state (through E_{γ} = 2072 keV) and a state with 5^{+} (via E_{γ} = 2716), and the 2716 keV line has a DCO ratio, which indicates an $E2$ transition. The quadrupole nature of the 1639 keV ($11^{-} \rightarrow 9^{-}$) γ-ray transition defines the states 11^{-} at 9083 keV and 9^{-} at 7445 keV.

Here, the 4231 keV, $I^{\pi} = 5^{+}$ state is a good example for a definite assignment of spin and parity despite the lack of angular correlation data of both feeding or depopulating transitions. The decay chain from the state 9^{+} at 7976 keV of ND6a to the state 3^{+} at 2385 keV of ND2a is as follows: $9^{+} \rightarrow 7^{+} \rightarrow$ 4231 keV state $\rightarrow 3^{+}$. The states 9^{+} at 7976 keV of ND6a, 7^{+} at 6305 keV and 3^{+} at 2385 keV of ND2a are fixed. The possible spin and parity options for state at 4231 keV are 6^{+}, 5^{+}, 5^{-} and 4^{+}. Assignments of 6^{+}, 5^{-} and 4^{+} are ruled out based on the less transition probabilities of $M2$ or higher order multipolarities. Consequently the spin and parity assignment of the state at 4231 keV is fixed to be 5^{+}.

4.1.5 Structure ND6

Structures ND6a ($\alpha = 1$) and ND6b ($\alpha = 0$) are two earlier known signature partner structures with $E2$ transitions inside each structure, connected via $E2/M1$ transitions at 415, 417, 495 and 611 keV. The ND6 structure is decaying into ND1, ND2, ND3 and ND5.

The structure ND6a is formed by a set of states from the 7976 keV 9^{+} state to the 11787 keV 15^{+} state. It has a sequence of $E2$ transitions at 1072, 911 and 1827 keV. The previously placed transition at 1268 keV, on the top of the 9048 keV level, is now replaced with the 911 keV transition. The doublet transitions at 910 and 911 keV of ND6a and ND6b were placed next to each other according to their respective coincidences. Several γ-ray transitions, namely at 567, 936, 1011, 1531, 1549, 1625, 1633, 1862, 1894, 2065, 2083, 2494 and 2832 keV connect the ND6a structure to the low-spin normal deformed region. The R_{DCO} value of the intense transition at 2832 keV ($9^{+} \rightarrow 7^{+}$) indicates that it is an $E2$ transition. Hence, the 7976 keV level has a spin and parity of 9^+. The spin and parity assignment of the 11^+ state at 9048 keV was defined by the R_{DCO} value of the 1625 keV γ-ray transition. The R_{DCO} value of this transition, R_{DCO} (1625) = 0.59(4) is consistent with $E1$ character.

The structure ND6b corresponds to a set of states from the 8437 keV 10^+ state to the 11961 keV 16^+ state. The band members are the 1028, 910, and 1586 keV transitions, which are consistent with $E2$ nature. There are several decay-out transitions from the structure ND6b, like 975, 1161, 1480, 1806, 2042, and 2355 keV. Among all these, the transitions at 1161, 2043 and 2355 keV are intense enough to define the band's spin and parity assignment. The DCO ratios, R_{DCO}(1161) [$14^+ \rightarrow 13^-$] = 0.54(3), R_{DCO}(2042) [$12^+ \rightarrow 11^-$] = 0.51(5) and R_{DCO}(2355) [$10^+ \rightarrow 9^-$] = 0.67(5) are consistent with pure $E1$ character. The structure ND6b decays to the 13^- state of ND3a via the 1586-1161- keV, $E2 - E1$ cascade. These two γ rays mark the end of transitions with relative intensities in excess of 10%. Thus, the 1586 keV transition is very important to find out the DCO-ratios of many of the weak connections, which are towards the rotational bands.

States without any Structures

There are several states which do not seem to belong to any apparent band-like structures, namely at 13964, 14611, 15021, 15682, 16234, 16414, 16468, 17035, and 17844 keV. The corresponding weak intensity γ-ray transitions from these states, for example, at 3060, 3721, 4273, 4453, 4507, 5074 and 5882 keV are decaying into the state 16^+ at E_x = 11961 keV. The two transitions at 3590 and 4236 keV instead decay into the state 14^+ at E_x = 10375 keV of ND6b. It is possible to determine DCO ratios for some of these weak transitions. For instance, a R_{DCO} value of the 4507 keV transition, R_{DCO} (4507) = 0.86(18), which in combination with yrast arguments tentatively suggests the state at 16468 keV to have $I^\pi = (18^+)$. The same procedure has been used to assign a spin of I= 17 to the states at 15021 and 16234 keV, while the parity of the levels remains undetermined. The spin and parity assignment of the state 16^+ at E_x = 13964 keV is confirmed by the DCO ratio of the decay-out transition at 3590 keV, which is consistent with an $E2$ character. The multipolarity assignments of the other states could not be established due to low intensity decay-out transitions.

Figure 4.4 (a) illustrates the high-energy part of the γ-ray coincidences with the 1586 keV transition in ND6b. The transitions depopulating several high-spin band structures decay into the state 16^+ (not shown in Fig. 4.2 but see Fig. 4.1)at 11961 keV, like at 3789 (WD2a), 3869 (WD10), 4141 (WD5), 4734 (WD4), 4856 (WD1), or 5388 (SD3) keV are clearly visible. Even though the decay-out γ-transition at 4114 (WD2a) keV does not feed into the 11961 keV level, it is clearly seen in the spectrum, due to the contamination from an in-band transition at 1588 keV in WD2a. The in-band transitions at 3503 keV from TB2 and 3623 keV from WD2a are also seen in the spectrum. A large number of weak high-energy γ rays at 4273, 4507, 5074, 4238 and 4810 keV, depopulating the corresponding states at 16234, 16468, 17035, 18020 and 18593 keV, are feeding into the 16^+ state at 11961 keV, are also identified.

4.1.6 Structure ND7

The new structure ND7 is built with two states, 15^+ and 17^+ at 12277 keV and 13782 keV, respectively. The one and only in-band transition at 1506 and the two other transitions at 1821 and 1902 keV lead to the yrast 17^+ state at 13782 keV. The DCO-ratios of both the 1821

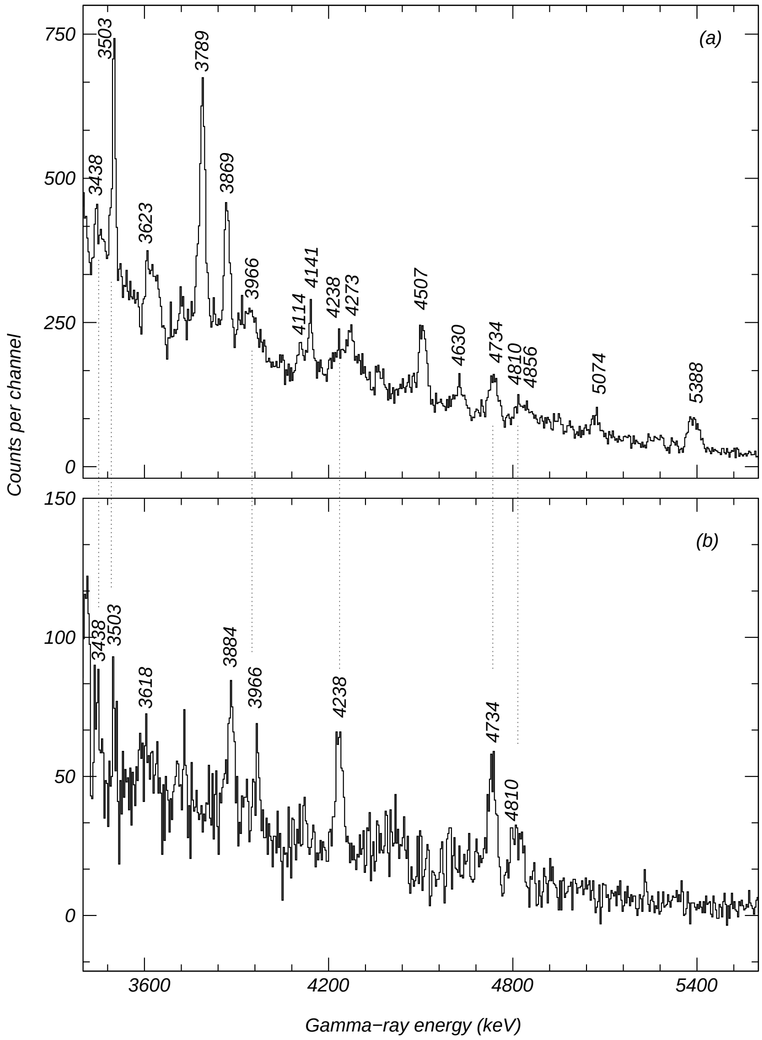

Figure 4.4: (a) High-energy part of the γ-ray spectrum in coincidence with the gating transition at 1586 keV. (b) High-energy part of the γ-ray spectrum in coincidence with the gating transition at 1821 keV.

and 1902 keV lines clearly point at mixed $E2/M1$ character, while the number available for the 1506 keV transition is consistent with a stretched $E2$ assignment. Interestingly, the mixing ratios $\delta(E2/M1)$ for the 1821 and 1902 keV transitions are nearly same; either moderate ($\delta \approx 0.3$) or significant ($\delta \approx 2.0$) quadrupole mixture is observed. Similar to the 11961 keV, 16^{+} state, the 13782 keV level is also fed by several 3-5 MeV high-energy γ-ray transitions. Among all these transitions, there is only one transition at 4734 keV, which depopulates the state at 18516 keV, associated with $E2$ character. The spin and parity assignments of that state were defined to be 19^{+}. The multipolarities of the remaining states could not be established due to weak intensity decay-out transitions at 3092, 3438, 3618, 3884, 3996, 4238, and 4810 keV. Figure 4.4 (b) shows the high-energy part of the γ-ray spectrum in coincidence with the 1821 keV γ-ray, which depopulates the state at 13782 keV. The highly energetic γ-ray transitions at 3438, 3503, 3618, 3884, 3966, 4238, 4734 and 4810 keV are clearly visible. All marked γ-ray transitions in Fig. 4.4 (b) are also seen in Fig. 4.4 (a) and are identified with dashed lines.

4.1.7 Structures ND8 and ND9

The ND8 structure is built up by a set of states from 12^+ at E_x = 9823 keV to the state 16^+ at E_x = 13156 keV. The one and only strong decay out transition is at 2402 keV (12^+ at 9823 keV $\rightarrow$ 11^- at 7422 keV) resolves the spin and parity of 9823 keV level. The R_{DCO} (2402) = 0.63(6) indicates its dipole character. The parity of ND8 is confirmed by the decay of the fixed state 20^+ at 19476 keV [45] into the state 16^+ at 13156 keV of ND8 via the 4128-2138-keV, $E2$ cascade (see Fig. 4.1). The R_{DCO} value of 2402 keV, which in combination with the $E2$ 1724 keV in-band transition of ND8, define the spin and parity assignment of the 9823 state to be I^π= 12^+. The 11546 keV state decays into the 9214 keV (ND3a) state via a 2333 keV γ-ray transition. The R_{DCO} value of 2333 keV transition is 0.53(9), is consistent with a dipole nature. Since the parity of the ND8 and ND3a is fixed, so the transition at 2333 keV is assigned to be electric dipole nature, which further define the level at 11546 keV to be 14^+. The in-band transitions at 1724 and 1610 keV have $E2$ character.

The structure ND9 consists of the 12812, 14445 and 15705 keV levels with two deexciting γ-ray transitions at 1633 ($17^- \rightarrow 15^-$) and 1260 ($19^- \rightarrow 17^-$) keV in cascade. These two in-band transitions are quadrupole in nature since their DCO ratios are close to unity. The fixed state 19^- at 16373 keV [20] decays into the level at 14445 keV of ND9 via an $E2$ 1928 keV transition (see Fig. 4.1), which fixes the ND9 structure with negative parity. The structure ND9 decays into the structure ND8 through the 1267 and 1289 keV γ-ray transitions. The spin and parity of the state at 12812 keV was confirmed by a rather intense decay-out transition at 2437 keV. The 2437 keV γ-ray has R_{DCO} = 0.68(4), which is consistent with dipole character. Since this transition proceeds from the negative parity level at 12812 keV and decays into the fixed positive parity state 14^+ at 10375 keV, which thus confirmed the 2437 keV transition as an $E1$ character. The level at 14445 keV decays by emission of three γ-rays at 1289, 1633 and 2483 keV. The DCO ratio measurement of the intense decay-out transition at 2483 keV retrieve spin and parity assignments for 14445 keV state. The R_{DCO} (2483) = 0.52(3) is consistent with an $E1$ character and indicates that the spin and parity of the state at 14445 keV to be 17^-.

Similar to the 11961 keV, 16^+ state, the 15705 keV level is fed by six high-energy γ-ray transitions at 2535, 3472, 3781, 5077, 5485 and 5898 keV. The DCO values of the 2535 and 3781 keV transitions confirm the spin and parity of the states at 18239 and 19486 keV to be 20^- and 21^-, respectively. The DCO-ratios of the other γ-ray transitions could not be measured due to their weak intensities. The decay out transition at 5898 keV, which depopulates the 21603 keV state, is also too weak to determine a DCO ratio. The state spin and parities are instead preliminarily assigned to tentative (21^-) using yrast arguments.

Figure 4.3 (c) illustrates coincidences with both transitions at 1260 and 1633 keV. The relevant transitions from the low-spin normal deformed part of the level scheme are identified with dashed lines. In addition to the in-band transitions of ND8 at 1610 and 1724 keV, the decay-out transitions at 1267 and 2437 keV from the 15^- state at 12812 keV are marked. To structure TB2 (see Sect. 4.2.2), there is the 1928 keV linking transition visible, and from the structure TB2 itself the 2129 keV transition is also shown. This indicates that the TB2 structure decays into ND9. Several low-intensity transitions are also visible in the spectrum.

4.1.8 Other States

The spin and parity assignment of 10^+ to the state at 7499 keV is determined by the 2018 keV transition. The 7499 keV state decays to the 8^+ state at 5481 keV through a 2018 keV transition. The R_{DCO} (2018) = 1.03(8) indicates that the transition is of $E2$ character. The spin and parity of the 7499 keV and 5481 keV levels is then 10^+ and 8^+, respectively. This assignment is further supported by the 1774 keV transition, which is also an $E2$ character.

In a similar way, spin and parity assignments for the 10^+ state at 7985 keV and 7^- state at 5693 keV were defined. The large uncertanity in the R_{DCO} value of the 1331 keV transition, depopulating the 7024 keV state, makes the state spin and parity assignments tentative (9^-).

The state at 13964 keV was fixed to 16^+ via the 3590 ($16^+ \rightarrow 14^+$) $E2$ decay out transition.

4.2 Known Terminating Bands TB1 and TB2

Deformed bands that are observed to high rotational frequency with decreasing moments of inertia are called smoothly terminating bands [46]. TB1 and TB2 are previously known smoothly terminating bands [20].

4.2.1 Structure TB1

Figure 4.5 shows the structure of TB1. It consists of two signature partners, TB1a ($\alpha = 1$) and TB1b ($\alpha = 0$), which are built from quadrupole transitions and connected via intense $E2/M1$ transitions between them. The previous publication [20] determined a tentative parity for TB1. Current results confirm the parity of TB1a and TB1b by several linking transitions, which are connected to the established low-spin region. For example, the level at 10631 keV of TB1b decays to the fixed state 10^+ via a 3132 keV transition. The DCO ratio of 3132 keV transition, R_{DCO} (3132) = 1.11(23) is consistent with an $E2$ character, and fixed the spin and parity assignments of the level at 10631 keV to be 12^+. The maximum spin is I^π = (21^+) at E_x = 19498 keV for TB1a and I^π = 20^+ at E_x = 17582 keV for structure TB1b. In addition to the previously suggested transitions at 2742, 3002 and 3208 keV, now the band is connected to the rest of the level scheme with many more γ-ray transitions, for example, at 1312, 1547, 1583, 1662, 1713, 1761, 1791, 1805, 2129, 2154, 2157, 2158, 2287, 2537, 2646, 2820, 2856 and 3132 keV. Among all these decay-out transitions, several R_{DCO} values were determined and used to define spin and parity assignments of TB1a and TB1b.

For example, the spin and parity assignments of the lowest states, 11^+ at 10242 keV (TB1a) and 12^+ at 10631 keV (TB1b) were defined by DCO ratios of the 2742 and 1547 keV transitions, respectively. The R_{DCO} value of the former transition, R_{DCO} (2742)= 1.10(16) is suggests $E2$ character, it is also consistent with mixed $E2/M1$ character. This assignment is mainly based on the decay pattern: the 12^+ state at 10631 keV decays into the 11^+ state at 10242 via a mixed $E2/M1$ 389 keV transition, the 11^+ state further decays into the 10^+ state at 7499 keV via 2742 keV transition. Since the spin and parity assignments of 12^+ state at 10631 keV and 10^+ state at 7499 keV are fixed, thus the 2742 keV transition is assigned to have $E2/M1$ character. The DCO ratio of 1547 keV transition, R_{DCO} (1547) = 0.59(5) is consistent with an $E1$ character.

There is one high-energy transition at 4731 keV decaying into the structure TB1. Since the intensity of this transition is low, it is difficult to measure a DCO ratio on it. The in-band transitions of TB1a and TB1b have $E2$ nature, and connecting transitions between them have

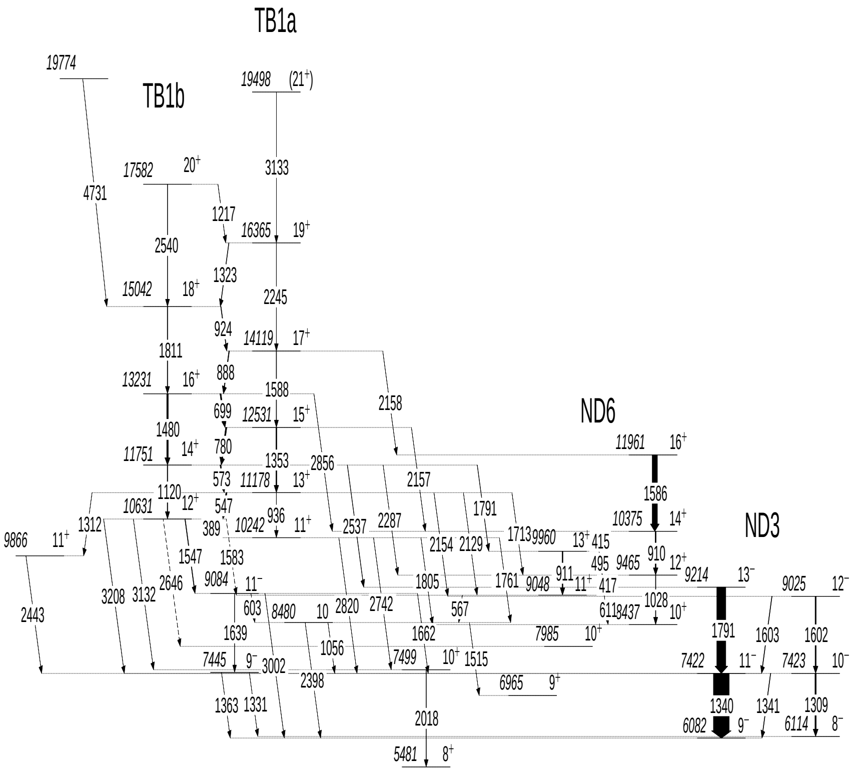

Figure 4.5: Structure of TB1 of the present level scheme. Energy labels are in keV and the intensities of the transitions are here indicated by the relative thicknesses of the arrows. Tentative levels and transitions are dashed.

$E2/M1$ character. All these R_{DCO} values are listed in paper III (Table 1).

Figure 4.6 (a) shows the γ-ray spectrum in coincidence with any combination of the 547, 573, 780, 699, 888 keV and the 547, 573, 780, 699, 888 and 924 keV $E2/M1$ transitions of structure TB1. In conjunction with the band members of TB1a and TB1b, all $E2/M1$ transitions in between them are also clearly seen. The intense decay out transitions at 1547, 1662, 2129, 3002, 3132 and 3208 keV are marked with star (*) symbols in black colour, while all transitions belonging to the normal deformed region are marked with star (*) symbols in blue color. The presence of a peak at 2018 keV arises from the decay pattern of the 12^{+} state at 10631 keV. The 12^{+} state at 10631 keV decays to the 10^{+} state at 7499 keV via 3132 keV γ transition, and the 10^{+} state at 7499 keV further decays to the state 8^{+} at 5481 keV via 2018 keV γ transition.

4.2.2 Structure TB2

Figure 4.7 shows the structure of TB2. The previously published TB2 consists of two bands TB2a ($\alpha = 1$) and TB2b ($\alpha = 0$), which are signature partners. These two bands are built from $E2$ transitions and connected via strong $E2/M1$ transitions between them. In addition to the previously suggested transitions at 1931, 3115 and 4229 keV, now the band is connected to the rest of the level scheme with many more γ-ray transitions, namely at 914, 969, 1021, 1113, 1152, 1241, 1295, 1310, 1330, 1384, 1447, 1604, 2187, 2369, 2437, 2580, 2626, 3305 and 3779 keV. Among all these decay-out transitions, several R_{DCO} values were determined and used to define spin and parity assignments of TB2a and TB2b.

For example, the lowest states, 13^- at 11651 keV (TB2a) and 14^- at 12329 keV (TB2b), were defined by DCO ratios of 4229 and 3115 keV transitions, respectively. The R_{DCO}(4229 keV) = 1.30 (21) has an $E2$ nature and the R_{DCO}(3115 keV) = 0.93(10) has a mixed $E2/M1$ determine the corresponding levels spin and parity assignments. Even though the value of DCO-ratio for 3115 keV transition is close to the expectation for an $E2$ transition, the 3115 keV transition has been assigned an $E2/M1$ character. The fact is that the fixed 15^- state at 12993 keV decays into the 14^- state at 12329 keV via a mixed $E2/M1$ 664 keV transition, and further the 14^- state decays into the fixed 13^- state at 9214 keV via 3115 keV transition. The in-band transitions of TB2a and TB2b have $E2$ nature, and connecting transitions between them have $E2/M1$ character. All these R_{DCO} values are listed in paperIII (Table 1) [18].

In addition, the TB2 structure is fed by eighteen 3 - 5.5 MeV high-energy γ-ray transitions, namely at 3403, 3654, 3719, 3838, 3924, 4239, 4320, 4323, 4401, 4623, 4631, 4682, 4843, 4906, 4953, 5191 and 5259 keV. The γ-ray transitions at 3719, 3838, 3924, 4623 and 4631 keV are sufficiently intense to support the corresponding level spin and parity assignments. The remaining transitions are too weak to measure the DCO ratios, thus the corresponding state spin and parity assignments could not be established.

Figure 4.6 (b) shows the γ-ray spectrum in coincidence with any combination of the 664, 679, 734, 815 keV and the 664, 679, 734, 815 and 873 keV $E2/M1$ transitions of structure TB2. In conjunction with the band members of TB2a and TB2b, all $E2/M1$ transitions in between them are also clearly seen. The rather intense decay-out transitions at 1928, 2437 and 3115 are marked with star (*) symbols in black colour, while all transitions belong to the normal deformed region are marked with star (*) symbols in blue color. Several low-intensity transitions are also visible in the spectrum. Figure 4.6 (c) illustrates the highest energy γ-ray transitions ranging from 3.5 - 6.0 MeV belonging to TB2. The intense decay-out transition at 4229 keV is clearly visible, as well as other weak transitions at 3719 and 3924 keV.

4.3 Well-deformed and Superdeformed Band Structures

The high quality of data set 1, together with data set 2, allowed the current analysis to establish ten well-deformed high-spin band structures, with I_{max} ranging from 22$\hbar$ to 30$\hbar$, and five superdeformed bands with I_{max} ranging from 29$\hbar$ to 35$\hbar$. All these bands are shown in Fig. 4.1. For a thorough description see [18, 45]. A short summary is given in the following.

In the decay scheme Fig. 4.1, the labelling given to the ten well-deformed bands is WD1 to WD10. The lowest states of all these bands are connected to the low-spin normal deformed region via linking transitions. WD1 is the most intense high-spin band in the present analysis, with an intensity of about 2$\%$ relative to the 954 keV ground state transition. Only one transition at 3887 keV was observed from data set 2 which was placed at the top of the band. The band WD2 consists of two bands, which are signature partners (WD2a with $\alpha = 1$ and WD2b with $\alpha = 0$) and are connected to each other via $E2/M1$ transitions. In-band transitions of all ten bands are consistent with $E2$ character.

The spin and parity assignment for the lowest states of all these bands have been determined by R_{DCO} values of their linking transitions. For example, the lowest state of WD4 at 18516 keV decays into the state 17^+ at 13782 keV via a 4734 keV γ-ray transition. The R_{DCO}(4734) = 1.20(25) is consistent with a stretched $E2$ character, suggesting a 19^+ assignment to the 18516 keV state.

Figure 4.8 shows the coincidence spectrum gated on the decay-out transition at 4734 keV and any one of the band members of WD4 at 1916, 2136 and 2577 keV. The band members of WD4 at 1916, 2136 and 2577 keV are clearly visible. The relevant transitions in the normal deformed region of the level scheme, for an example at 954, 1197, 1232, 1310, 1340, 1522, 1586, 1604, 1791 and 1821 keV, are identified with star (*) symbols in blue.

Superdeformed bands are labelled with SD1, SD2, SD3, SD4 and SD5 in Fig. 4.1. All five bands are connected to the low-spin states by several linking transitions. This provides spin and parity assignments to the lowest states in the bands, because the transitions at the bottom of the bands are either sufficiently intense or sufficiently clean to distinguish between stretched quadrupole and dipole characters of some of the more intense linking transitions.

The previously observed band SD1 was extended [45] by adding transitions at 3579, 3958, and 4234 keV on the top of the state at 32917 keV. SD1 and SD2 are signature partner bands. The maximum spin in the current analysis is 35^- for the 42517 keV state belonging to SD2. The topmost three transitions of SD1 and SD2 are observed only in data set 2. The SD3 band is built up by a set of states from 16^+ at E_x = 15483 keV to the state 30^+ at E_x = 33799 keV. The spin and parity of SD3 was confirmed with a strong enough decay-out transition at 5388 keV, which has $E2$ nature. The spin assignment of the SD4 band is tentative and the band's parity is uncertain. The band is built up by a set of levels from 21825 keV to the 36896 keV, and is connected to the low-spin part of the level scheme via the 1774-5898 keV weak intensity γ-ray cascade. The SD5 is built up by a set of states from 23^- at E_x = 23028 keV to the state (29^-) at E_x = 31397 keV. The assignments of the (25^-), (27^-) and (29^-) states at 25478, 28244 and 31397 keV, respectively, is based on the apparent regular increase of their excitation energies.

Assuming an E2 character of the in-band transitions, the tentative spin and parity assignments to the states near the top of the all bands are based on their regular rotational behaviour. All bands spin and parity assignments are given in Fig. 4.1 and are listed in paper III (Table 1) [18].

Figure 4.9 explains the exceptionally high quality of data set 1. The figure shows a spectrum in coincidence with the 5388 keV decay-out transition of SD3 and one of the band members of SD3 (2375, 2616, 2849 and 3118 keV). The intensity of 5388 keV is as low as 0.02$\%$ relative to the 954 keV ground state transition, whereas the SD3 band intensity is less than 2$\%$. The triple coincidences both with members of SD3 (2127, 2375, 2616, 2849 and 3118 keV) and with the relevant transitions in the low-spin regime like 1232, 1340, 1522, 1586 and 1791 keV, which are marked with a star (*) in blue, are clearly visible. This proves the good and high quality of data set 1.

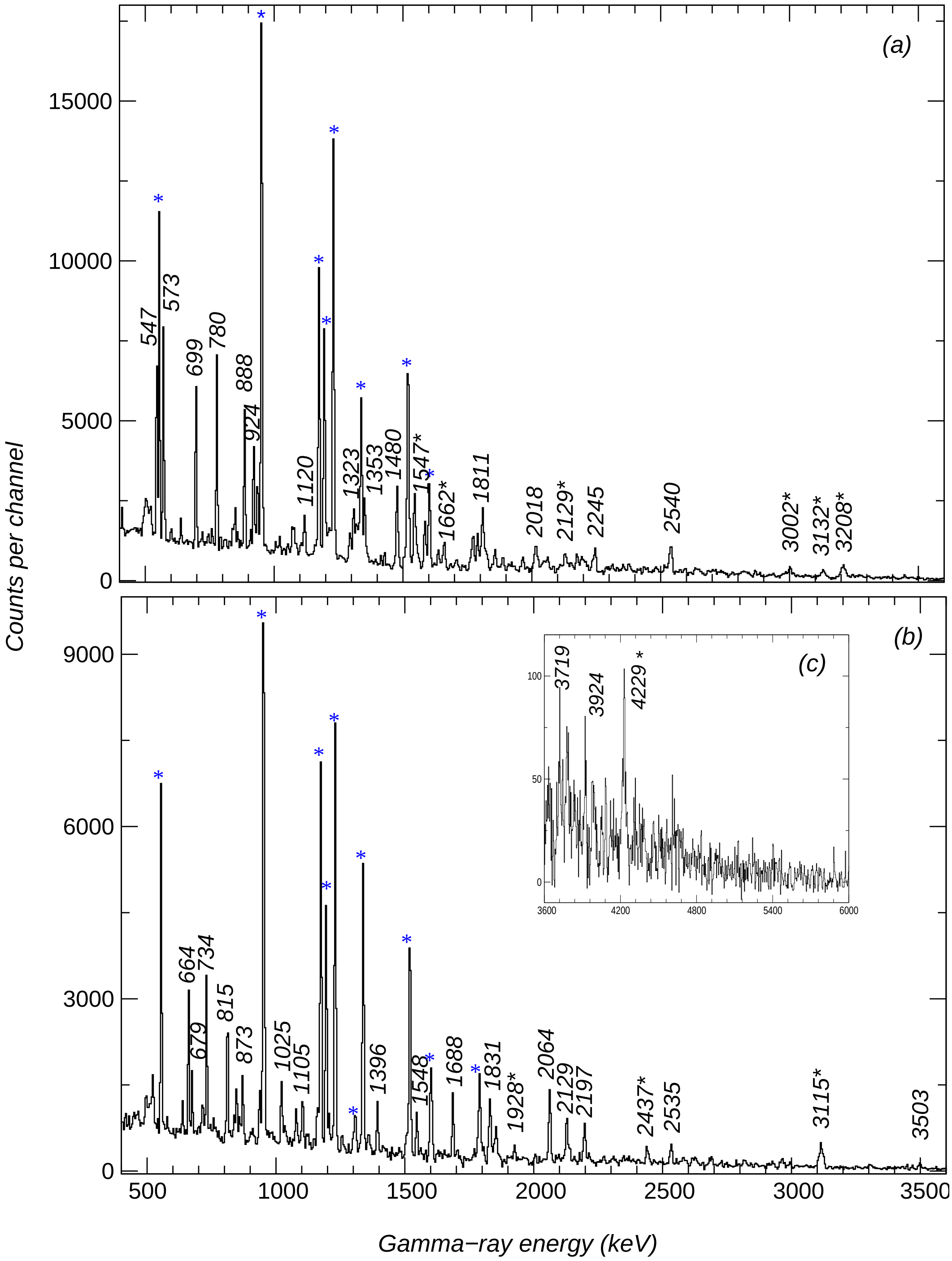

Figure 4.6: (a) Coincidence spectrum with any combination of the 547, 573, 780, 699, 888 keV and the 547, 573, 780, 699, 888 and 924 keV transitions of TB1. The strong decay out transitions at 1547, 1662, 2129, 3002, 3132 and 3208 keV are marked with star (*) symbols in black colour, while all relevant normal deformed region transitions are marked with star (*) symbols in blue color. (b) Coincidence spectrum with any combination of the 664, 678, 734, 815 keV and the 664, 678, 734, 815 and 873 keV transitions of TB2. The strong linking transitions at 1928, 2437 and 3115 keV are indicated with a star (*) in black color. The relevant transitions belong to the normal deformed region of the level scheme are marked with star (*) in blue color. (c) Same coincidence γ-ray spectrum as (b), but illustrates for the high-energy γ-ray transitions ranging from 3.5 - 6.0 MeV of TB2 structure. See more details in text.

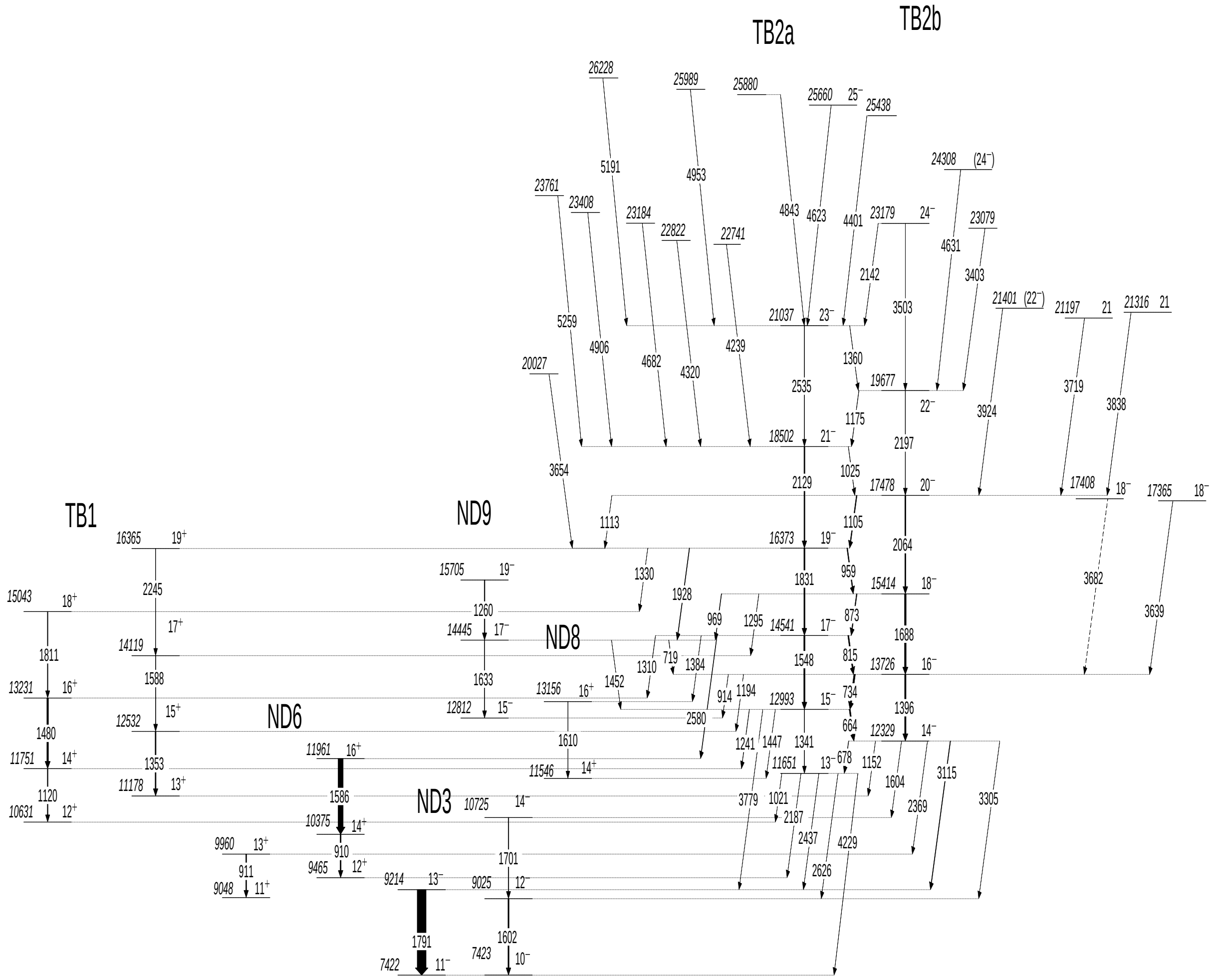

Figure 4.7: Structure of TB2 of the present level scheme. Energy labels are in keV and the intensities of the transitions are here indicated by the relative thicknesses of the arrows. Tentative levels and transitions are dashed.

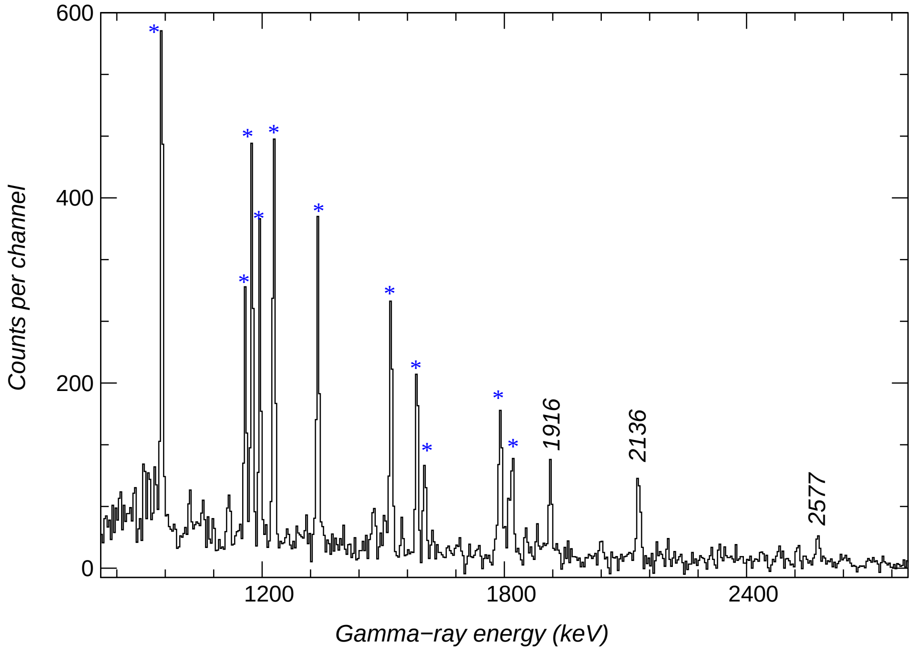

Figure 4.8: Coincidences with the 4734 keV decay-out transition of WD4 and one of the band members of WD4 (1916, 2136 and 2577 keV). Relevant, low-spin transitions are marked with star (*) in blue, while the band members at 1916, 2136 and 2577 keV are labelled with their energies.

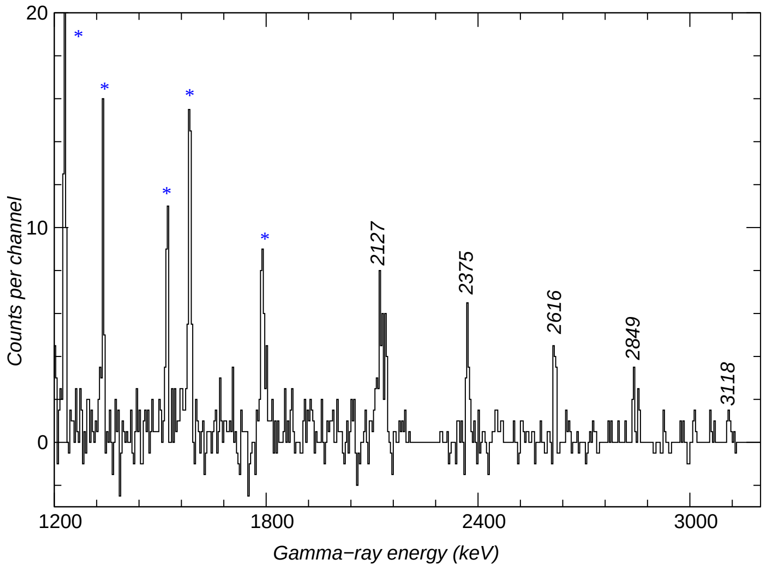

Figure 4.9: Coincidences with the 5388 keV decay-out transition of SD3 and any one of the band members (2127, 2375, 2616 and 2849 keV) of SD3. The relevant low-spin transitions are marked with star (*) in blue. The band members at 2127, 2375, 2616, 2849 and 3118 keV are marked with their energies. See text for more details.

Chapter 5

Theoretical Discussion

5.1 Nilsson Model

The nuclear shell model is generally used to describe spherical nuclei but it fails to explain the properties of deformed nuclei (nuclei with N and Z far from the closed shells) and rapidly rotating nuclei. To understand the basic properties of nucleons moving in a deformed nucleus, a model was introduced by S.G. Nilsson in 1955 [47], named as the Nilsson model. More details on this model are given in [48]. A brief summary is given below.

In the Nilsson model the modified oscillator potential [48, 49] is used to describe the motion of the nucleons. For an axial symmetric deformation, the Nilsson Hamiltonian takes the form

$$H = \frac{-\hbar^2}{2M}\Delta + \frac{1}{2}M(\omega_z^2 z^2 + \omega_\perp^2(x^2+y^2)) - 2\kappa\hbar\omega_0 \vec{l}\cdot\vec{s} - \kappa\mu\hbar\omega_0(l^2 - \langle l^2\rangle_N). \tag{5.1}$$

Here ω_0 is the harmonic oscillator frequency in the spherical limit while ω_z and $\omega_\perp$ are the frequencies of the anisotropic oscillator in the z-direction and the directions perpendicular to the z-direction, respectively. The first term provides the kinetic energy of the nucleons and the second term defines the quadrupole deformation dependence describing spheroidal shapes. The third term is the spin-orbit coupling and was introduced [50, 51] to reproduce the empirical shell gaps for different N and Z values. The last term $(l^2 - \langle l^2\rangle_N)$ is introduced to simulate the surface diffuseness depth, which leads to a proper single-particle ordering by lowering the energies of the large l orbitals within an N-shell. Here the $\langle l^2\rangle_N)$ term is included [52] to keep the average energy of an N-shell unaltered by the l^2 term. The strength of the $\vec{l}\cdot\vec{s}$ and l^2- terms is determined by the Nilsson parameters, κ and μ.

For small deformations, the single-particle states are defined by the approximate quantum numbers $nlj\Omega$. The parameter Ω is the projection of the total angular momentum (j) on the z-axis, n is the radial quantum number and l is the orbital angular momentum. For large deformations, the single particle states are described by the approximate 'asymptotic quantum numbers', $[N, n_z, \Lambda]\Omega$. Here $N = n_z + n_\perp$ is the principal quantum number, n_z and $n_\perp$ are the number of oscillator quanta in the z-direction and in the perpendicular direction, respectively, while Λ is the projection of the orbital angular momentum on the symmetry axis.

5.2 Cranking Model

To describe the single-particle motion in a rotating nucleus, the cranking model approximation is frequently used, which was suggested by Inglis in 1954 [53, 54]. The basic idea of the cranking model is the following classical assumption: The nucleus with an angular momentum $I \neq 0$ is rotating with a fixed frequency, ω, around a principle axis.

The cranking Hamiltonian is then given by

$$h^{\omega} = h - \omega j_x, \tag{5.2}$$

where h^{ω} is the Hamiltonian in the body-fixed rotating system and h is the single-particle Hamiltonian in the laboratory system. The x- component of the single-particle angular momentum is denoted by j_x, $j_x = l_x + s_x$. The term - ωj_x is analogous to the Coriolis and centrifugal forces in classical mechanics. The eigenvalues of h^{ω} are the single-particle energies in the rotating system, which are generally referred to as Routhians, e_i^{ω}. The total single-particle energy is calculated as the sum of the expectation values of the "single-particle energies" in the laboratory system,

$$E_{tot} = \sum_{occ} \langle h_i \rangle = \sum_{occ} e_i^{\omega} + \omega \sum_{occ} \langle j_x \rangle_i \tag{5.3}$$

The total angular momentum, I, is approximated by the sum of the expectation values of the $\langle j_x \rangle$ operator.

$$I \approx I_x = \sum_{occ} \langle j_x \rangle_i \tag{5.4}$$

In eqs. 5.3 and 5.4, $\sum_{occ}$ refers to the sum over the occupied proton and neutron orbitals. For the nuclear shapes considered here, the cranking Hamiltonian is invariant under a rotation of 180° around the x-axis,

$$R_x = R_x(\pi) = \exp(-i\pi j_x) \tag{5.5}$$

The eigenvalue of the R_x operator is $r = \exp$ (-i$\pi\alpha$), where the signature quantum number α is used to classifiy the single-particle orbitals. The total signature of a system is defined as the sum of the signature for the occupied orbitals,

$$\alpha_{tot} = \alpha = (\sum_{occ} \alpha_i) \bmod 2 \tag{5.6}$$

The value of α determines the possible spin values through the relation

$$\alpha = I \bmod 2, \tag{5.7}$$

Thus for an even number of nucleons we have α = 0 for I = 0, 2, 4 and α = 1 for I = 1, 3, 5, while for systems with an odd particle number, $\alpha = +1/2$ for I = 1/2, 5/2, 9/2 and $\alpha = -1/2$ for I = 3/2, 7/2, 11/2. Furthermore, we will only consider shapes that are invariant under reflection, $\vec{r} \rightarrow -\vec{r}$. This gives that parity is also a good quantum number.

5.3 Cranked Nilsson-Strutinsky (CNS) Calculations

To understand the experimentally observed bands in ^{62}Zn, configuration-dependent cranked Nilsson-Strutinsky (CNS) calculations [1, 55, 56] were carried out. In this formalism, the cranked Nilsson (modified oscillator) Hamiltonian is used to describe a nucleon in the rotating nucleus.

$$h^{\omega} = h_{osc}(\varepsilon_2, \gamma) - V' - \omega j_x + 2\hbar\omega_0\rho^2\varepsilon_4 V_4(\gamma), \quad (5.8)$$

The deformed harmonic-oscillator Hamiltonian h_{osc}, with different oscillator frequencies ω_x, ω_y and ω_z is expressed as

$$h_{osc} = \frac{p^2}{2m} + \frac{1}{2}m(\omega_x^2 x^2 + \omega_y^2 y^2 + \omega_z^2 z^2). \quad (5.9)$$

Generally these three frequencies are expressed in terms of quadrupole deformation coordinates ε_2 and γ [57], corresponding to the different ellipsoidal shapes.

$$\omega_i = \omega_0(\varepsilon_2, \gamma)[1 - \frac{2}{3}\varepsilon_2 \cos(\gamma + i\frac{2\pi}{3})],\ i = x, y, z. \quad (5.10)$$

The parameter ε_2 gives the degree of the deformation of the nucleus, while γ gives its degree of axial asymmetry. Figure 5.1 shows the values of ε_2 and γ, which are used to

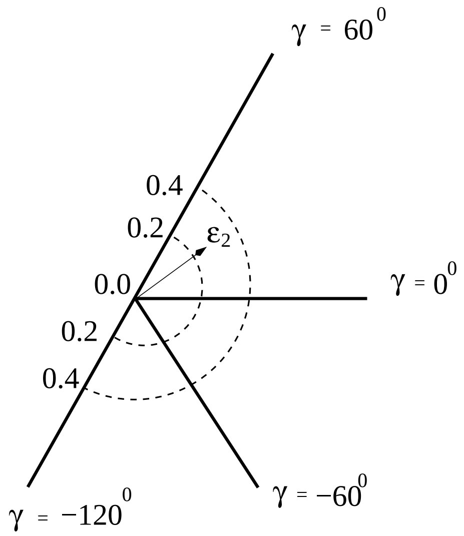

Figure 5.1: The (ε_2, γ) half plane, describing the shape and rotation axis of the nuclear potential.

describe all possible ellipsoidal shapes with rotation around the three principal axes. $\varepsilon_2 = 0$ corresponds to a spherical nucleus. The $\gamma = 0°$ axis refers to prolate shape, whereas the $\gamma = -60°$ axis refers to oblate shape. These two shapes are axially symmetric with collective rotation around the perpendicular axis. At the border line, the nucleus rotates around the oblate ($\gamma = 60°$) or prolate ($\gamma = -120°$) symmetry axis corresponding to the non-collective limit. Away from the axes, ($0° < \gamma < 60°$), ($0° < \gamma < -60°$) and ($-60° < \gamma < -120°$), the nuclear shape is triaxial, with rotation about each of the three different principal axis.

The second term in eq. 5.7,

$$V' = \hbar\omega_0^0\kappa_N 2\vec{l_t}\cdot\vec{s} + \mu_N(l_t^2 - \langle l_t^2\rangle_N), \quad (5.11)$$

was already discussed in connection with Nilsson model. The index t in the orbital angular momentum operator $\vec{l_t}$ indicates that it is defined in stretched coordinates [57]. The strengths of the $\vec{l}_t \cdot \vec{s}$ and l_t^2 terms are dependent on N, by introducing N-dependent κ and μ parameters. A higher order hexadecapole deformation, $2\hbar\omega_0\rho^2\varepsilon_4 V_4(\gamma)$ is also included, where ρ is the radius in the stretched coordinate system.

In these calculations, the Hamiltonian is diagonalized using the eigenfunctions of the rotating oscillator [58], $|n_x n_2 n_3 \Sigma\rangle$, as basis states. The main advantage of the rotating basis is that N_{rot} can be treated as a good quantum number, where $N_{rot} = n_x + n_2 + n_3$. One advantage of these calculations over the shell-model calculations, is that the model space is practically unlimited.

Generally the CNS model is referred to as configuration dependent, because it becomes possible to make a rather detailed specification of configurations. In this approach they are specified by the number of particles with signature $\alpha = 1/2$ and $\alpha = -1/2$, respectively, in each N_{rot} shell. Furthermore, within each N_{rot}-shell, it is generally possible to distinguish between orbitals which have their main amplitudes in the high-j intruder shell and the low-j orbitals which have their main amplitudes in the other j-shells. In the $A \sim 60$ mass region, the involved shells are $N_{rot} = 3$ and $N_{rot} = 4$. For the $N_{rot} = 3$ shell, the $1f_{7/2}$ and for the $N_{rot} = 4$ shell, the $1g_{9/2}$ orbitals are considered as high-j. The remaining orbitals in the respective shells are treated as low-j.

Table 5.1: Occupation of different high- and low-j N_{rot} orbitals of different signature α for a ^{62}Zn proton configuration with one hole in $1f_{7/2}$ and one particle in $1g_{9/2}$.

	$N_{rot} =$	0	1	2	3	4	5
$\alpha = -1/2$	low-j	0	1	3	1	0	0
	high-j	1	2	3	3	0	0
$\alpha = +1/2$	low-j	0	1	3	1	0	0
	high-j	1	2	3	4	1	0

For $Z = 30$, the configuration with one proton hole in $1f_{7/2}$ and one proton particle in the $1g_{9/2}$ subshell, one way of filling of different high-j and low-j orbitals with different signatures $\alpha = \pm 1/2$ is shown in Table 5.1. Note, in an even N_{rot}-shell, for the intruder orbitals $\alpha = 1/2$ orbital occupation is favored, whereas in an odd N_{rot}-shell, the $\alpha = -1/2$ orbital occupation is favoured (see Figs. 5.3 and 5.8). In these calculations, the configurations are fixed, and the total energy for each configuration is then minimized in terms of deformation using the parameters specified above ($\varepsilon_2, \gamma, \varepsilon_4$). The calculations do not include pairing. Therefore, they are realistic at high spins, but they give at least a qualitative description of the lower-spin states.

5.3.1 Computer Calculations

In the practical calculations, the programs, which are illustrated in the flowchart of Fig. 5.2, need to be run. The calculations are performed with the standard values of the Nilsson parameters, κ and μ. In Table 5.2, the κ and μ' values of proton and neutrons for $N_{rot} = 0, 1, 2, 3, 4, 5$ are reported. Here $\mu' = \kappa \times \mu$. These are of empirical origin and taken

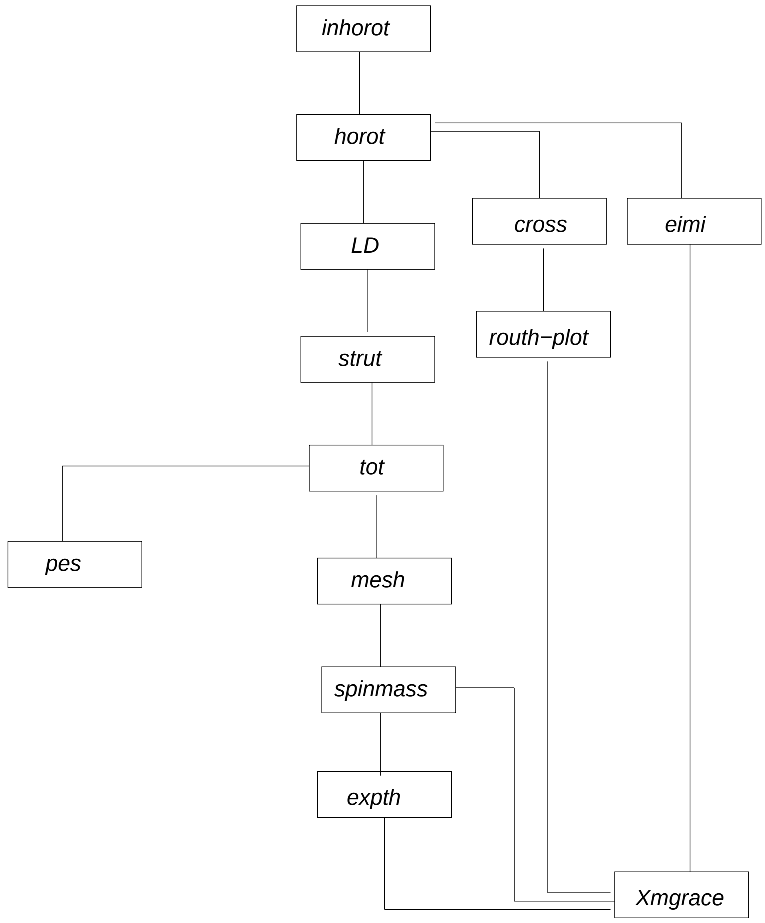

Figure 5.2: Illustration of the standard flow through the computer programs used in the CNS calculations. All these names refers to the corresponding programs in FORTRAN code.

Table 5.2: Nilsson parameters of different N_{rot} shells

N_{rot} =	protons	neutrons
	κ, μ'	κ, μ'
0	0.12, 0.0	0.12, 0.0
1	0.12, 0.0	0.12, 0.0
2	0.105, 0.0	0.105, 0.0
3	0.09, 0.027	0.09, 0.0225
4	0.065, 0.0370	0.07, 0.0273
5	0.060, 0.0390	0.062, 0.0266

from [55]. These values are slightly different for protons and neutrons and vary for the different N_{rot}-shells.

In the $inhorot$ program, one can define a mesh in the (ε_2, γ) deformation plane by introducing a Cartesian (x, y) coordinate system with the y-axis along the $\gamma = -120°/60°$

axis. The number of points in x- and y- directions, and the spacing between the points is selected. Each point in the mesh represents a specific value of ε_2 and γ. In addition, the number of points in ε_4 and their values are specified. The total number of points in a mesh are $N_x \cdot N_y \cdot N_{\varepsilon_4} \cdot N_\omega$. Here N_x and N_y are the number of points along x and y directions, of the (ε_2, γ) plane. N_{ε_4} and N_ω are the number of ε_4 and ω values, where ω is the rotational frequency. The $inhorot$ program creates an input file for $horot$. The $horot$ program is used to calculate the single-particle energies in the mesh points. For every deformation point in the mesh, the LD program will calculate the rotating liquid drop energies using the rigid body moments of inertia. Here the static liquid drop parameters are taken from the Lublin-Strasbourg drop (LSD) [56, 59]. The rigid body moments of inertia are calculated for a nucleus with a diffuse surface having a radius parameter r_0 = 1.16 fm and a diffuseness parameter, $a = 0.6$ fm [56, 59]. Renormalization of the static energy and moments of inertia is necessary in the Nilsson potential, so the total energies are Strutinsky renormalized [60, 61] to the rotating liquid-drop behaviour. The Strutinsky renormalization is carried out in $strut$ program.

The program tot is used for two purposes. One purpose is to perform the $scan$ calculations and another is to run for fixed configurations, like the example given in Table 5.1. The yrast states of the different combinations of parity and signature are searched in a $scan$ calculation. As already mentioned, in this approach it is possible to identify the orbitals having their main amplitudes in the j-shell with the largest j-value within each N_{rot}-shell. As a result, a large number of different configurations in the yrast region can be determined. The total spin is calculated as the sum of the expectation values of j_x for the occupied orbitals. The total energy E_{tot} at a specific deformation $(\varepsilon_2, \gamma, \varepsilon_4)$ and specific spin I is calculated as the sum of rotating liquid drop energy and the shell energy using the tot program.

The energy can be illustrated as potential energy surfaces in the (ε_2, γ)-plane and the plots are made in pes program. The $mesh$ program is used to make interpolations to find out the energy minima at each spin with respect to deformation. The $spinmass$ program is used to create input files to the plotting program like, energies vs. spin, $J^{(1)}$ and $J^{(2)}$ moments of inertia and nuclear shape trajectories in the deformation space as a function of I for different configurations. The plotting program $Xmgrace$ is used to create the different plots. To compare the calculated and experimental energies on an absolute scale, the $expth$ program is used.

Finally, to plot the single-particle energies as function of rotational frequency at a fixed deformation, and to plot single-particle energies e_i at a rotational symmetric deformation vs. m_i, the programs called $cross$, $routh$-$plot$ and $eimi$ need to be performed.

The results from these programs, which were applied to ^{62}Zn, are reported in the following sections.

5.3.2 Theoretical Interpretations on ^{62}Zn

The ground state of ^{62}Zn can be viewed as a ^{56}Ni core plus six valence nucleons outside the core. The orbitals which are involved in a theoretical description of ^{62}Zn include the $N = 3$ high-j $1f_{7/2}$ shell, the upper low-j fp shells $1f_{5/2}$, $2p_{3/2}$, and $2p_{1/2}$, and finally the $N = 4$ shell $1g_{9/2}$. The j-shells are pure only if the shape is spherical. In the deformed rotating potential, these j-shells will mix. i.e., in the present approximation the wave functions of the single-particle orbitals will have amplitudes in all the j-shells of a specific N_{rot}-shell. However, it turns out that if the deformation is not too large, these orbitals can be classified as

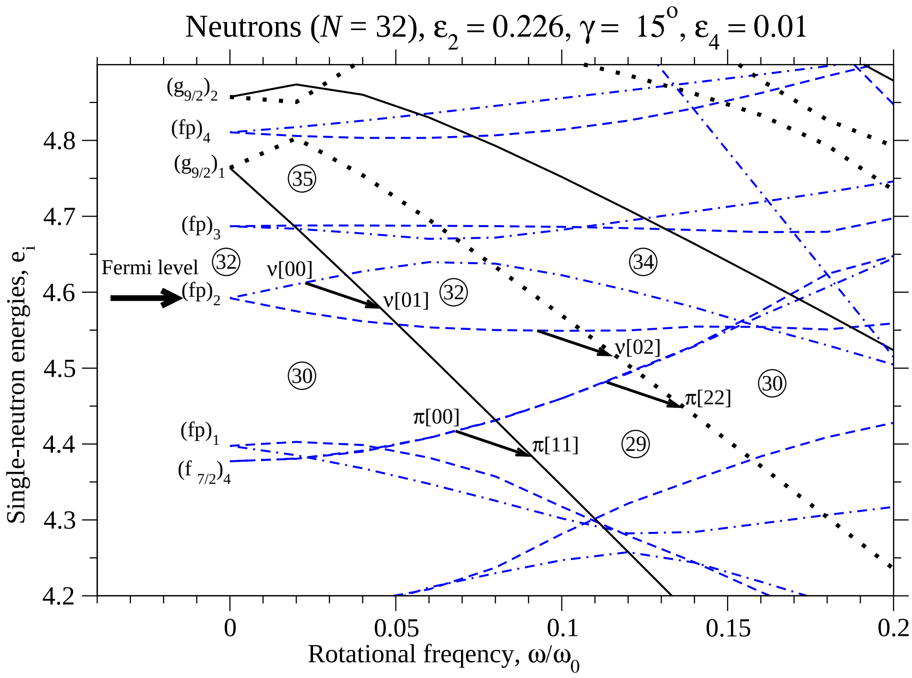

Figure 5.3: Single neutron orbitals, routhians, plotted as a function of rotational frequency, $\frac{\omega}{\omega_0}$. The energies are calculated at a constant deformation of $\varepsilon_2 = 0.226$, $\gamma = 15°$ and $\varepsilon_4 = 0.01$. The arrow on the left hand side indicates the Fermi level for $N = 32$ at $\omega = 0$. Particle numbers at some energy gaps are encircled. The orbitals are labelled by the group to which they belong and the ordering in the group at rotational frequency, $\omega = 0$. See text for details.

having their main amplitudes in either the high-j intruder shell or in the other shells with smaller j-values [1, 21].

Figure 5.3 shows the calculated single-particle orbitals (routhians) for neutrons as a function of the rotational frequency for a typical deformation for low-spin states, $\varepsilon_2 = 0.226$, $\gamma = 15°$ and $\varepsilon_4 = 0.01$. Due to the low Coulomb effects, the single-particle orbitals for protons and neutrons are almost identical. The main difference is the Fermi energy, which is higher for neutrons than for protons. Dashed lines are used for negative parity and dots for signature $\alpha = -1/2$, i.e. solid lines for $(\pi, \alpha) = (+, +1/2)$, dotted lines for $(+, -1/2)$, dashed lines for $(-, +1/2)$ and dot-dashed lines for $(-, -1/2)$. The orbitals are labelled according to which j-shell or group of j-shells they belong and the ordering in the group at rotational frequency $\omega = 0$. The (fp) group indicates the mixing of the $1f_{5/2}$ and $2p_{3/2}$ subshells. It is not really possible to make a distinction between the $1f_{5/2}$ and $2p_{3/2}$ shells. The mixing probability of the $2p_{1/2}$ subshell is low for these orbitals and does not contribute significantly to the wave-functions of the upper fp shell orbits which are active in ^{62}Zn. The large signature splitting of the lowest high-j $1g_{9/2}$ intruder orbital means that for configurations with one $1g_{9/2}$ neutron (or proton), one expects to observe only the favoured $\alpha = +1/2$ signature.

The short-hand notation of each rotational band is based on the number of particles in different j-shells for each configuration, see Table 5.1. In general the labelling refers to the dominating shell only, while the wave functions also contain components from other

j-shells. A configuration can be written as:

$$\pi[(1f_{7/2})^{-p_1}(1g_{9/2})^{p_2}(fp)^{p_3}] \otimes \nu[(1f_{7/2})^{-n_1}(1g_{9/2})^{n_2}\nu(fp)^{n_3}] \tag{5.12}$$

which provides a possibility of giving the short-hand notation [p_1p_2,n_1n_2]. Here p_1 (n_1) denotes the number of $1f_{7/2}$ proton (neutron) holes and p_2 (n_2) number of $1g_{9/2}$ protons (neutrons). The parameter p_3 (n_3) denotes the number of particles in the low-j fp-subshells ($1f_{5/2}$, $2p_{3/2}$, and $2p_{1/2}$). They are fixed to get the correct number of particles, i.e $p_3 = 2{+}p_1{-}p_2$ and $n_3 = 4 + n_1 - n_2$ for ^{62}Zn. The signature of an odd number of fp- particles is sometimes specified as $[p_1p_2(+/-), n_1n_2(+/-)]$ for signature $\alpha = +1/2$ and $\alpha = -1/2$, respectively.

In the ground state of ^{62}Zn only the low-j $N_{rot} = 3$ shells are occupied. More deformed, higher-spin configurations are formed by making particle excitations into the deformation-driving $1g_{9/2}$ orbitals and/or generating holes in the $1f_{7/2}$ orbitals. For example, as shown in Fig. 5.3, the lowest possible neutron configuration $\nu[(fp)^4]$ is labelled as ν[00]. At $\frac{\omega}{\omega_0} \approx 0.03$, the $\alpha = -1/2$ $(fp)_2$ and the favoured $(\mathrm{g}_{9/2})_1$ orbitals cross, which means that the occupation of the $\alpha = 1/2$ $(1g_{9/2})_1$ neutron orbital is favoured in energy at frequencies $\frac{\omega}{\omega_0} \gtrsim 0.03$. The corresponding configuration $\nu[(fp)^3(1g_{9/2})^1]$ is labelled ν[01]. At $\frac{\omega}{\omega_0} \approx 0.11$, the $\alpha = 1/2$ $(fp)_2$ and the $\alpha = -1/2$ $(\mathrm{g}_{9/2})_1$ orbitals cross, so that the occupation of the $\alpha = -1/2$ $(\mathrm{g}_{9/2})_1$ orbital is favoured at $\frac{\omega}{\omega_0} \gtrsim 0.11$. The corresponding configuration $\nu[(fp)^2(1g_{9/2})^2]$ is labelled as ν[02].

For the protons the signature degenerate $(1f_{7/2})_4$ orbitals cross the $(1g_{9/2})_1$ orbital at $\frac{\omega}{\omega_0} \approx 0.08$. At higher frequencies the occupation of the $\alpha = 1/2$ $(1g_{9/2})_1$ orbital together with one of the $(1f_{7/2})_4$ orbitals is favoured. The corresponding configuration $\pi[(1f_{7/2})^{-1}(1g_{9/2})^1]$ is labelled π[11]. At $\frac{\omega}{\omega_0} \approx 0.12$ the $(1f_{7/2})_4$ orbitals cross the $\alpha = -1/2$ $(1g_{9/2})_1$ orbital, so that the occupation of two $(1g_{9/2})_1$, and no $(1f_{7/2})_4$ orbitals, is favoured at higher frequencies. The corresponding configuration $\pi[(1f_{7/2})^{-2}(1g_{9/2})^2$] labelled as π[22]. Returning to the neutrons, at $\frac{\omega}{\omega_0} \approx 0.15$ the orbitals $(1f_{7/2})_4$ and $(fp)_2$ cross, so that at higher frequencies it is favourable to make also two neutron holes in the $(1f_{7/2})_4$ orbitals. All these orbital crossings occur at a constant deformation of $\varepsilon_2 = 0.226$ and $\gamma = 15°$, $\varepsilon_4 = 0.01$, but they give a basic idea of which configurations are favoured in general.

5.3.3 Predictions on Low and Medium-spin Structures

Figure 5.4 shows the calculated energies for a selection of fixed configurations in the yrast region of ^{62}Zn, drawn relative to the liquid drop energy. The solid (dashed) lines correspond to positive (negative) parity states and filled (open) symbols correspond to a signature of $\alpha = 0(1)$. The aligned states at, or very close to, $\gamma = 60°$ are encircled. The band configurations shown in panel (a) have no particle excitations from $1f_{7/2}$, whereas the bands displayed in panel (b) have one proton hole in $1f_{7/2}$. Thus the maximum spin for the configurations in panel (a) is 10 to 19$\hbar$ and in panel (b) 14 to 26$\hbar$ (see below). All configurations are labelled with the shorthand notation [p_1p_2,n_1n_2].

With 2 protons and 4 neutrons outside the $Z = N = 28$ shell gap, the lowest spin configuration is labelled as [00,00] with $I_{max} = 10^+$, corresponding to the ground state band ND1. By exciting one (fp) neutron into the intruder $1g_{9/2}$ shell, the configuration $\pi[(fp)^2_4] \otimes \nu[(fp)^3_{4.5}(1g_{9/2})^1_{4.5}]$ is formed. It is labelled as $[00, 01(+)]$ and terminating at $I_{max} = 13^-$. The other signature configuration $\pi[(fp)^2_4] \otimes \nu[(fp)^3_{5.5}(1g_{9/2})^1_{4.5}]$ labelled as $[00, 01(-)]$ is termi-

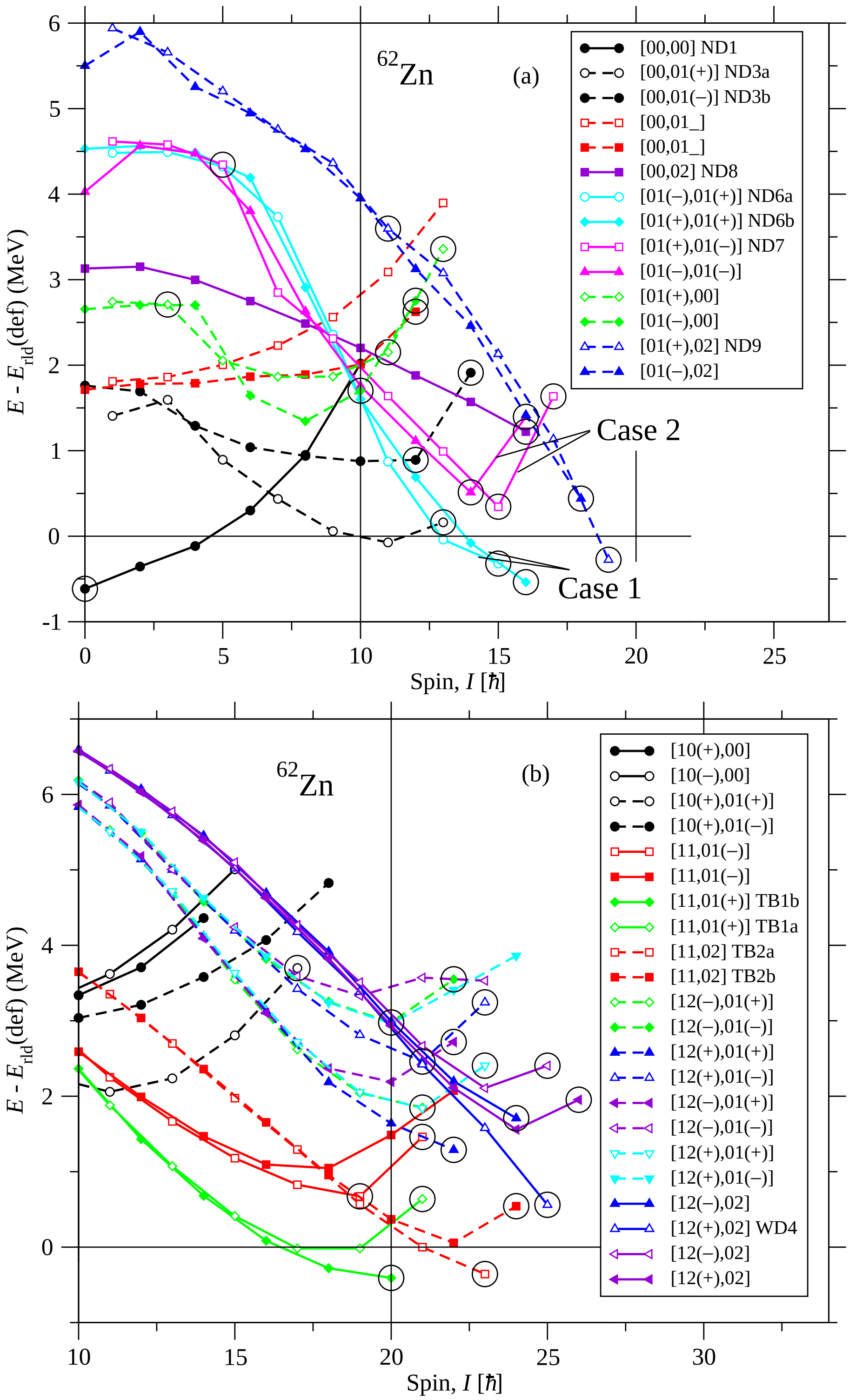

Figure 5.4: Calculated energies for a selection of fixed configurations in the yrast region of ^{62}Zn, drawn relative to the rotating liquid drop energy. The positive (negative) parity states are represented with solid (dashed) lines and filled (open) symbols belong to a signature of $\alpha = 0(1)$. Non-collective aligned states are encircled. The configurations in panel (a) are illustrated for no particle excitations, whereas those in panel (b) are for one proton particle excitation across the $Z = N = 28$ shell gap. See text for details.

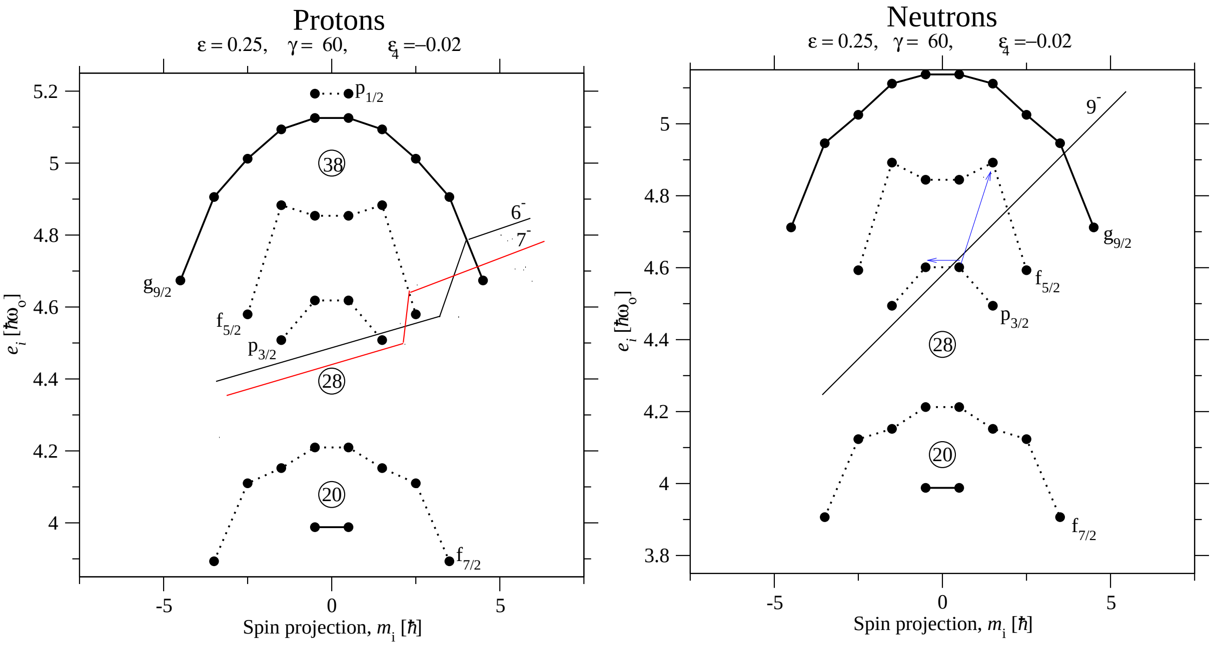

Figure 5.5: The sequence of the proton and neutron single-particle states drawn as energy vs. spin projection and the position of the respective sloping Fermi surfaces relative to the single particle levels. See text for more details.

nating at $I_{max} = 14^-$. The subscripts indicate the maximum spin contribution from each j-shell or group of j-shells. These two calculated signature partner configurations are in good agreement with the experimentally observed ND3 structure with two signatures ND3a and ND3b (see below).

In the configuration labelled [00,01$_-$], the minus sign indicates that the $g_{9/2}$ neutron occupies the unfavoured signature, orbital $\alpha = -1/2$. Because of the large signature splitting for this intruder orbital, the [00,01$_-$] configurations with signatures $\alpha = \pm 1/2$ for the (fp) neutrons are at higher energy than other similar configurations discussed above. The configuration with two neutrons in $1g_{9/2}$, which is labelled as [00,02] can be assigned to observed ND8.

The configuration with one proton in the $1g_{9/2}$ subshell, $\pi(1g_{9/2})^1$ combined with the neutron configuration $\nu(1g_{9/2})^1$, results in two pairs of signature partners which are marked with case 1 and case 2 inside the figure. The case 1 configuration [01(+),01(+)] terminates in the state, $\pi[(fp)^1_{2.5}(1g_{9/2})^1_{4.5}] \otimes \nu[(fp)^3_{4.5}(1g_{9/2})^1_{4.5}]$ i.e at $I_{max} = 16^+$. In the other signature partner configuration, $[01(+), 01(-)]$, the spin of the (fp) proton is 1.5 instead in the terminating $I_{max} = 15^+$ state. In a similar way, the case 2 signature partner configurations $[01(-), 01(+)]$ and $[01(-), 01(-)]$ are terminating at $I_{max} = 17^+$ and $I_{max} = 16^+$ respectively. It is clearly seen in the figure, that the case 2 configurations are at higher energy than the case 1 configurations at their terminating spin states.
This can be understood from Fig. 5.5, which illustrates the single-particle energies at an axial symmetric deformation drawn vs. their projection of the single-particle angular momentum m_i on the symmetry axis. The orbitals are connected and labelled by the respective j-shells where they have their main amplitudes. In sloping Fermi surface diagrams [48, 61], favoured

aligned states are formed in configurations defined by straight-line, or close-to-straight-line Fermi surfaces, where all orbitals below the Fermi surface are occupied and those above are empty.

Figure 5.5 is drawn at the deformation found for the $I_{max} = 15^+$ terminating state. With approximately the same deformation for the other aligned [01,01] states, it is now possible to draw the Fermi surfaces in the figure. The two signature partner proton configurations have a similar energy cost per spin unit in the terminating state as seen from the corresponding Fermi surfaces drawn with a solid red and black lines in a panel (a). For the neutron configurations on the other hand, the energy cost per spin unit is different in case 1 and case 2 as can be understood from panel (b).

Thus in case 1, the third (fp) neutron is in the $2p_{3/2,m=1/2}$ orbital corresponding to a straight-line Fermi surface, see panel (b), and thus favoured in energy. In case 2 with opposite signature, the third (fp) neutron can be moved to the $2p_{3/2,m=-1/2}$ orbital resulting in aligned states at $I = 14, 15$ with rather low energies. Then, however, the maximum spin in these configurations are obtained with the third (fp) neutron in the $f_{5/2,m=3/2}$ orbital instead. As seen in panel (b), this orbital is very high in energy relative to the straight line Fermi surface corresponding to a kink for case 2 in Fig. 5.4 with high-lying $I = 16, 17$ states. The high energy of the 14^- state in the [00,01($-$)] configuration is explained by the same mechanism.

The [01,01] signature partner of the case 1 configurations are in nice agreement with experimentally observed ND6 structure with signature partners ND6a and ND6b. The highest spin state of $[01(+), 01(-)]$ configuration can be assigned to the observed band ND7. With two neutrons in $1g_{9/2}$, the signature partner configurations $[01(+), 02]$, $[01(-), 02]$ are terminating at maximum spin 19^- and 18^-. The former configuration fits well with the experimentally observed ND9 structure. The other signature partner configuration is not observed experimentally.

The configurations shown in Fig. 5.4 (b) have one proton hole in $1f_{7/2}$. The $[11, 01(+)]$ configuration with one proton and one neutron in $1g_{9/2}$ terminates at $I_{max} = 20^+, 21^+$ in the states

$$\pi[(1f_{7/2})^{-1}_{2.5,3.5}(fp)^2_4(1g_{9/2})^1_{4.5}]_{11,12} \otimes \nu[(fp)^3_{4.5}(1g_{9/2})^1_{4.5}]_9. \quad (5.13)$$

These two configurations are in good agreement with the observed terminating band TB1 with signature partners TB1a and TB1b, respectively. The other combination of signature partner bands [11,01($-$)] are higher in energy with one neutron in the unfavoured signature $\alpha = -1/2$ branch of the $(fp)_2$ orbital (see Fig. 5.3).

With one more neutron in $1g_{9/2}$, signature partner configurations [11,02] are formed. They terminate at $I_{max} = 23^-, 24^-$ in the states

$$\pi[(1f_{7/2})^{-1}_{2.5,3.5}(fp)^2_4(1g_{9/2})^1_{4.5}]_{11,12} \otimes \nu[(fp)^2_4(1g_{9/2})^2_8]_{12}. \quad (5.14)$$

These two calculated signature partner bands are in good agreement with the observed terminating signature partner bands TB2a and TB2b. The calculated bands with the configuration [12,02] have the highest terminating spins in Fig. 5.4, $I_{max} = 22 - 26^+$. The [12(+),02] band with $I_{max} = 25^+$ can be assigned to the observed band WD4.

In addition to the bands discussed here, additional bands of the type [10,00], [10,01] and [12,01] are shown in Fig. 5.4 (b). They are formed with different combinations of the signatures for the $1f_{7/2}$ proton hole and for the (fp) proton and neutron. They are all calculated at a rather high energy and appear not to have experimental correspondences.

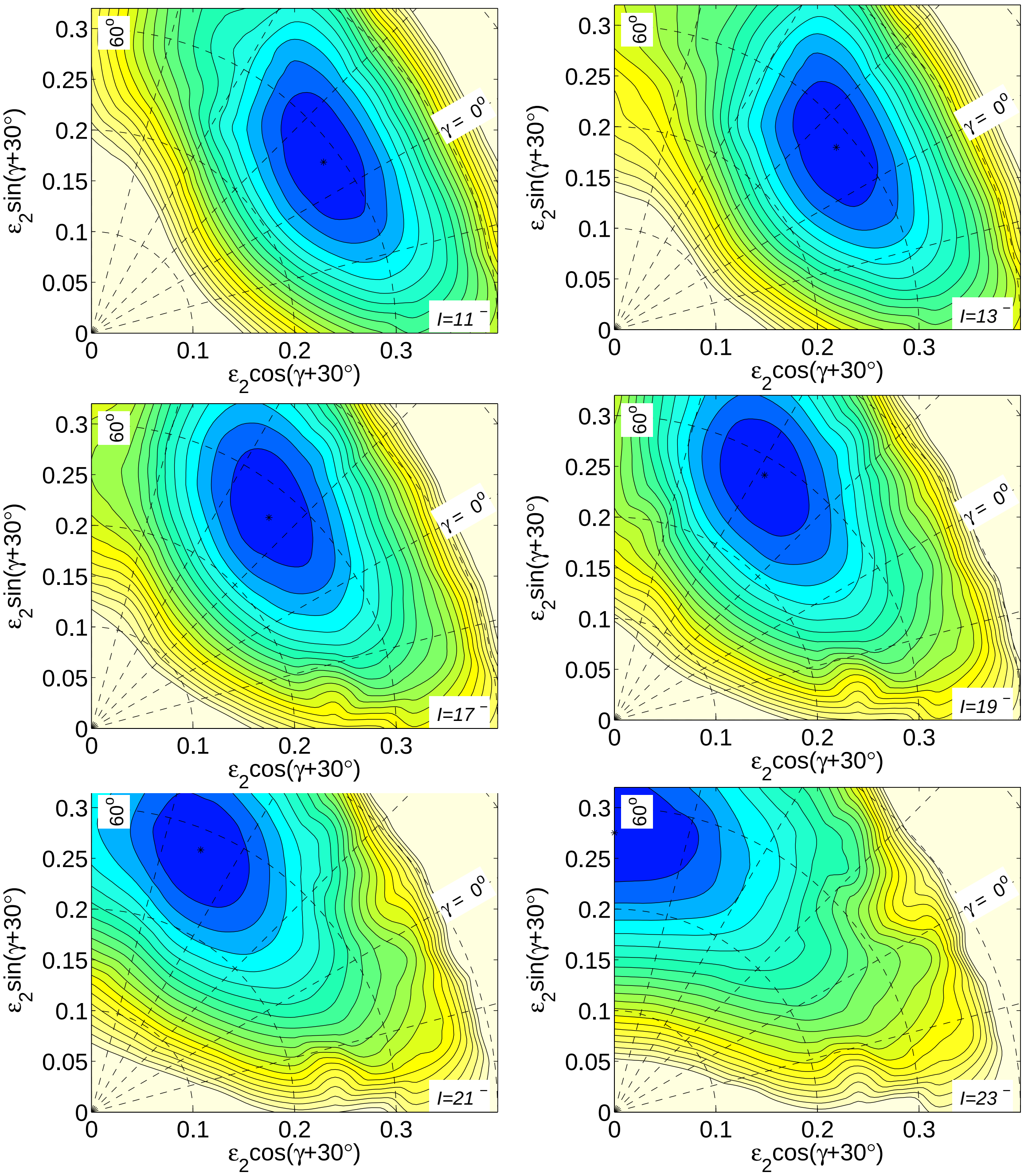

Figure 5.6: Calculated potential energy surfaces for the [11,02] configuration with negative parity and $\alpha = 1$ signature. The contour line separation is 0.2 MeV. See text for details.

Figure 5.6 shows the calculated total potential energy surfaces for the [11,02] configuration with negative parity and signature $\alpha = 1$. The calculated maximum spin for this configuration is $I_{max} = 23^-$. In these figures, the contour line separation is 0.2 MeV. The lowest energy minima are indicated with filled black circles. For the lowest spin values $I = 11^-, 13^-$ shown in the figure, the lowest energy is found at γ = 0° - 20°, indicating a large collectivity at these spin values. For medium spin values $I = 17^-, 19^-, 21^-$, the minimum is located at γ = 20° - 40°, indicating reduced collectivity. For the maximum spin value of [11,02] at $I = 23^-$, the lowest minimum is at $\gamma = 60°$ corresponding to a non-collective state. This type of non-collective yrast states at $\gamma = 60°$ are encircled in the $E - E_{rld}$ plots.

5.3.4 Predictions on Well-deformed Structures

Figure 5.7 is analogous to Fig. 5.4, but the configurations in panel (a) have one proton hole and one neutron hole in the $1f_{7/2}$ shell, while those in panel (b) have two proton holes in the $1f_{7/2}$ shell. The highest spin for the configurations in both panels is 24 to 30$\hbar$. All configurations in Fig. 5.7 are labelled with the shorthand notation [p_1p_2,n_1n_2].

The [11,11] configuration with one proton and one neutron in the $1g_{9/2}$ subshell, results in two pairs of signature partners. These calculated bands are at a rather high energy with no observed bands assigned to them.

With one more neutron in $1g_{9/2}$, four pairs of signature partner configurations with negative parity $[11, 12(+/-)]$ are formed. With the same convention as in Fig. 5.4, the $(+/-)$ sign indicates signature of the (fp) particle. The lowest calculated signature partner bands terminate at $I_{max} = 26^-, 27^-, 27^-, 28^-$ in the states

$$\pi[(1f_{7/2})^{-1}_{2.5,3.5}(fp)^2_4(1g_{9/2})^1_{4.5}]_{11,12} \otimes \nu[(1f_{7/2})^{-1}_{2.5,3.5}(fp)^3_{4.5}(1g_{9/2})^2_8]_{15,16}. \tag{5.15}$$

Two of these calculated signature bands can be assigned to the observed WD2a and WD2b bands. The other negative signature configuration may be associated with the observed bands WD5 or WD6.

With three neutrons in $1g_{9/2}$, two pairs of signature partner configurations [11,13] are formed. The lowest positive signature band of this type 'terminates' at $I_{max} = 28^+$, and can be assigned to the observed band WD7. No observed bands are assigned to the other [11,13] bands.

The $[21(+/-), 01(+/-)]$ configuration in Fig. 5.7 (b) with one proton and one neutron in $1g_{9/2}$, results in four bands with a rather large signature splitting. All these calculated bands are at a rather high energy. The lowest energy configuration $[21(+), 01(+)]$ terminates at $I_{max} = 24^+$ in the state

$$\pi[(1f_{7/2})^{-2}_6(fp)^3_{4.5}(1g_{9/2})^1_{4.5}]_{15} \otimes \nu[(fp)^3_{4.5}(1g_{9/2})^1_{4.5}]_9 \tag{5.16}$$

This configuration can be assigned to the observed band WD9.

With one proton and two neutrons in $1g_{9/2}$, one pair of signature partner configurations $[21(+/-), 02]$ is formed. The odd spin partner ($\alpha = 1$) is lower in energy than even spin band ($\alpha = 0$) . The maximum spin for these two bands are at $I_{max} = 27^-, 28^-$ in the state

$$\pi[(1f_{7/2})^{-2}_6(fp)^3_{4.5,5.5}(1g_{9/2})^1_{4.5}]_{15,16} \otimes \nu[(fp)^2_4(1g_{9/2})^2_8]_{12} \tag{5.17}$$

The odd spin band $[21(+), 02]$ is appears to be associated with the observed WD5 and WD6 bands. Both of these bands are at a comparatively low energy. More details on these assignments for WD5 and WD6 are explained in Sec 5.4.1.

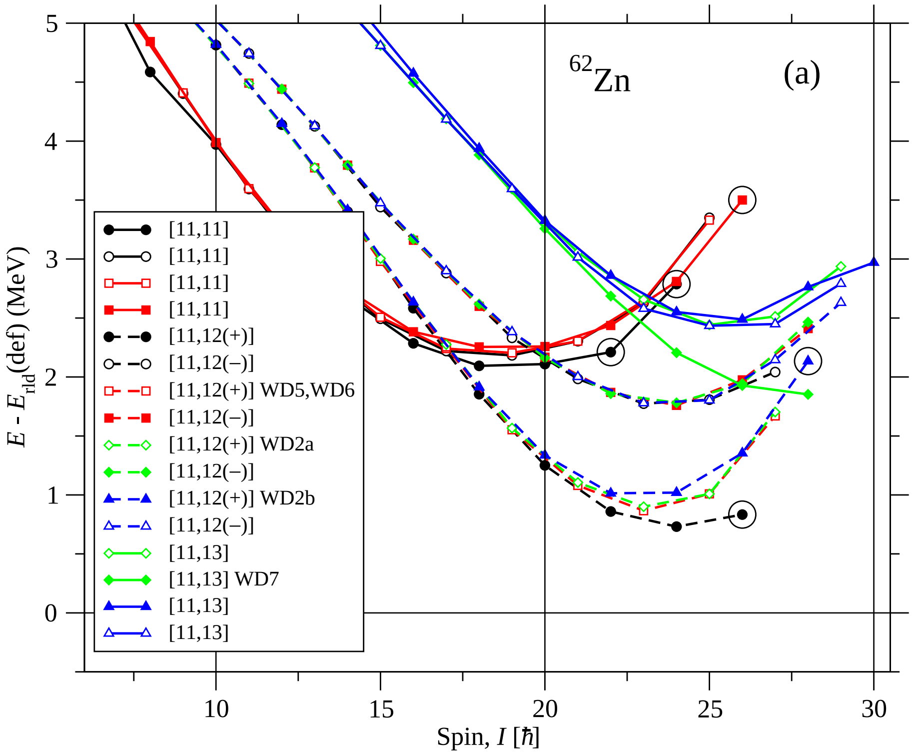

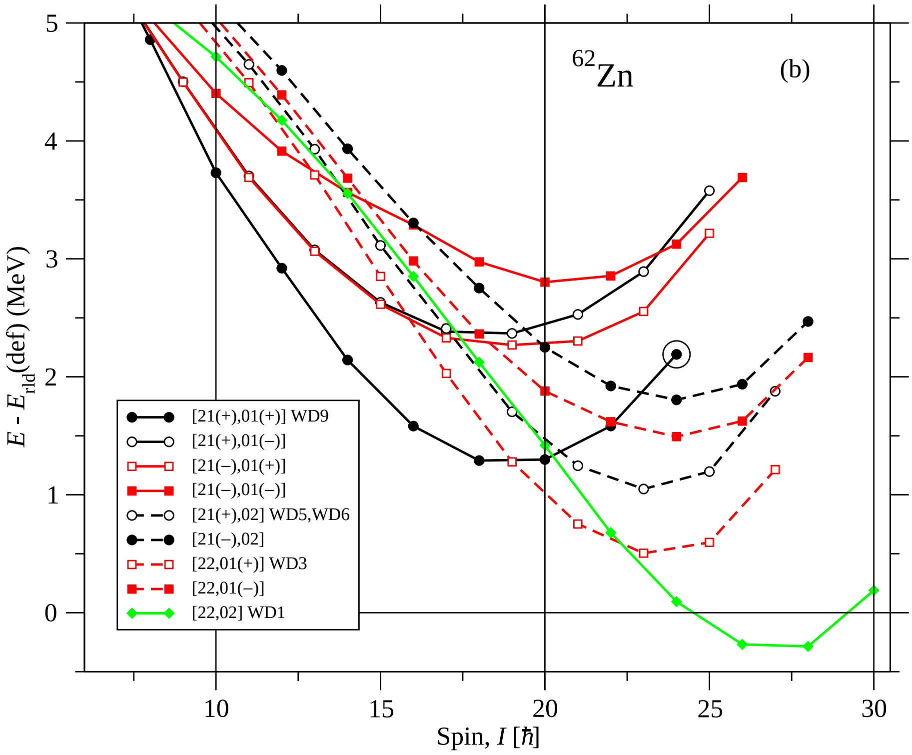

Figure 5.7: Same as Fig. 5.4 but here illustrated (a) with one proton and neutron hole in the $1f_{7/2}$ shell, and (b) with two proton holes in the $1f_{7/2}$ shell. See text for details.

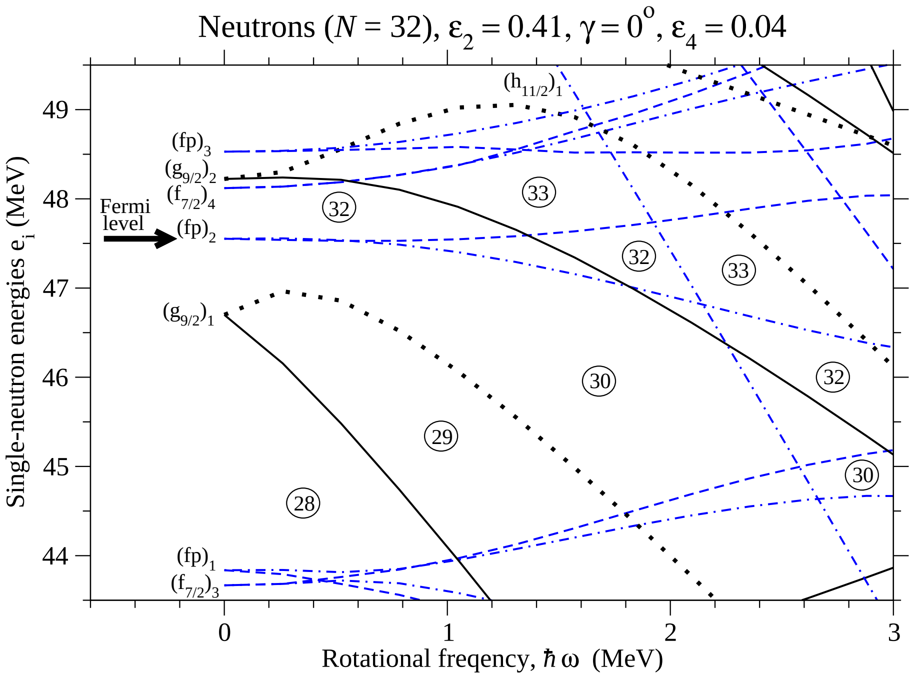

Figure 5.8: Single neutron orbitals, routhians, plotted as a function of rotational frequency, $\hbar\omega$. The energies are calculated for ${}^{62}_{30}\mathrm{Zn}_{32}$ at a constant deformation of $\varepsilon_2 = 0.41$, $\gamma = 0°$ and $\varepsilon_4 = 0.04$. The arrow indicates the Fermi level at $\omega = 0$. Particle numbers at some gaps are encircled. The orbitals are labelled by the group to which they belong and the ordering in the group at rotational frequency, $\omega = 0$. See text for details.

The configuration [22,01(+)] has an $I_{max} = 27^-$ state,

$$\pi[(1f_{7/2})_6^{-2}(fp)_4^2(1g_{9/2})_8^2]_{18} \otimes \nu[(fp)_{4.5}^3(1g_{9/2})_{4.5}^1]_9 \tag{5.18}$$

This configuration is in good agreement with the observed WD3 band. The other calculated signature partner band $[22, 01(-)]$ is at a rather high energy, with no experimental correspondence. The [22,02] configuration has $I_{max} = 30^+$ corresponding to the state

$$\pi[(1f_{7/2})_6^{-2}(fp)_4^2(1g_{9/2})_8^2]_{18} \otimes \nu[(fp)_4^2(1g_{9/2})_8^2]_{12} \tag{5.19}$$

This configuration is in good agreement with the observed WD1 band [45].

5.3.5 Predictions on Superdeformed Structures

Figure 5.8 illustrates the single-neutron orbitals plotted as a function of rotational frequency, $\hbar\omega$, at a typical deformation for the SD bands, $\varepsilon_2 = 0.41$, $\gamma = 0°$ and $\varepsilon_4 = 0.04$. As already mentioned, the single-particle orbitals for protons and neutrons are almost identical. For $Z = 30$, the π[22] configuration is favoured in a large frequency range up to $\hbar\omega \lesssim 2.3$ MeV. At $\hbar\omega \lesssim 1.5$ MeV for $N = 32$, the $\alpha = (+/-)1/2\ (fp)_2$ are the favoured orbitals to fill for the two neutrons above the 30 gap. Therefore, the ν[22] configuration is favoured for $\hbar\omega \lesssim 1.5$ MeV. At $\hbar\omega \approx 1.5$ MeV the $\alpha = -1/2\ (fp)_2$ and the favoured $(1g_{9/2})_2$ orbitals cross, which means that the occupation of the $\alpha = 1/2\ (fp)_2$ and the favoured $(1g_{9/2})_2$ neutron orbitals

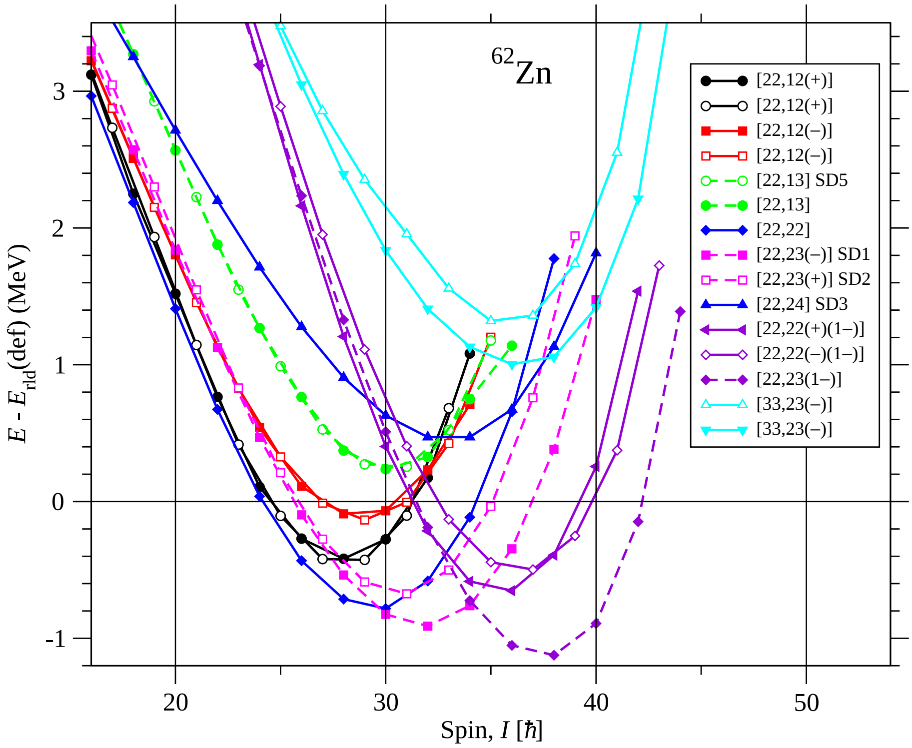

Figure 5.9: Same as Fig. 5.4 but here illustrated for the lowest possible selected calculated bands which have two or three proton holes in the $1f_{7/2}$ shell and one or two neutron holes in the $1f_{7/2}$ shell. See text for details.

are lowest in energy at frequencies $\hbar\omega \gtrsim 1.5$ MeV. At $\hbar\omega \approx 2.3$ MeV the $\alpha = -1/2$ $h_{11/2}$ orbital crosses the lowest $(fp)_2$ orbital. Thus, at higher frequencies, the occupation of the $\alpha = -1/2$ $1h_{11/2}$ orbital together with the $\alpha = 1/2$ $(1g_{9/2})_2$ orbital is favoured for $N = 32$. At $\hbar\omega \approx 2.6$ MeV for $Z = 30$ the $\alpha = -1/2$ $1h_{11/2}$ orbital crosses the $(1f_{7/2})_3$ orbitals, so at higher frequencies at this deformation, it is favourable to fill one $1h_{11/2}$ orbital also for the protons.

Figure 5.9 illustrates selected calculated bands with the proton configuration corresponding to the large $Z = 30$ gap in Fig. 5.8 combined with neutron configurations, where two orbitals above this gap are occupied. In addition, two configurations with a third $1f_{7/2}$ proton hole are included. The maximum spin values for these bands are in the range 33 to $44\hbar$.

The favoured proton configuration [22] combined with the neutron configuration $[12(+/-)]$ with one neutron hole in $1f_{7/2}$ shell and two neutrons in $1g_{9/2}$ shells, leads to two pairs of signature partner bands. There is no experimental evidence for any of these bands. With one more neutron excited to $1g_{9/2}$, negative parity configurations are formed, which are thus possible assignments for the SD1 and SD2 bands. With the third neutron in the favoured signature of the $(1g_{9/2})_2$ orbital, the signature partner configurations [22,13] and $[22, 23(+/-)]$ are formed, depending on whether the neutron is excited from the (fp) or $(1f_{7/2})$ orbitals. The [22,23] bands are calculated at a lower energy than the [22,13] bands, so they are our preferred choice for the observed SD1 and SD2 bands [45]. The negative signature partner of

Table 5.3: Experimentally observed structures are shown to illustrate their configuration assignments. Horizontal rows illustrate the proton configurations and the vertical columns give neutron configurations with their respective I_{max} values. For each combined neutron and proton configuration the maximum spin is indicated and also the experimental bands in ^{62}Zn, which are assigned to the configurations.

Config. ν π I_{max}	00] 6	01(+)] 9	01(-)] 10	02] 12	12(+)] 15, 16	13] 17	22] 20	23(+/-)] 21, 22	24] 22	22(1-)] 24, 25	23(1-)] 26
[00 4	ND1 10	ND3a 13	ND3b 14	ND8 16	20	21	24	25, 26	26	28, 29	30
[01(+) 7	13	ND6b 16	ND7 17	ND9 19	23	24	27	28, 29	29	31, 32	33
[01(-) 8	14	ND6a 17	18	20	24	25	28	29, 30	30	32, 33	44
[11 11,12	17 18	TB1b TB1a 20, 21	21 22	TB2a TB2b 23, 24	WD2a WD2b WD5, WD6 27, 28 26,27	WD7 28	31 32	32, 33 33, 34	33 34	35, 36 36, 37	37 38
[12(+) 13	19	22	23	WD4 25	29	30	33	34, 35	35	37, 38	39
[21(+) 15	21	WD9 24	25	WD5, WD6 27	31	32	35	36, 37	37	39, 40	41
[22 18	24	WD3 27	28	WD1 30	34	SD5 35	38	SD2, SD1 39, 40	SD3 40	42, 43	44
[33 21,22	27 28	30 31	31 32	33 34	37 38	38 39	41 42	42, 44 43, 44	43 44	45, 46 46, 47	47 48

[22,13] configuration is a possible candidate for observed SD5 band, while the other positive signature partner band is not observed experimentally.

There are two configurations, [22,22] and [22,24], which can be assigned to the observed SD3 band, but none of them is an ideal choice [45].

Considering the rather strong down-slope around $I = 30$ for the $E - E_{rld}$ curve of the SD4 band, it appears that the calculated configurations discussed so far are not possible assignments. Higher spin configurations are achieved by exciting one neutron to the favoured $h_{11/2}$ orbital or by exciting one proton from the $1f_{7/2}$ orbital. The lowest energy bands of this kind are drawn in Fig. 5.9, where the occupation of the $\alpha = -1/2\ h_{11/2}$ orbital is shown in parentheses, $(1-)$. One band of this type might be assigned to the observed SD4 band.

5.4 Configuration Assignments for Observed Bands

An overview of the results from the matching between the experimental structures and calculated configurations is found in Table 5.3. Different proton (rows) and neutron (columns) configurations are combined and the maximum spin for each combination is given.

5.4.1 More Details on Assignments

Figures 5.10 and 5.11 illustrate the configuration assignments for the observed bands with positive and negative parity, respectively. In both figures the observed bands have maximum spin $\leq 25\hbar$. The low-spin ND bands, the previously known two terminating bands, and one high-spin deformed band (WD4) are shown in the top panels with the configurations assigned to them in the middle panels and the difference in energy between the two in the bottom panels. In the top and middle panels, the y-axis corresponds to the energy with the rotating liquid drop (rld) energy subtracted [56]. The positive (negative) parity bands have an even (odd) number of $1g_{9/2}$ particles and it is instructive to see how the bands split up in groups with different I_{max} values depending on the number of $1g_{9/2}$ particles.
As we already discussed many details about the calculated configurations in section 5.2.2, we only specify those configurations which correspond to the best fit of the observed bands here.

The observed ground state structure ND1 is assigned to [00,00]. By lifting particles from the fp orbitals to the $g_{9/2}$ orbitals, we successively obtain the $[00, 01(+/-)]$ configurations which are assigned to the ND3a and ND3b bands, [00,02] assigned to ND8 , $[01(+/-), 01(+)]$ assigned to ND6a and ND6b, the two highest spin state of $[01(+), 01(-)]$ assigned to ND7 and finally $[01(+), 02]$ assigned to ND9. Note especially that with more particles in the high-j $1g_{9/2}$ orbitals, the terminating sequences become more down-sloping.

If we proceed in the same way, for the configurations with one proton hole in $1f_{7/2}$, the signature partner configurations $[11, 01(+)]$ are assigned to TB1a and TB1b, and the [11,02] configurations are in good agreement with the observed TB2a and TB2b bands. Finally the [12(+),02] configuration agrees well with observed WD4 structure.

Except for the ground state band ND1 and the highest spin state in the ND3 and ND7 configurations, the differences in the lower panels of Fig. 5.10 and 5.11 are fairly constant for the different structures and fall within $\pm$ 1 MeV. The highest spin states of ND3 and ND7 are both formed with the third fp neutron in the $1f_{5/2,m=3/2}$ orbital, (see Fig. 5.5). The discrepancy suggests that the $1f_{5/2}$ neutron subshell is at a too high energy with present parameters (κ and μ). Because $I^{\pi} = 14^{-}$ and 17^{+} is the highest spin with can be formed with $1f_{7/2}$ hole and one and two $1g_{9/2}$ particles, respectively, the possibility that these states should be assigned to another configuration appears excluded because more proton holes in $1f_{7/2}$ would lead to a higher energy. It appears that ND2 and ND4 might rather be described as vibrations while ND5 is not a regular structure. Therefore, the structures ND2, ND4, and ND5 are not assigned to any configurations.

Figure 5.12 is analogous to Fig. 5.10 but here the illustrated bands correspond to one proton and one neutron hole in $1f_{7/2}$, for both positive and negative parity high-spin structures with maximum spin $I \leq 30\hbar$. Figure 5.13 is analogous to Fig. 5.12 but with two proton holes in $1f_{7/2}$.

With two proton holes, the configuration can be described as built from a ${}^{60}_{29}\mathrm{Cu}_{31}$ core

$$\pi(f_{7/2})^{-2}(fp)^{2}(g_{9/2})^{1}\nu(fp)^{2}(g_{9/2})^{1} \tag{5.20}$$

with one proton and one neutron outside. Low energy bands are obtained if the proton and neutron are placed either in the $\alpha = +1/2(fp)_2$ orbital or in the $\alpha = -1/2(g_{9/2})_1$ orbital, which thus leads to four combinations which can all be assigned to observed bands (see Fig. 5.13); WD9 with both particles in the fp orbitals, WD3 and WD6-5 with one particle lifted to $1g_{9/2}$, and WD1 with both particles in $1g_{9/2}$. The WD6-5 band is a mixture of WD5

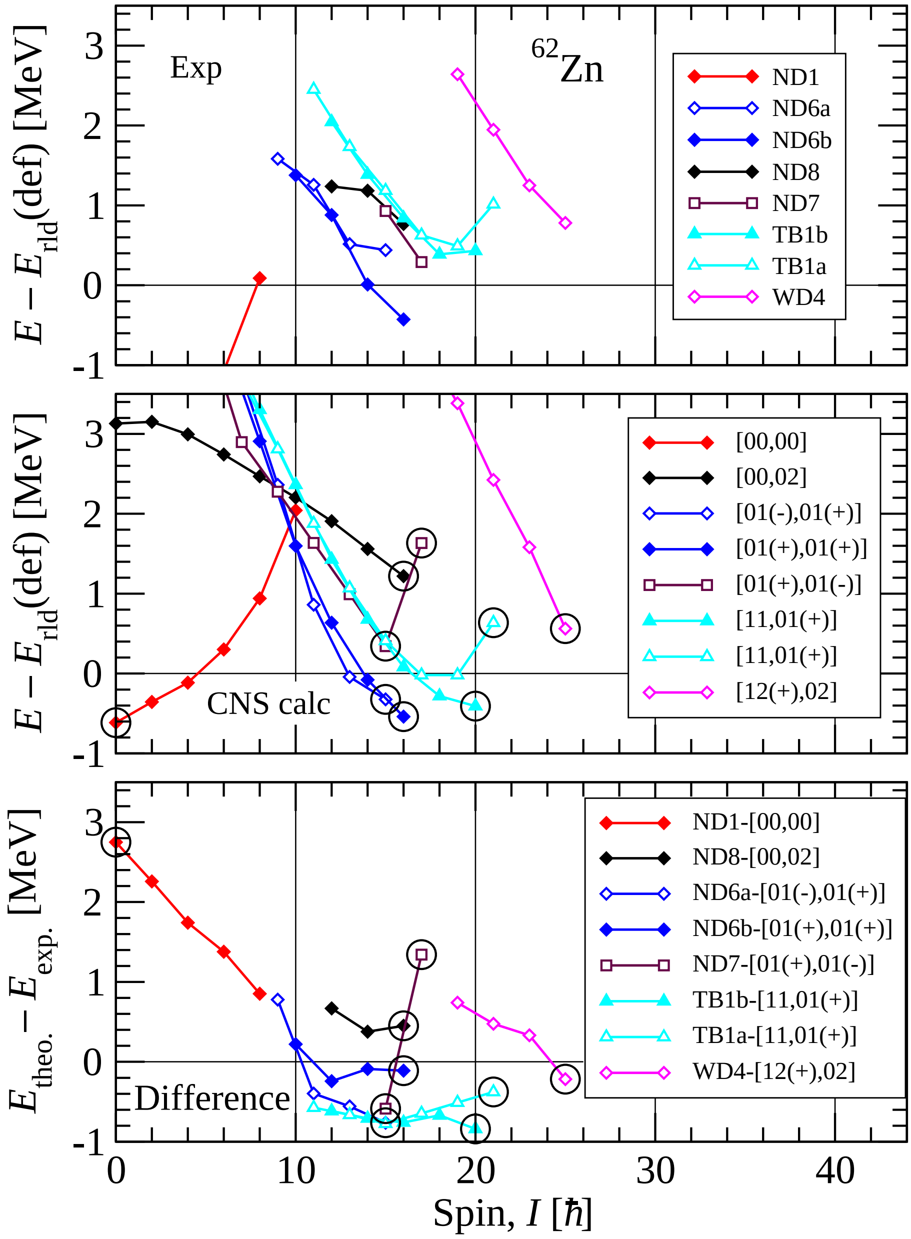

Figure 5.10: Comparison between experimentally observed structures and cranked Nilsson-Strutinsky predictions for observed positive-parity bands with $I_{max} \lesssim 25\hbar$ in ^{62}Zn. The top panel illustrates experimental energies relative to the rotating liquid drop (rld) energy, where the bands are labelled according to Fig. 4.1. The middle panel shows the selected calculated bands. The bottom panel shows the energy difference between the predictions and the observations. Signature α= 0 is represented by filled symbols, and α = 1 by open symbols.

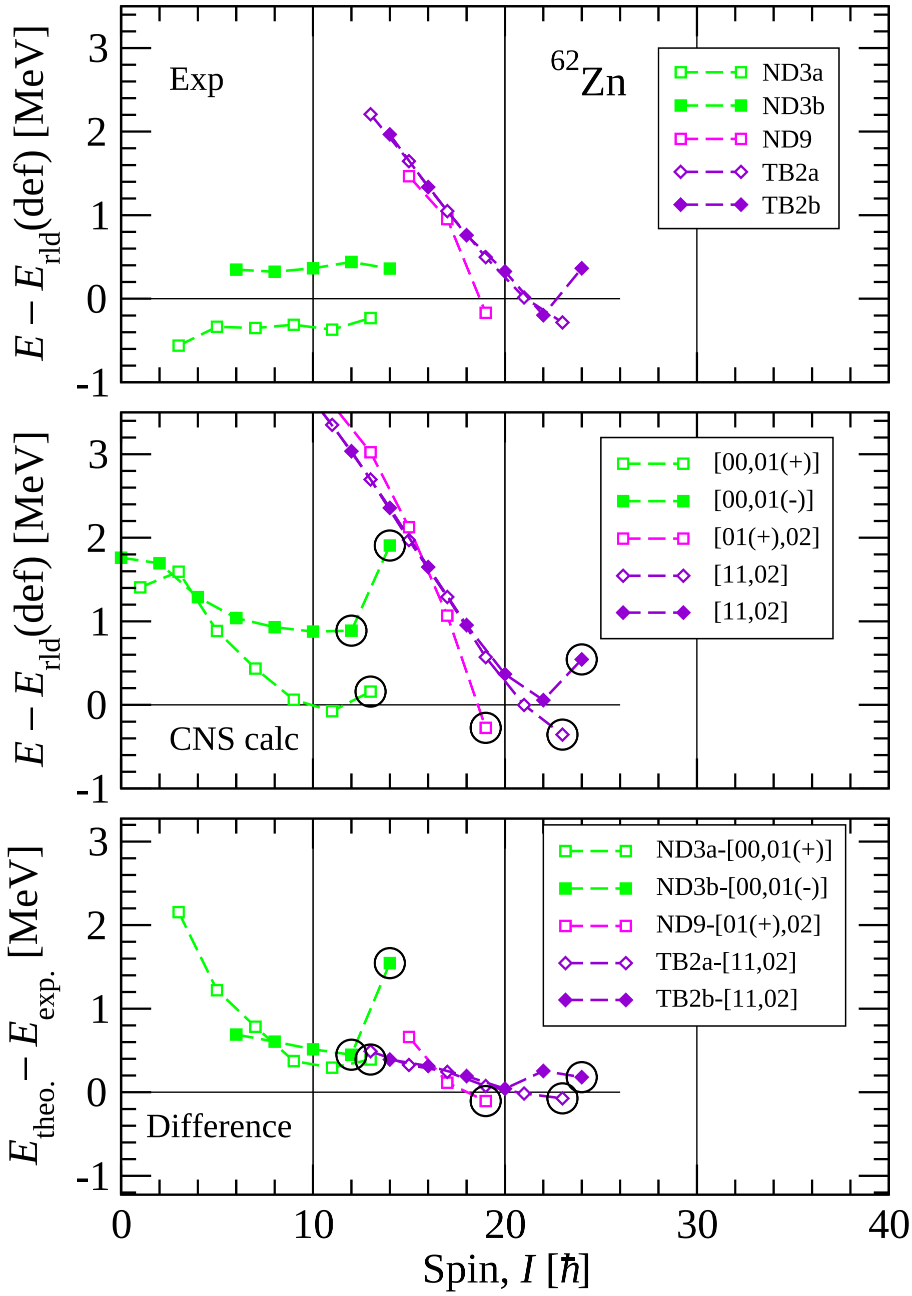

Figure 5.11: Same as Fig. 5.10 but here illustrated for observed bands with negative parity.

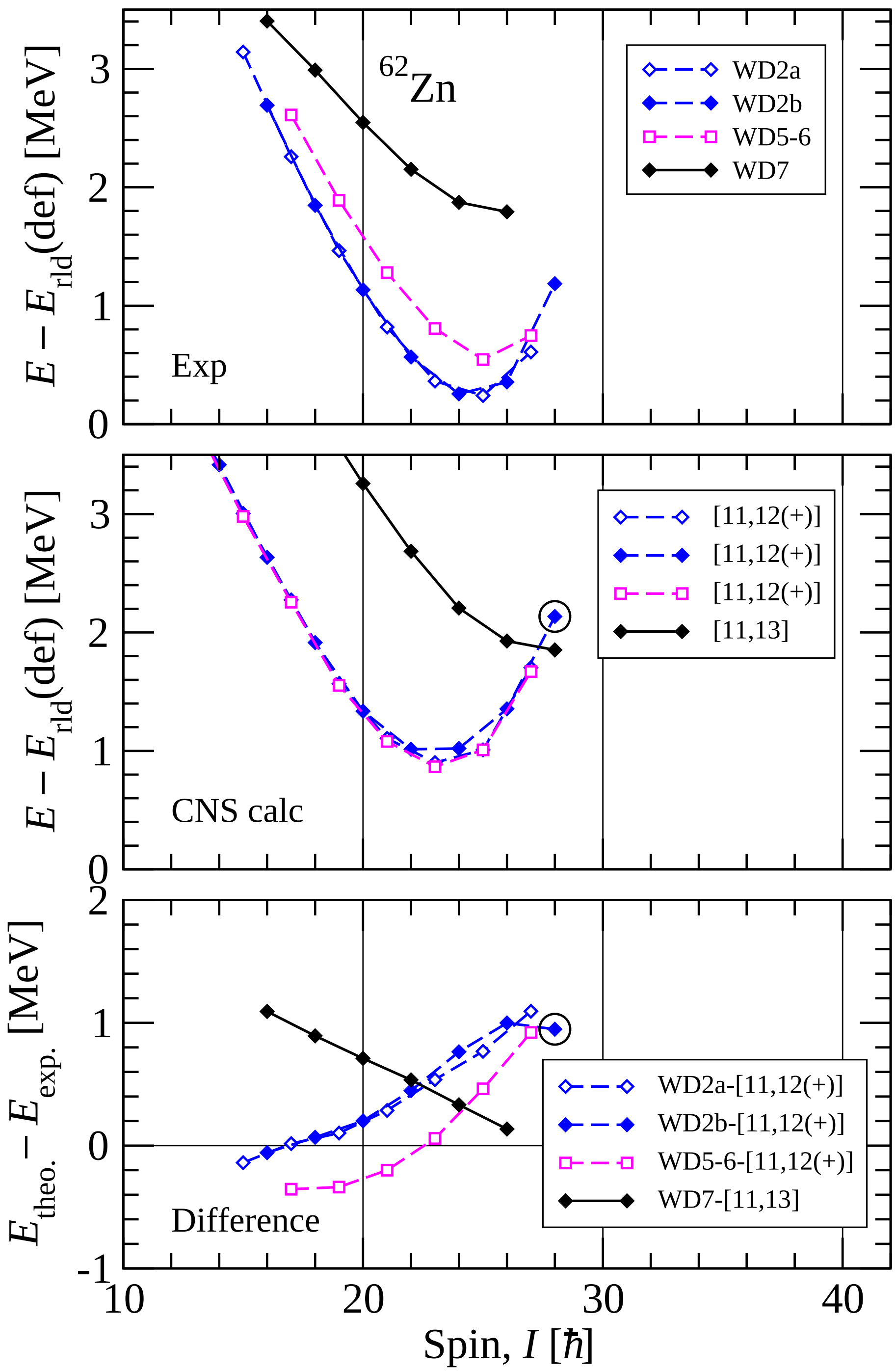

Figure 5.12: Same as Fig. 5.10 but with the assigned configurations of one proton and one nutron hole in the $1f_{7/2}$ shell for both positive and negative parity high-spin deformed structures with maximum spin $\leq 30\hbar$ with firm spin-parity assignments. Solid (dashed) lines represent positive (negative) parity.

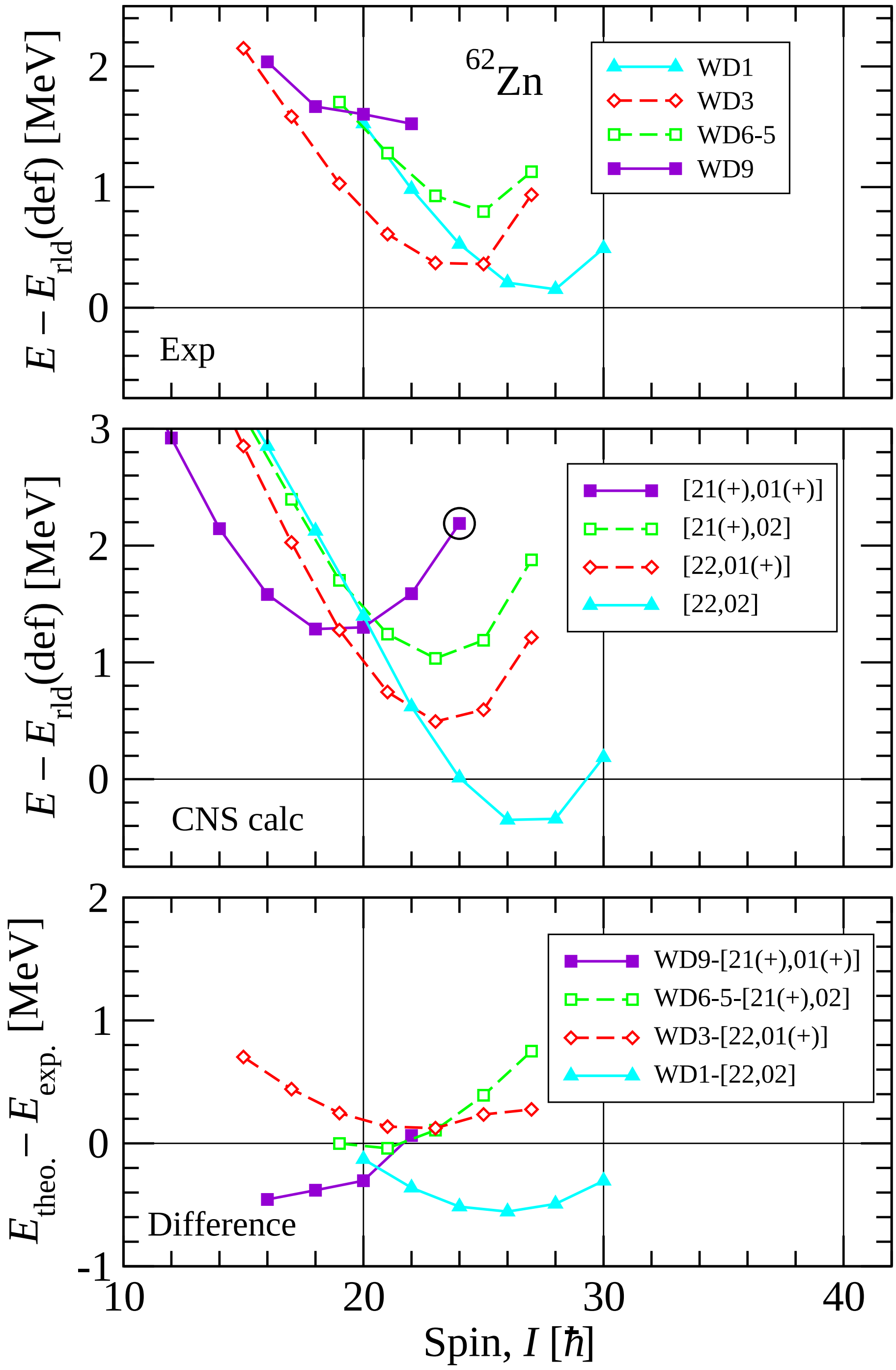

Figure 5.13: Same as Fig.5.12 but here shown for bands with two proton holes in the $1f_{7/2}$ shell.

and WD6. Experimentally these two bands come close together at spin $I^{\pi} = 21^{-}$ with in an energy difference of 20 keV. To make these band energies smooth, WD5 and WD6 bands should cross at the 21^{-} spin state. In this process, two smooth undisturbed bands with new energies called WD5-6 and WD6-5 are formed. The WD5-6 band is assigned to $[11, 12(+)]$ and the WD6-5 band is assigned to $[21(+), 02]$.

With one neutron hole and one proton hole in $1f_{7/2}$, two pairs of signature partner bands are obtained which are degenerate in a large spin range. The WD2a and WD2b bands can be assigned to the $[11, 12(+)]$ bands with $I_{max} = 27^{-}, 28^{-}$, while the WD5-6 band can be assigned to the other odd-spin $[11, 12(+)]$ configuration. There will be an interaction between the $[11, 12(+)]$ configurations with the same signature which is not included in the CNS formalism. This interaction would lead to a splitting in general agreement with what is seen for the observed WD2a and WD5-6 bands. The WD7 band can be assigned to the [11,13] band, which is lowest in energy at high spin, [see Fig. 5.7, panel (a)]. The energy differences between experimental and calculated, for all these bands are within ± 1 MeV, in the lower panel of Fig. 5.12 and 5.13, but the different slopes are somewhat problematic.

The spin and parity assignments are uncertain experimentally for the structures WD8 and WD10. Therefore, it is difficult to assign configurations to them.

Figure 5.14 is analogous to Fig. 5.12 but for superdeformed band structures with firm spin-parity assignments. The bands SD1 and SD2 are in good agreement with the $[22, 23(-)]$ and $[22, 23(+)]$ signature partner configurations. SD3 fits with the [22,24] configuration, but it is then strange that the [22,22] band is not observed. More details on these band assignments are reported in [1] [45].

The new SD4 band spin is uncertain and the parity is undetermined. However, there are some possible configuration assignments. It is clearly seen from Fig. 5.9 that the calculated π[22] bands with one or two neutron holes in the $1f_{7/2}$ shell have a smaller slope, while the bands with one particle in $1h_{11/2}$ have a larger slope compared to the experimentally observed SD4 band in Fig. 5.13 top panel. The calculated bands with three proton holes in the $1f_{7/2}$ shell and three protons in the $1g_{9/2}$ shell have a better slope than these two cases discussed above. The corresponding $[33, 23(-)]$ band is compared with the observed SD4 band, resulting in ~ 1.4 MeV energy difference in the lower panel of Fig. 5.14. In conclusion the configuration of SD4 is unclear. The new SD5 band might be assigned to the negative signature partner of [22,13] configuration.

5.4.2 Deformations

The calculated shape trajectories for the selection of bands, assigned to TB1b, TB2a, WD2b, WD3, WD1 and SD1, are illustrated in Fig. 5.15. It can be seen that the bands in general change their shapes gradually, starting close to $\gamma = 0°$ (prolate) and approaching $\gamma = 60°$ (oblate) at termination.

It was shown in [15] that the number of particles excited into $1g_{9/2}$, together with the number of particle-hole excitations across the $N = Z = 28$ shell gap, is strongly correlated to the calculated deformation at a low or intermediate spin value. The trend is seen in Fig. 5.15, which includes structures ranging from two particles in $1g_{9/2}$ subshell, $[11, 01(+)]$, to five particles, $[22, 23(-)]$. Simultaneously the number of particle-hole excitations from the

[1] There is a small error in the moment of inertia calculation in [45] which affects both the calculated energies and the reference energies which are subtracted. This leads to differences of a few hundred keV in the energies of the $E - E_{rld}$ plots, but it does not change any conclusions about configuration assignments.

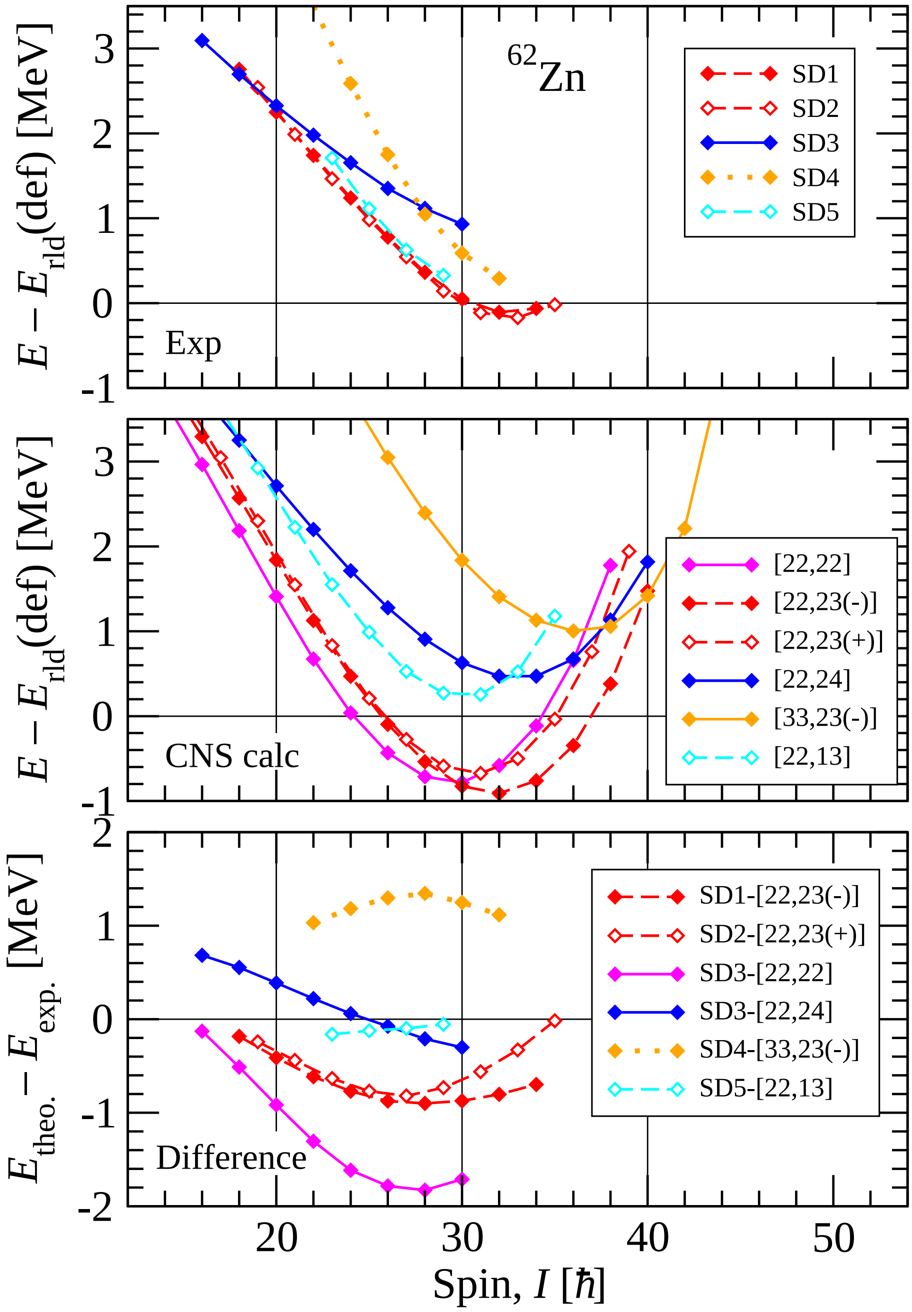

Figure 5.14: Same as Fig. 5.12 but here shown for superdeformed band structures with $I_{max} \lesssim 35\hbar$.

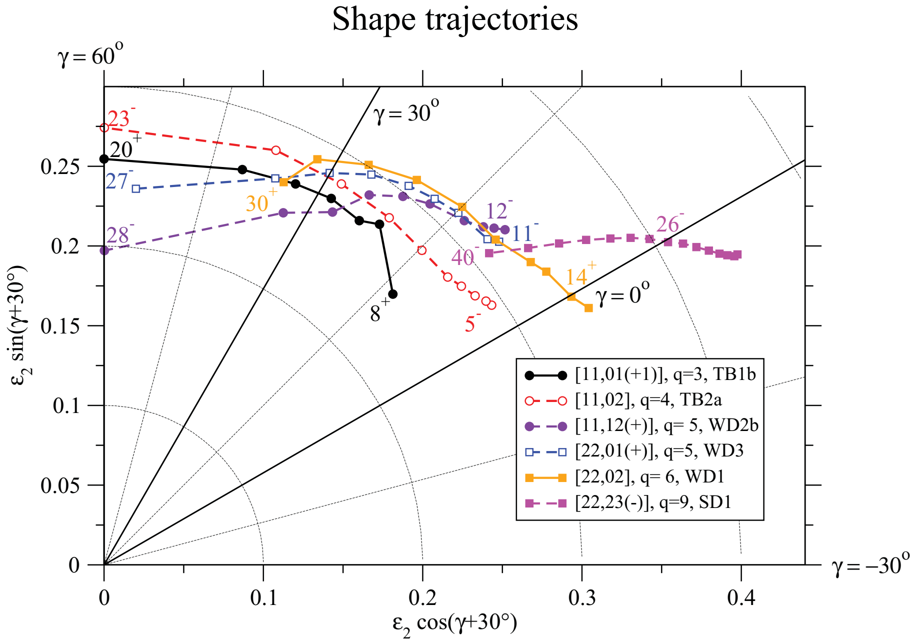

Figure 5.15: The calculated shape evolution of selected configurations assigned to the bands TB1b, TB2a, WD2b, WD3, WD1 and SD1 in the (ε_2, γ) plane. The $\gamma = 0°$ axis describes prolate shape with collective rotation and $\gamma = 60°$ oblate shape with rotation around the symmetry axis. Intermediate values of γ, i.e., $0° < \gamma < 60°$ signify triaxial shapes.

$1f_{7/2}$ subshell ranges from one to four. To see the combined effect, the variable q was introduced [15] as the sum of particle-hole excitations and particles in $g_{9/2}$ subshell according to $q = p_1 + p_2 + n_1 + n_2$. In the figure the illustrated structures range from $q = 3$ up to $q = 9$, and the average deformation increases with q as suggested earlier.

Chapter 6

Conclusions and Outlook

The combined data from four different fusion-evaporation reaction experiments has been used to construct and analyse the excitation scheme of the nucleus ^{62}Zn. The resulting level scheme comprises some 250 energy levels and 430 γ-ray transitions. The proposed maximum spin is $I = 35\,\hbar$ at an excitation energy of $E_x = 42.5$ MeV; numbers comparable only to ^{58}Ni [31]. One important result is that the configuration assignment puzzle has been solved for the first superdeformed band observed in $A \sim 60$ region [8, 45] .

Apart from the previous results [8, 20], the present results include a number of low-spin, normally deformed structures, ten new well-deformed rotational bands, and four additional superdeformed bands. These are summarized and presented in the three publications of this licentiate thesis. The combination of the GAMMASPHERE γ-ray spectrometer and ancillary particle detection systems allowed for the connection of rotational bands to well-known, low-lying excited states in ^{62}Zn. The present results pave the way towards a complete assessment of superdeformation in the $A \sim 60$ region.

The experimental characteristics of the rotational bands are analyzed and compared with results from Cranked Nilsson-Strutinsky calculations. Most of the structures are characterized by means of these calculations, where it is concluded that the low-spin normal deformed structures have no holes in the $1f_{7/2}$ orbitals, the two known terminating bands have one hole, the well-deformed bands have two holes and finally the superdeformed bands have three to four holes in the $1f_{7/2}$ orbitals. With more particles in the high-j $1g_{9/2}$ orbitals the terminating sequences become more down-sloping, when drawn relative to the rotating liquid drop reference, i.e., they are more favoured in energy at high-spin states. More holes in the high-j $1f_{7/2}$ orbitals on the other hand lead to terminating sequences with a large curvature, corresponding to small moments of interia.

The present analysis, combined with available experimental results in the $A \sim 60$ mass region, will be used to improve the current set of Nilsson parameters in the $N = 3$ and $N = 4$ oscillator shells.

Acknowledgments

With great pleasure, I take this opportunity to put my gratitude to all those who have contributed towards this thesis in various ways.

It is difficult to overstate my gratitude to my supervisor, Professor Dirk Rudolph, without whom this thesis would not have been possible. I have been very fortunate to have the privilege of working with him. Enlightening discussions, many hours spent in front of the computer, and great deal of effort put in reading this thesis are only few of the many things I am obliged for.

I also would like to thank my co-supervisor Professor Ingemar Ragnarsson for giving me the opportunity to contact the Lund Nuclear structure Group and for teaching me about CNS calculations as well as the all the things regarding physics. I feel very grateful to you both for always showing interest in my work, for your continuous encouragement and especially for correcting my thesis. I would also like to thank my other co-supervisor Professor Claes Fahlander for his support on this thesis.

It is a pleasure to thank all my friends, especially Douglas DiJulio and Ulrika Forsberg for their help. I am also thankful to the rest of the people working in and together with the Nuclear Structure Group in Lund. A special thanks goes to Lise-Lotte Andersson for her quick answers through mail.

Finally, I would like to convey my sincere gratitude to my husband, my little daughter and my family members for always standing by me, it means more to me than I could ever express.

Bibliography

[1] A.V. Afanasjev, D.B. Fossan, G.J. Lane, and I. Ragnarsson, Phys. Rep. **322**, 1 (1999).

[2] http://www.aip.org/png/html/shapes.htm .

[3] T. Troudet and R. Arvieu, Phys. Lett. **B82**, 308 (1979).

[4] I. Ragnarsson, Phys. Lett. **B199**, 317 (1987).

[5] S.M. Polikanov *et al.*, Sov. Phys. JETP **15**, 1016 (1962).

[6] C. Andreoiu, PhD thesis, Lund University, ISBN 91-628-5308-2 (KFS AB, Lund, 2002).

[7] C.E. Svensson *et al.*, Phys. Rev. Lett. **85**, 2693 (2000).

[8] C.E. Svensson *et al.*, Phys. Rev. Lett. **79**, 1233 (1997).

[9] C. Baktash *et al.*, Phys. Rev. Lett. **74**, 1946 (1995).

[10] A.V. Afanasjev and I. Ragnarsson, Nucl. Phys. **A628**, 580 (1998).

[11] P.J. Nolan *et al.*, J. Phys. G **11**, L17 (1985).

[12] P.O. Tjom *et al.*, Phys. Rev. Lett. **55**, 2405 (1985).

[13] E.F. Moore *et al.*, Phys. Rev. Lett. **63**, 360 (1989).

[14] E.K. Johansson *et al.*, Phys. Rev. C **80**, 014321 (2009).

[15] C. Andreoiu *et al.*, Eur. Phys. J. **A14**, 317 (2002).

[16] L.L. Andersson *et al.*, Eur. Phys. J. **A36**, 251 (2008).

[17] L.L. Andersson *et al.*, Phys. Rev. C **79**, 024312 (2009).

[18] J. Gellanki *et al.*, to be published.

[19] C.E. Svensson *et al.*, Phys. Rev. Lett. **82**, 3400 (1999).

[20] C.E. Svensson *et al.*, Phys. Rev. Lett. **80**, 2558 (1998).

[21] I. Ragnarsson *et al.*, Phys. Rev. Lett **74**, 3935 (1995).

[22] http://nucalf.physics.fsu.edu/ ∼riley/gamma/.

[23] G.F. Knoll, "Radiation and Measurement", 2nd edition, John Wiley & Sons, New York (1989).

[24] I.-Y. Lee, Nucl. Phys. **A520**, 641c (1990).

[25] EUROBALL III, A European γ-ray facility, Eds. J. Gerl and R.M. Lieder, GSI 1992.

[26] http:// axpd30.pd.infn.it/GASP/.

[27] D.G. Sarantites *et al.*, Nucl. Instrum. Meth. **A381**, 418 (1996).

[28] http://wunmr.wustl.edu/ ~dgs/mball/.

[29] D. Rudolph *et al.*, Phys. Rev. Lett. **89**, 022501(2002).

[30] D.A.Torres *et al.*, Phys. Rev. C **78**, 054318 (2008).

[31] D. Rudolph *et al.*, Phys. Rev. Lett. **96**, 092501 (2006).

[32] M. Devlin *et al.*, Nucl. Instrum. Meth. **A383**, 506 (1996).

[33] C.E. Svensson *et al.*, Nucl. Instrum. Meth. **A396**, 288 (1997).

[34] D. C. Radford, Nucl. Instrum. Meth. **A361**, 297 (1995).

[35] J. Theuerkauf, S. Esser, S. Krink, M. Luig, N. Nicolay, O. Stuch, H. Wolters, Program Tv, University of Cologne, unpublished.

[36] D. Seweryniak *et al.*, Nucl. Instrum. Meth. **A340**, 353 (1994).

[37] B. Cederwall *et al.*, Nucl. Instrum. Meth. **A354**, 591 (1995).

[38] K.S. Krane, R.M. Steffen, and R.M.Wheeler, At. Data Nucl. Data Tables **11**, 351 (1973).

[39] H.J. Rose and D. Brink, Rev. Mod. Phys. **39**, 306 (1967).

[40] D. Rudolph *et al.*, Eur. Phys. J. **A4**, 115 (1999).

[41] J.F. Bruandet, Tsan Ung Chan, M. Agard, J.P. Longequeue, C. Morand, and A. Giorni, Z. Phys. **A 279**, 69 (1976).

[42] L. Mulligan, R. W. Zurmuhle, D. P. Balamuth, Phys. Rev. C **19**, 1295 (1979).

[43] N.J. Ward, L.P. Ekström, G.D. Jones, F. Kearns, T.P. Morrison, O.M. Mustaffa, D.N. Simister, P.J. Twin, and R. Wadsworth, J. Phys. G **7**, 815 (1981).

[44] K. Furutaka *et al.*, Z. Phys. **A 358**, 279 (1997).

[45] J. Gellanki *et al.*, Phys. Rev. C **80**, 051304(R) (2009).

[46] I. Ragnarsson, Z. Xing, T. Bengstsson, and M. A. Riley, Phys. Scr. **34**, 651 (1986).

[47] S.G. Nilsson, Dan. Mat. Fys. Medd. **29**, no. 16 (1955).

[48] S. G. Nilsson, I. Ragnarsson, Shapes and Shells in Nuclear Structure (Cambridge University Press, 1995).

[49] S. G. Nilsson *et al.*, Nucl. Phys. **A131**, 1 (1969).

[50] O. Haxel, J.H.D. Jensen, and H.E. Suess, Phys. Rev. **75**, 1766 (1949).

[51] M.G. Mayer, Phys. Rev. **75**, 1969 (1949).

[52] C. Gustafsson, I.L. Lamm, B. Nilsson and S.G. Nilsson, Ark. Fys. **36**, 613 (1967).

[53] D.R. Inglis, Phys. Rev. C **96**, 1059 (1954).

[54] D.R. Inglis, Phys. Rev. C **103**, 1786 (1956).

[55] T. Bengtsson and I. Ragnarsson, Nucl. Phys. **A436**, 14 (1985).

[56] B.G. Carlsson and I. Ragnarsson, Phys. Rev. C **74**, 011302(R) (2006).

[57] S.E. Larsson, Phys. Scr. **8**, 17 (1973).

[58] V.G. Zelevinskii *et al.*, J. Nucl. Phys. **22**, 565 (1975).

[59] K. Pomorski and J. Dudek, Phys. Rev. C **67**, 044316 (2003).

[60] V.M. Strutinsky, Nucl. Phys. **A95**, 420 (1967).

[61] G. Andersson *et al.*, Nucl. Phys. **A268**, 205 (1976).

PAPER I

PHYSICAL REVIEW C **80**, 051304(R) (2009)

Characterization of superdeformed bands in ^{62}Zn

J. Gellanki,[1,*] I. Ragnarsson,[2] D. Rudolph,[1] C. E. Svensson,[3] L.-L. Andersson,[1,†] C. Andreoiu,[1,3,‡] C. Baktash,[4] M. P. Carpenter,[5] R. J. Charity,[6] C. J. Chiara,[6,§] J. Eberth,[7] J. Ekman,[1,∥] C. Fahlander,[1] D. S. Haslip,[3] E. K. Johansson,[1] D. R. LaFosse,[6,¶] S. D. Paul,[4] O. L. Pechenaya,[6,**] W. Reviol,[6] R. du Rietz,[1,††] D. G. Sarantites,[6] D. Seweryniak,[5] L. G. Sobotka,[6] H. G. Thomas,[7] D. A. Torres,[1,8,‡‡] J. C. Waddington,[3] J. N. Wilson,[6,§§] C. H. Yu,[4] and S. Zhu[5]

[1]*Department of Physics, Lund University, S-22100 Lund, Sweden*
[2]*Division of Mathematical Physics, LTH, Lund University, S-22100 Lund, Sweden*
[3]*Department of Physics, University of Guelph, Guelph, Ontario N1G 2W1, Canada*
[4]*Physics Division, Oak Ridge National Laboratory, Oak Ridge, Tennessee 37831, USA*
[5]*Physics Division, Argonne National Laboratory, Argonne, Illinois 60439, USA*
[6]*Chemistry Department, Washington University, St. Louis, Missouri 63130, USA*
[7]*Institut für Kernphysik, Universität zu Köln, D-50937 Köln, Germany*
[8]*Departamento de Física, Universidad Nacional de Colombia, Bogotá, Colombia*

(Received 18 September 2009; published 24 November 2009)

Combined data from four fusion-evaporation reaction experiments were utilized to investigate deformed and superdeformed structures in $^{62}_{30}$Zn$_{32}$. Combination of the Gammasphere γ-ray spectrometer and ancillary particle detection systems allowed for the connection of rotational bands to well-known, low-lying excited states in ^{62}Zn, as well as spectroscopy of discrete high-spin states reaching excitation energies of $E_x = 42.5$ MeV. Four well- or superdeformed bands in ^{62}Zn are characterized and described by means of cranked Nilsson-Strutinsky calculations.

DOI: 10.1103/PhysRevC.80.051304 PACS number(s): 21.60.Cs, 23.20.En, 23.20.Lv, 27.50.+e

The existence of nuclear rotational excitations relates directly to the possible nonisotropic mass distribution of the nucleus. Indeed, some nuclei are found to have a stable axial deformation with a major-to-minor axis ratio approaching 2 : 1. Nuclei at this extraordinary deformation are referred to as "superdeformed" (SD), and more than 250 SD bands have been observed in the mass regions $A \sim 190$, 150, 130, 80, 60, and 40 [1]. Building on two-particle, two-hole (2p-2h) excitations for both protons and neutrons across the magic gap at particle numbers $Z = N = 28$, large SD shell gaps at single-particle energy levels for the particle numbers $N, Z \sim 30$–32 were predicted in the $A \sim 60$ mass region long ago [2,3]. In the intermediate spin and energy range, these SD bands often compete with well-deformed (WD) terminating bands, which have a smaller number of cross-shell excitations.

Following the first observation of an SD band in ^{62}Zn [4], SD bands and, likewise, WD bands have been observed in a number of nuclei in the $A \sim 60$ region, namely, ^{57}Co [5], $^{56,58-60}$Ni [6–11], ^{58,59,61}Cu [12–16], and $^{60-62}$Zn [17–20]. Despite significant experimental information on ^{62}Zn, the properties of the SD band in ^{62}Zn remain unclear [4,21]. The decay-out transitions of the SD band could not be established [4], which was taken to signify a different decay-out process compared to ^{60,61}Zn [17,18]. The additional neutrons outside the $N = 30$ shell gap may affect both pair correlations and the barrier between the SD well and the first, near-spherical potential well. In this study, we were able to classify the known and three new rotational bands in ^{62}Zn.

The results originate from the combined statistics of four experiments carried out at Argonne and Lawrence Berkeley National Laboratory. For a thorough description of the experimental details, see, for example, Refs. [9,11,14,19]. In brief, one experiment used the fusion-evaporation reaction ^{40}Ca(^{28}Si,1α2p)^{62}Zn at a beam energy of 122 MeV. The target with 99.975% isotopic enrichment was 0.5 mg/cm^2 thick. ^{62}Zn nuclei were populated with ≈30% of the total fusion-evaporation cross section. The experimental setup consisted of the Gammasphere array [22], at that time comprising 103 Ge detectors, for γ-ray detection. The array was operated in conjunction with the 4π charged-particle detector array Microball [23]. The Heavimet collimators were removed from the Ge detectors to provide γ-ray multiplicity and sum-energy measurements [24] and additional channel selectivity by total energy conservation requirements [25]. `Data set 1` represents the basis of our study, namely, to identify the SD bands and the decay-out transitions from the SD bands into states in the first minimum of the potential. In

*gellanki.jnaneswari@nuclear.lu.se
†Present address: Department of Physics, University of Liverpool, Liverpool L69 7ZE, United Kingdom.
‡Present address: Chemistry Department, Simon Fraser University, Burnaby, British Columbia V5A 1S6, Canada.
§Present address: Nuclear Engineering Division, Argonne National Laboratory, Argonne, Ilinois 60439, USA.
∥Present address: Malmö högskola, S-20506 Malmö, Sweden.
¶Present address: Teradyne Inc., North Reading, Massachusetts 01864, USA.
**Present address: Department of Radiation Oncology, Washington University School of Medicine, St. Louis, Missouri 63130, USA.
††Present address: Department of Nuclear Physics, The Australian National University, Canberra, ACT 0200, Australia.
‡‡Present address: University of the West of Scotland, High Street, Paisley PA1 2BE, Scotland, United Kingdom.
§§Present address: IPN Orsay, F-91406 Orsay, France.

 ©2009 The American Physical Society

addition, three more experiments using the fusion-evaporation reaction ^{28}Si(^{36}Ar,2p)^{62}Zn at beam energies of about 140 MeV were performed [9,11,19]. Whereas the relative yield for ^{62}Zn is very small, this combined `data set 2` adds to the addition of the highest-spin states of the bands.

The analysis was restricted to events in which all of the evaporated charged particles, that is, two protons in the case of `data set 2` and an additional α particle for `data set 1`, were detected. A kinematic Doppler-shift correction of the γ-ray energies is possible, based on the measured charged-particle energies and directions, which define the momenta of the recoiling residual nuclei for each event. In addition, the γ rays originating from the SD bands are likely to be emitted while the residual ^{62}Zn nuclei are still slowing down inside the thin target foil. Assuming average deformation of the rotational bands in ^{62}Zn and simulating the slowing-down process in the thin target layer, so-called additional fractional Doppler shifts can be derived as a function of γ-ray energy [26]. Taking this into account, a more accurate Doppler-shift correction of the γ rays originating from deformed structures is obtained.

Our study of ^{62}Zn relies on a $\gamma\gamma\gamma$ cube of `data set 1` analyzed with the RADWARE package [27]. To confirm low-intensity or ambiguous transitions, certain parts of the decay scheme are focused on during the analysis by specific $\gamma\gamma$ matrices, which are preselected by γ rays originating from a certain rotational band or decay sequence within the complex ^{62}Zn excitation scheme. For `data set 2`, a $\gamma\gamma$ matrix was created, which focuses on the high-lying entry states in ^{62}Zn by requiring at least 14 detected γ rays with at least 16.5-MeV total energy and less than 19-MeV particle energy [8]. For γ-ray spectrum analyses, the code TV developed at the University of Cologne [28] was used. The assignment of $E1$, $M1$, $E2$, or mixed $E2/M1$ multipolarities to γ-ray transitions is based on directional correlations from oriented states defined as the ratio of yields, Y:

$$R_{\mathrm{DCO}} = \frac{Y(\gamma_1 \text{ at } 30^\circ;\ \text{gated with } \gamma_2 \text{ at } 83^\circ)}{Y(\gamma_1 \text{ at } 83^\circ;\ \text{gated with } \gamma_2 \text{ at } 30^\circ)}.$$

Using known stretched $E2$ transitions as γ_2, $R_{\mathrm{DCO}} \sim 1.0\ (0.6)$ is expected for observed quadrupole (dipole) transitions γ_1. For more details, we refer to, for example, Refs. [14] and [16].

The primary result of the coincidence analysis is the high-spin excitation scheme of ^{62}Zn shown in Fig. 1. Four bands, labeled SD1, SD2, SD3, and WD1, are observed, whereas only the most relevant transitions in the complex low-lying decay scheme of ^{62}Zn are included [4,20,29]. All four bands are connected to the low-spin states by several linking transitions. This allows spin and parity assignments to the lowest states in the bands, because the transitions at the bottom of the bands are either sufficiently intense or sufficiently clean to distinguish between stretched quadrupole and dipole characters of some of the more intense linking transitions. Assuming an $E2$ character of the in-band transitions, the tentative spin and parity assignments to the states near the top of the bands are based on their regular rotational behavior.

The known band SD1, which was observed up to the 3234-keV transition [4], was extended by transitions at 3579, 3958, and 4234 keV. These topmost transitions are observed only in `data set 2`: the spectrum in Fig. 2(b) was obtained by summing γ-ray spectra in coincidence with several SD1 band members in the corresponding two-proton selected $\gamma\gamma$ matrix. Whereas both the 3958- and the 4234-keV transitions are found to be in coincidence with the line at 3579 keV, a mutual coincidence between them cannot be firmly established. Thus the 4234-keV line is not included in Fig. 1, as it feeds either the 36496- or the 40454-keV level of SD1.

Figure 2(a) shows results for SD1 from the high-statistics `data set 1`. SD1 is connected to the low-spin part of the level scheme via a total of six γ-ray transitions. Interestingly, all of them feed “band 2” of Ref. [20], and some of them are labeled in Fig. 2(a), at 2963, 3027, and 3983 keV. These are clearly visible, even though their relative yield is only ~0.1% of the 954-keV ground-state transition. Low-lying SD1 band members are about a factor of 10 more “intense,” consistent

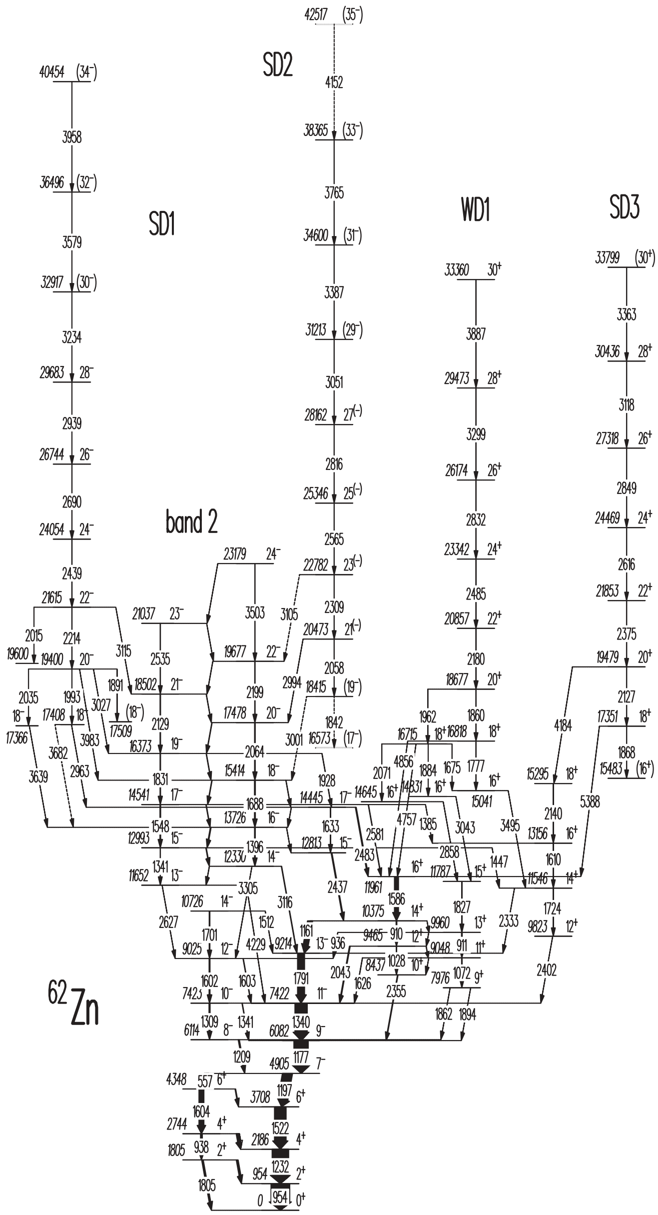

FIG. 1. Partial decay scheme of ^{62}Zn. Energy values are given as kilo-electron volts, and the widths of the arrows correspond to the relative intensities of the γ rays.

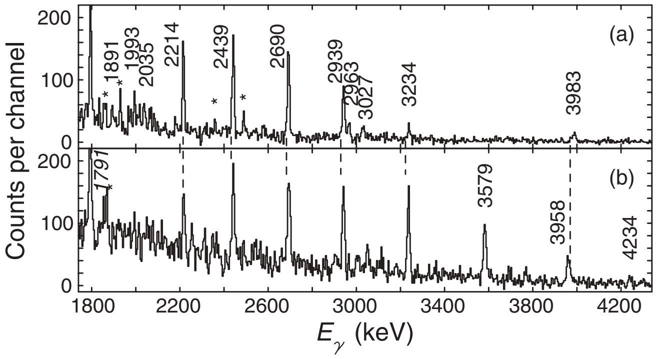

FIG. 2. (a) γ-ray spectrum in coincidence with any combination of two of the 1993-, 2214-, 2439-, 2690-, 2939-, and 3234-keV transitions of SD1 taken from `data set 1`. (b) γ-ray spectrum generated from `data set 2` by coincidence requirements on the 2214-, 2439-, 2690-, 2939-, 3234-, and 3579-keV transitions in SD1. γ-ray labels are kilo-electron volts, the binning is 4 keV per channel, and an asterisk or italic labeling indicates lines from the lower part of the ^{62}Zn decay scheme in Fig. 1.

with Ref. [4]. Despite this very low yield, a careful analysis provides $R_{\mathrm{DCO}} = 0.59(24)$ and $R_{\mathrm{DCO}} = 1.12(36)$ for the 2963- and 3983-keV lines, respectively. In conjunction with the $E2$ character of the in-band transitions, these numbers provide the $I^{\pi} = 20^{-}$ assignment of the 19400-keV level. Thus, the maximum observed spin of SD1 is $I^{\pi} = (34^{-})$ at an excitation energy of $E_x = 40.7$ MeV. Note that the high statistics allow for observation of the beginning of several decay-out branches near the bottom of SD1, for example, the yield of the 1891-, 1993-, and 2035-keV transitions accounting essentially for that of the 2214-keV line.

Excitation energies and rotational frequencies of SD1 and the bands in ^{58}Ni [8] are surpassed by SD2, which is shown in Fig. 3(a). Like SD1, the three topmost transitions, at 3387, 3765, and 4152 keV, are seen only in `data set 2`. The transitions linking SD2 into “band 2” [4] are established at 2994 keV and, tentatively, 3001 and 3105 keV. In addition, the DCO ratio of the doublet at 2994/3001 keV amounts to $R_{\mathrm{DCO}} = 0.61(20)$, that is, dipole character. The parity assignment for SD2 remains tentative, as it is impossible to distinguish electric or magnetic dipole character with the present data.

Figure 3(b) illustrates WD1 as obtained from `data set 1`. The inset shows the high-energy part of the spectrum. Once more the topmost transition at 3887 keV is only observed in `data set 2`. With an intensity of about 2% relative to the 954-keV ground-state transition, WD1 is presently the most intense high-spin band in ^{62}Zn. The band is connected to low-spin states via several linking paths including transitions at 1827, 1884, 2858, 3043, 3495, 4757, and 4856 keV. Among these, the 3043- to 1827-keV cascade (dipole-quadrupole) and the 3495-keV direct link (quadrupole) are intense enough to deduce DCO ratios [29]. Thus, positive parity can be assigned to WD1.

A spectrum in coincidence with the 5388-keV decay-out transition of SD3 and one of the band members of SD3 is shown in Fig. 3(c). It provides the extremely high quality of `data set 1`: With relative yields as low as 0.02% (5388-keV line) and less than 0.8% (band members), the triple

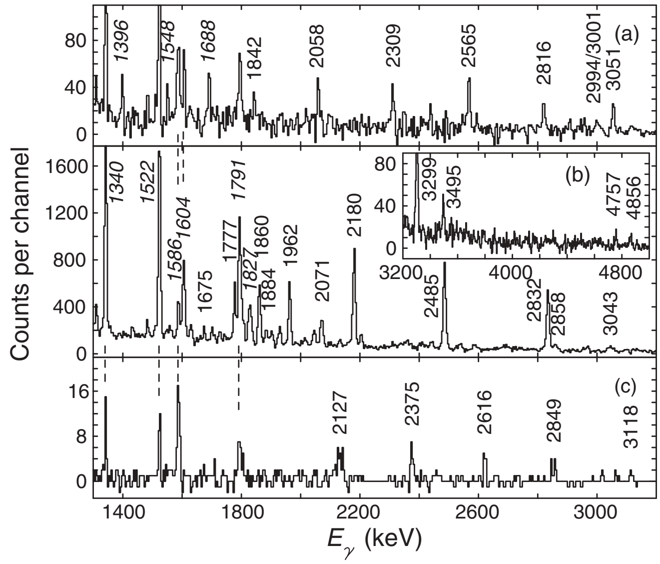

FIG. 3. A sample of γ-ray spectra taken from `data set 1`. (a) Spectrum in coincidence with any combination of the 2309-, 2565-, and 2816-keV and the 1842-, 2058-, 2309-, 2565-, 2816-, and 3051-keV transitions of SD2. (b) Spectrum in coincidence with any combination of the 2180-, 2485-, 2832-, and 3299-keV and the 1860-, 1962-, 2180-, 2485-, 2832-, and 3299-keV transitions of WD1. (c) Spectrum in coincidence with the 5388-keV decay-out transition and any of the 2375-, 2616-, 2849-, and 3118-keV transitions of SD3. See text and caption to Fig. 2 for more details.

coincidences both with members of SD3 (2127, 2375, 2616, 2849, and 3118 keV) and with the relevant transitions in the low-spin regime (here 1340, 1522, 1586, and 1791 keV) are clearly visible. The DCO ratio for the 5388-keV linking transition is found to be consistent with $E2$ character [$R_{\mathrm{DCO}} = 1.15(34)$], that is, the maximum spin of this band is $I^{\pi} = (30^{+})$ at $E_x = 33.8$ MeV.

Observed bands were analyzed using the configuration-dependent cranked Nilsson-Strutinsky model [30–32]. In this model, one considers the rotation from the intrinsic frame of reference, in which nucleons experience an additional potential caused by the Coriolis and centrifugal forces. The total energy of fixed configurations is minimized in the deformation parameters ε_2, γ, and ε_4 at each spin. Standard parameters [30] were used in the Nilsson Hamiltonian. At high spin, pairing is of little importance and thus neglected.

Configurations assigned to the observed SD bands in ^{62}Zn are illustrated schematically in Fig. 4. The most important orbitals include the $\mathcal{N} = 3$ high-j shell $1f_{7/2}$ and upper fp-shell orbitals $1f_{5/2}$, $2p_{3/2}$, and $2p_{1/2}$ and, finally, the $\mathcal{N} = 4$ orbit $1g_{9/2}$. In the deformed rotating potential these j shells mix, that is, the wave functions of the single-particle orbitals will have amplitudes in several j shells. However, it turns out that for deformations up to $\varepsilon_2 = 0.3$–0.4, the orbitals can be classified as having their main amplitudes either in the high-j intruder shell or in the other shells with lower j values [31,33]. Thus, each configuration can be labeled $[p_1 p_2, n_1 n_2]$. Here, for protons and neutrons, respectively, p_1 and n_1 denote the number of holes in the high-j $1f_{7/2}$ orbitals, and p_2 and n_2 denote the number of particles in the high-j $1g_{9/2}$ subshell.

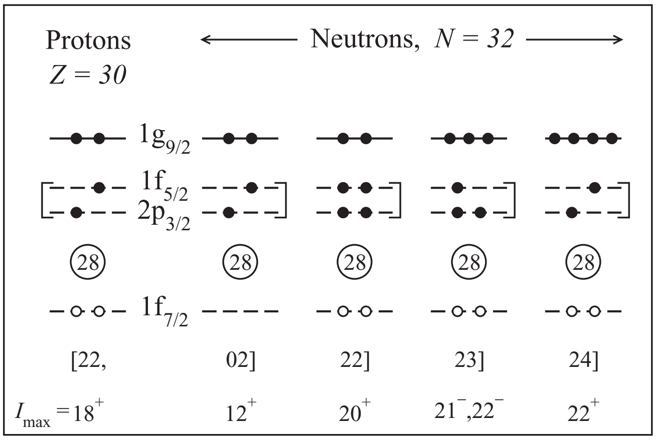

FIG. 4. Schematic illustration of configurations considered for interpretation of the observed SD bands in ^{62}Zn. Filled circles indicate particles and open circles indicate holes relative to the spherical $Z = N = 28$ gap. The $2p_{3/2}$ and $1f_{5/2}$ subshells are coupled to indicate that they mix strongly and are therefore treated as one entity in the configuration assignment. The $I_{\max}$ value given below each configuration is the maximum spin value that can be formed for the pure configuration according to the Pauli principle.

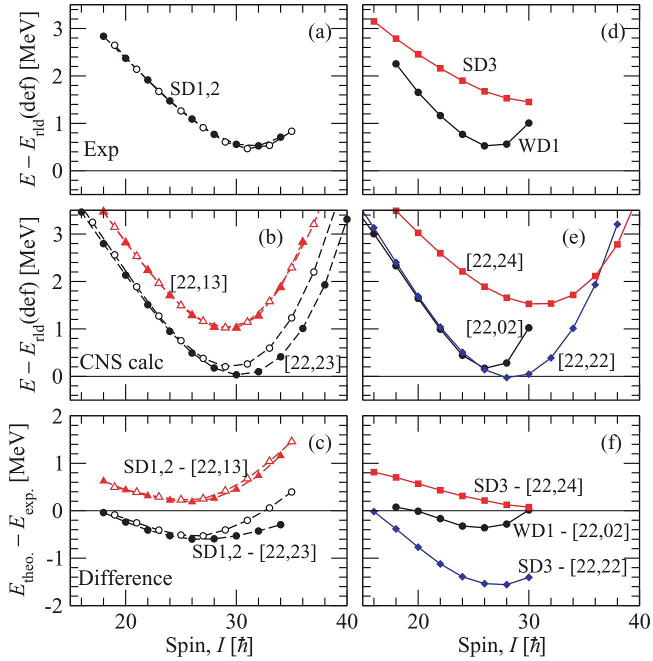

FIG. 5. (Color online) Comparison between experimentally observed structures and cranked Nilsson-Strutinsky predictions for rotational bands in ^{62}Zn, with the absolute energy scale fixed according to Ref. [32]. Top panels illustrate experimental energies relative to the rotating liquid drop (rld) energy, where the bands are labeled according to Fig. 1. Middle panels show the selected calculated bands. Bottom panels plot the energy difference between the predictions and the observations. Signature $\alpha = 0$ is represented by filled symbols; $\alpha = 1$, by open symbols. Solid (dashed) lines represent positive (negative) parity.

The valence configuration of ^{62}Zn corresponds to $\pi(2p_{3/2}1f_{5/2})^2\nu(2p_{3/2}1f_{5/2})^4$, namely, [00,00] in short-hand notation. Higher excitations for both 30 protons and 32 neutrons are obtained by lifting particles across the $Z = N = 28$ spherical shell gaps from the $1f_{7/2}$ subshell and/or exciting them to the $1g_{9/2}$ high-j shell. The combination of such proton and neutron excitations gives rise to the SD band configurations shown in Fig. 5. For example, in the case of protons, lifting the two particles from $1f_{7/2}$ into $1g_{9/2}$ yields the configuration $\pi(1f_{7/2})^{-2}(1f_{5/2}2p_{3/2})^2(1g_{9/2})^2$ with maximum spin, $I_{\max} = 18^+$, labeled "[22]." This proton configuration is greatly favored in a large region of the deformation space and relates to the doubly magic SD band in the $Z = N = 30$ nucleus $^{60}_{30}$Zn [17]. Above the corresponding neutron $N = 30$ SD gap, there are signature $\alpha = \pm 1/2$ pairs of low-j and high-j $\mathcal{N} = 3$ orbitals as well as high-j $\mathcal{N} = 4$ orbitals at similar energies. It becomes possible to form a rather large number of roughly equally favored configurations. The ones most likely to be assigned to the observed SD bands are shown in Fig. 4. Also note that because these low-j and high-j $\mathcal{N} = 3$ orbitals come at a similar energy, they mix rather strongly and special care must be taken to distinguish the different configurations [29].

In Fig. 5, the experimental bands are compared with the cranked Nilsson-Strutinsky predictions The energy difference between observed and calculated bands shown in the lower panels are expected to come within about ±1 MeV. If the observed transition energies are predicted correctly for the transitions within a band, the corresponding curve in the bottom panel will have a constant energy difference.

Bands SD1 and SD2 are signature partners with negative parity, which implies an odd number of $1g_{9/2}$ particles. This leaves [22,23] and [22,13] as possible assignments. The [22,23] configuration is clearly the most likely interpretation: it is calculated ∼1 MeV lower in energy and it appears impossible to get [22,13] below [22,23] with reasonable parameter changes. As shown in Fig. 5, the absolute energy of the [22,23] configuration is in good agreement with experiment, whereas the [22,13] configuration deviates too much at high spin. On the other hand, the two signatures are almost degenerate up to the highest spin values observed in experiment, which is in general agreement with the [22,13] but not with the [22,23] configuration. Therefore, we cannot totally exclude [22,13] as a possible assignment for SD1 and SD2. Both SD1 and SD2 decay-out primarily via "band 2," which has a [11,02] assignment [20]. Because band 2 falls in between the SD well and the near-spherical well, in terms of energy, spin, and deformation, a stepwise decay-out mechanism can be inferred for ^{62}Zn, similar to other $N \neq Z$ nuclei in the region [11,15,16,19].

WD1 is in good agreement with the [22,02] configuration. Though observed to its maximum spin value, it is still calculated to be slightly collective at $I = I_{\max}$, similar to bands discussed in Ref. [34]. The steep up slope when approaching $I = 30$ gives strong support for this assignment.

For SD3, configurations [22,22] or [22,24] are the most likely assignments. The general behavior of the curves in the lower panel in Fig. 5 is similar to that of the [22,22] assignment and the other observed bands. On the contrary, the absolute value of the difference is much larger than for the [22,24] assignment. However, with the [22,24] assignment, it

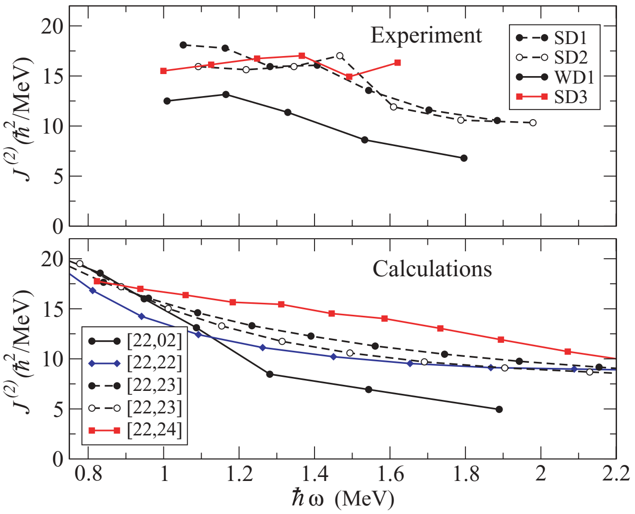

FIG. 6. (Color online) $J^{(2)}$ moments of inertia vs. rotational frequency for both observed and calculated rotational bands in ^{62}Zn.

is remarkable that the [22,22] band has not yet been observed, as it is calculated to be lower in energy.

The $J^{(2)}$ moments of inertia of the observed bands are shown in Fig. 6. Partly based on $J^{(2)}$ values, configuration [22,24] was assigned to SD1 in Ref. [21]. However, with the band itself extended to a higher spin, and in view of the observed signature partner, a [22,23] configuration assignment is now more reasonable also from the point of view of $J^{(2)}$ moments of inertia. On the contrary, based solely on the $J^{(2)}$ value, [22,13] is another possible assignment because it has a very similar curvature in Fig. 5(b) and, thus, a very similar $J^{(2)}$ (not shown in Fig. 6). The low value of $J^{(2)}$ for WD1 and configuration [22,02] reflects the large curvature in the upper panels in Fig. 5. Finally, SD3 is not observed at frequencies high enough to give any clear configuration preference related to $J^{(2)}$ values.

In summary, combining data from several fusion-evaporation reaction experiments using the Gammasphere finally allowed solving of the configuration assignment puzzle of the very first $A \sim 60$ SD band in ^{62}Zn [4,21]. Three more SD bands were experimentally observed in ^{62}Zn, two of which were also readily characterized by means of cranked Nilsson-Strutinsky calculations.

We would like to thank the accelerator crews and the Gammasphere support staff at Argonne and Berkeley for their superb efforts.

[1] B. Singh, R. Zywina, and R. B. Firestone, Nucl. Data Sheets **97**, 241 (2002).
[2] I. Ragnarsson, S. G. Nilsson, and R. K. Sheline, Phys. Rep. **45**, 1 (1978).
[3] J. Dudek, W. Nazarewicz, Z. Szymanski, and G. A. Leander, Phys. Rev. Lett. **59**, 1405 (1987).
[4] C. E. Svensson *et al.*, Phys. Rev. Lett. **79**, 1233 (1997).
[5] W. Reviol *et al.*, Phys. Rev. C **65**, 034309 (2002).
[6] D. Rudolph *et al.*, Phys. Rev. Lett. **82**, 3763 (1999).
[7] E. K. Johansson *et al.*, Phys. Rev. C **77**, 064316 (2008).
[8] D. Rudolph *et al.*, Phys. Rev. Lett. **96**, 092501 (2006).
[9] E. K. Johansson *et al.*, Phys. Rev. C **80**, 014321 (2009).
[10] C.-H. Yu *et al.*, Phys. Rev. C **65**, 061302(R) (2002).
[11] D. A. Torres *et al.*, Phys. Rev. C **78**, 054318 (2008).
[12] D. Rudolph *et al.*, Phys. Rev. Lett. **80**, 3018 (1998).
[13] C. Andreoiu *et al.*, Phys. Rev. C **62**, 051301(R) (2000).
[14] C. Andreoiu *et al.*, Eur. Phys. J. A **14**, 317 (2002).
[15] C. Andreoiu *et al.*, Phys. Rev. Lett. **91**, 232502 (2003).
[16] L.-L. Andersson *et al.*, Eur. Phys. J. A **36**, 251 (2008).
[17] C. E. Svensson *et al.*, Phys. Rev. Lett. **82**, 3400 (1999).
[18] C.-H. Yu *et al.*, Phys. Rev. C **60**, 031305(R) (1999).
[19] L.-L. Andersson *et al.*, Phys. Rev. C **79**, 024312 (2009).
[20] C. E. Svensson, C. Baktash, G. C. Ball, J. A. Cameron, M. Devlin, J. Eberth, S. Flibotte, A. Galindo Uribarri, and D. S. Haslip, Phys. Rev. Lett. **80**, 2558 (1998).
[21] A. V. Afanasjev, I. Ragnarsson, and P. Ring, Phys. Rev. C **59**, 3166 (1999).
[22] I.-Y. Lee, Nucl. Phys. **A520**, 641c (1990).
[23] D. G. Sarantites *et al.*, Nucl. Instrum. Methods Phys. Res. A **381**, 418 (1996).
[24] M. Devlin *et al.*, Nucl. Instrum. Methods Phys. Res. A **383**, 506 (1996).
[25] C. E. Svensson *et al.*, Nucl. Instrum. Methods Phys. Res. A **396**, 228 (1997).
[26] B. Cederwall *et al.*, Nucl. Instrum. Methods Phys. Res. A **354**, 591 (1995).
[27] D. C. Radford, Nucl. Instrum. Methods Phys. Res. A **361**, 297 (1995).
[28] J. Theuerkauf *et al.*, program TV, University of Cologne (unpublished).
[29] J. Gellanki *et al.* (to be published).
[30] T. Bengtsson and I. Ragnarsson, Nucl. Phys. **A436**, 14 (1985).
[31] A. V. Afanasjev, D. B. Fossan, G. J. Lane, and I. Ragnarsson, Phys. Rep. **322**, 1 (1999).
[32] B. G. Carlsson and I. Ragnarsson, Phys. Rev. C **74**, 011302(R) (2006).
[33] I. Ragnarsson, V. P. Janzen, D. B. Fossan, N. C. Schmeing, and R. Wadsworth, Phys. Rev. Lett. **74**, 3935 (1995).
[34] J. J. Valiente-Dobon *et al.*, Phys. Rev. Lett. **95**, 232501 (2005).

Paper II

High spin structure studies in ^{62}Zn

J. Gellanki,[1] **D. Rudolph,**[1] **I. Ragnarsson,**[2]
L.-L. Andersson,[1,‡] **C. Andreoiu,**[1,3,§] **M. P. Carpenter,**[4]
J. Ekman,[1,‖] **C. Fahlander,**[1] **E. K. Johansson,**[1] **W. Reviol,**[5]
D. G. Sarantites,[5] **D. Seweryniak,**[4] **C. E. Svensson,**[3]

[1] Department of Physics, Lund University, Lund, Sweden
[2] Division of Mathematical Physics, LTH, Lund University, Lund, Sweden
[3] Department of Physics, University of Guelph, Canada
[4] Physics Division, Argonne National Laboratory, U.S.A.
[5] Chemistry Department, Washington University, St. Louis, U.S.A.

E-mail: `gellanki.jnaneswari@nuclear.lu.se`

Abstract. A detailed experimental study of the ^{62}Zn nucleus has been performed by combining the data sets from four fusion-evaporation reaction experiments. Apart from the previously published data, the present results include some ten new rotational band structures and one new superdeformed band. The Gammasphere Ge-detector array in conjunction with the 4π charged-particle detector array Microball allowed for the detection of γ-rays in coincidence with evaporated light particles. The deduced level scheme includes some 250 excited states, which are connected with 430 γ-ray transitions. The multipolarities have been assigned via directional correlations of γ-rays emitted from oriented states. The experimental characteristics of the rotational bands are analyzed and compared with results from Cranked Nilsson-Strutinsky calculations.

PACS numbers: 21.60.Cs, 23.20.En, 23.20.Lv, 27.50.+e

Submitted to: *Phys. Scr.*

1. Introduction

In recent years, modern germanium detector arrays like GAMMASPHERE [1] in conjunction with the charged particle arrays such as Microball [2] have been used to identify nuclear structure properties at high spin in the $A \sim 60$ mass region, like band termination, highly deformed bands, superdeformed bands, prompt proton decays and shape changes [3, 4, 5, 6, 7, 8, 9, 10, 11, 12, 13, 14, 15, 16, 17, 18, 19]. An interesting feature in this mass region is that the same nuclei can exhibit various kinds of the above mentioned nuclear phenomena [6, 10, 13, 18, 20]. To generate the high-spin states required for the observation of most of the collective phenomena, it is necessary to break the $Z = N = 28$ core and to excite nucleons into the intruder $1g_{9/2}$ subshell.

‡ Present address: Helmholtz-Institut Mainz, D-55099 Mainz, Germany.
§ Present address: Chemistry Department, Simon Fraser University, Burnaby, BC, V5a 1S6, Canada.
‖ Present address: Malmö högskola, S-20506 Malmö, Sweden.

2. Experimental Details

The low-lying states in ^{62}Zn including two terminating bands and one unlinked superdeformed band were established in previous studies [16, 17]. Three superdeformed bands were resolved in our recent study [21]. The combined statistics of four different experiments performed at Argonne and Lawrence Berkeley National Laboratories were used to identify the excited states of ^{62}Zn. Detailed description of these experiments are given in [6, 8, 10, 13, 14]. The first experiment which has high counting statistics used the fusion-evaporation reaction ^{40}Ca(^{28}Si,$1\alpha 2p$)^{62}Zn at a beam energy of 122 MeV. The target had a thickness of 0.5 mg/cm^2 and an isotopic enrichment of 99.975%. The relative population cross section for ^{62}Zn was $\sim$ 30%. The other three experiments utilized the fusion-evaporation reaction ^{28}Si(^{36}Ar,$2p$)^{62}Zn at similar beam energies, $\sim$ 140 MeV, leading to a small population cross section for ^{62}Zn. All four experiments used the 4π Ge-detector array GAMMASPHERE [1] combined with the particle detector Microball [2]. The statistics from the first experiment was used to identify the normally deformed, well deformed, and superdeformed band structures including their decay-out transitions. The combined statistics of the remaining three experiments was used to add the highest-spin states on top of the superdeformed bands. In all experiments the heavimet collimators in front of the Ge detectors were removed to provide γ-ray multiplicity and sum-energy measurements [22] and additional channel selectivity by total energy conservation requirements [23].

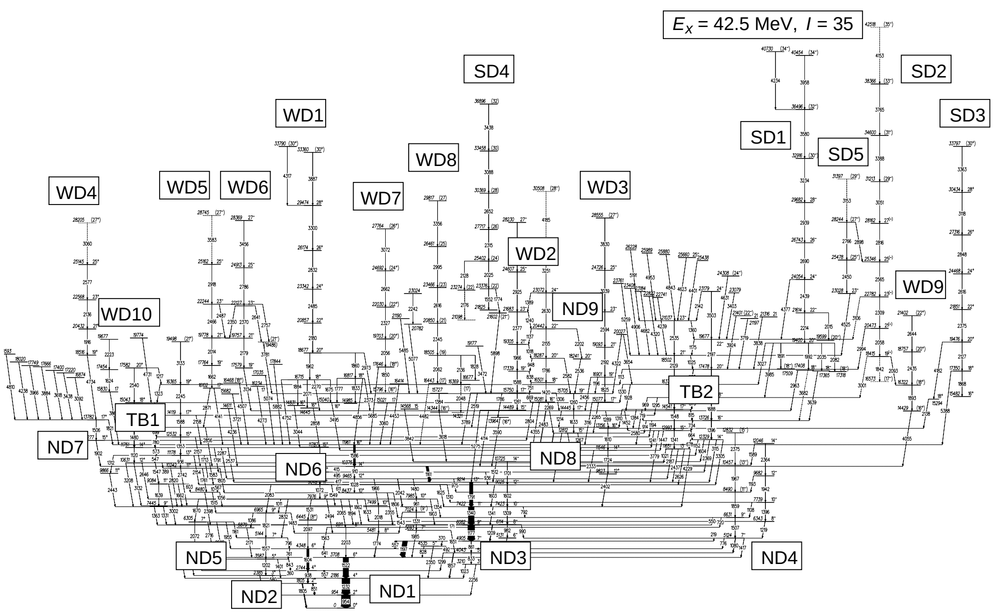

Figure 1. Overview of the complex level scheme of ^{62}Zn as obtained in the present study. The various normal deformed (ND), terminating (TB), well-deformed (WD), and superdeformed (SD) bands are labeled.

3. Analysis and Results

The γ-ray events were sorted offline into various γ-ray energy projections, $E_\gamma - E_\gamma$ matrices, and $E_\gamma - E_\gamma - E_\gamma$ cubes subject to appropriate evaporated particle conditions. Analysis of the cube and the matrices was carried out using the RADWARE software package [24] and the spectrum-analysis code Tv [25]. A kinematic correction [26, 27] was used to aid in the Doppler correction. The assignment of multipolarities to the γ-rays was done by using directional correlations from the oriented states (DCO ratios).

The current results confirm the previous results for the lower-spin states and reveal much more information at high spin. The complete level scheme deduced for ^{62}Zn is indicated in Fig. 1. Since it comprises about 430 γ-ray transitions and 250 excited states, its detailed presentation is subject to an extensive study in a forthcoming publication [20]. To ease the discussion, the level scheme is classified into normal deformed structures (ND1-ND9), the known terminating bands (TB1,TB2) [17], as well as a number of well-deformed (WD1-WD10) and superdeformed (SD1-SD5) bands in Fig. 1. The level energies, the corresponding depopulating γ-rays, their relative intensities, angular-correlation ratios, and resulting spin-parity assignments are summarized in Ref. [20].

The highest spin deduced from a connected band in the previous study is 24^- at 23214 keV [17]. Our recent publication [21] focused on three superdeformed bands and one well deformed band, where the observed maximum spin is (35^-) at 42.5 MeV excitation energy. The present level scheme in Fig. 1 adds a few new low-spin normal deformed structures, nine well-deformed bands (WD2-WD10), and two superdeformed bands (SD4,SD5). Some structures (e.g. WD2) consist of two signature partner bands, which will be denoted with (a) and (b) in addition to the band label.

All highly deformed rotational structures were identified up to $I \sim$ 25-28 $\hbar$ whereas the superdeformed bands were observed up to $I \sim$ 30-35 $\hbar$. Most of the excited rotational bands were connected to the low-spin normal deformed states by a number of linking transitions. In most cases, this allowed for firm, but sometimes only tentative spin and parity assignments to the lowest states in the bands. For example, the lowest state at 16102 keV of WD5 decays into the normal deformed 16^+ state at 11961 keV via a 4141-keV decay-out transition. The $R_{DCO}(4141) = 0.51(10)$ is consistent with $\Delta I = 1$ character, suggesting $I = 17$ to the 16102-keV state. The tentative spin and parity assignments to the states near the top of the bands are based on their regular rotational behaviour.

A spectrum in coincidence with the 4355 keV decay-out transition of WD2b and any one of the band members of WD2b (1420, 1786, 2155 and 2630 keV) is shown in Fig. 2. It illustrates the high sensitivity of the first experiment, with small relative yields such as 0.04% for the gating 4355 keV transition and about 2% for the band members. The triple coincidences both with band members of WD2b (1420, 1786, 2155, 2630, and 3251 keV) and with the relevant transitions in the normal deformed region (954, 1177, 1197, 1232, 1309, 1340, 1341, 1512, 1522, 1602-1604, and 1701 keV) are clearly visible. The weak connecting transitions 838 and 1018 keV between signature partner bands WD2a and WD2b are also marked. The peak at 2925 keV belongs to WD2a. The presence of a 2355-keV peak marked in red is related to contamination arising from the intense, yrast $13^- \rightarrow 11^-$ 1791-keV γ-ray transition, which has nearly the same energy as the band member at 1786 keV.

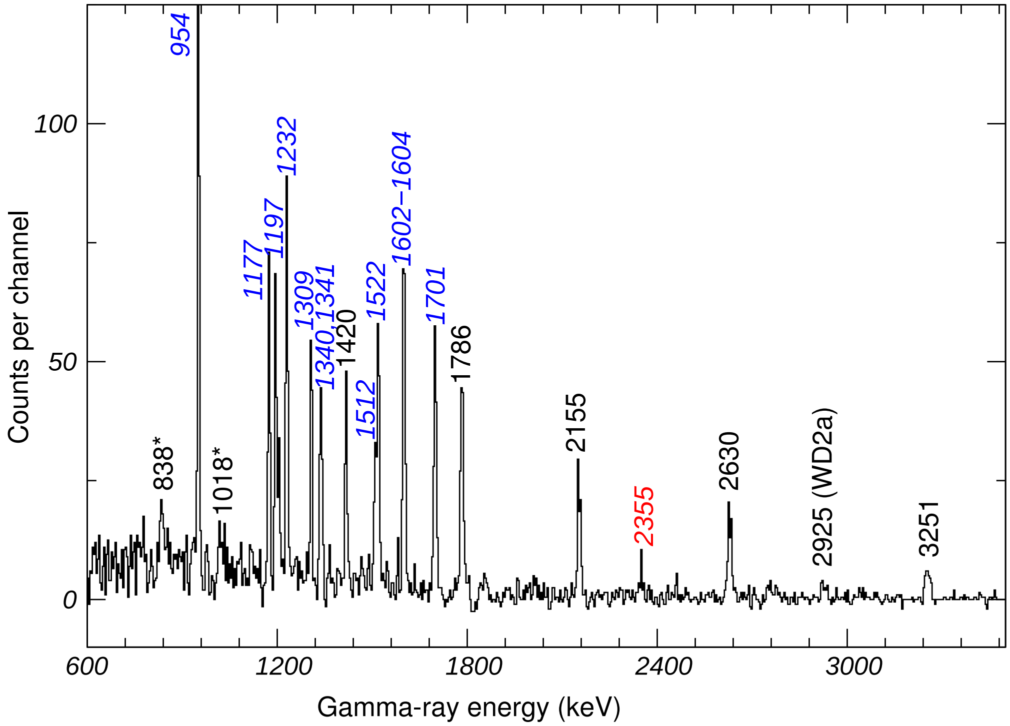

Figure 2. Coincidences with the 4355-keV decay-out transition of WD2b and any one of the band members of WD2b at 1420, 1786, 2155, and 2630 keV. Transitions from the normal deformed part of the level scheme are marked in blue and italic style, while the band members including the 2925 keV transition of WD2a are marked in black. The transitions at 838 and 1018 keV connecting WD2a and WD2b are marked with a star (*). The peak at 2355 keV is a contaminant.

4. Theoretical Interpretations

The experimental bands were analyzed using the configuration-dependent cranked Nilsson-Strutinsky (CNS) model [28, 29, 30]. These calculations are based on the cranking model [31, 32], with the single-particle eigenvalues calculated from the Nilsson Hamiltonian [28]. The total energy of fixed configurations is minimized in the deformation parameters ϵ_2, γ and ϵ_4 at each spin. Pairing effects are neglected since the formalism has been developed to describe the high-spin structures.

The orbitals involved for a description of ^{62}Zn include those of the $\mathcal{N} = 3$ high-j $1f_{7/2}$ shell, the upper fp shell comprising $1f_{5/2}$, $2p_{3/2}$ and $2p_{1/2}$, and finally the $\mathcal{N} = 4$ $1g_{9/2}$ shell. The configurations are labeled $[p_1p_2,n_1n_2]$, where p_1 (n_1) is the number of proton (neutron) holes in the $1f_{7/2}$ subshell and p_2 (n_2) is the number of proton (neutron) particles in the $1g_{9/2}$ shell. For example, the ground-state band configuration $\pi(2p_{3/2}1f_{5/2})^2\nu(2p_{3/2}1f_{5/2})^4$ of ^{62}Zn is labeled as [00,00]. In order to form regular rotational bands, it is necessary to lift protons or neutrons across the $Z = N = 28$ spherical shell gaps from the $1f_{7/2}$ shell, while the excitation of particles to the $1g_{9/2}$ shell is important to increase the deformation and to generate angular momentum [10].

In Fig. 3, some of the bands are compared with the CNS predictions. The upper

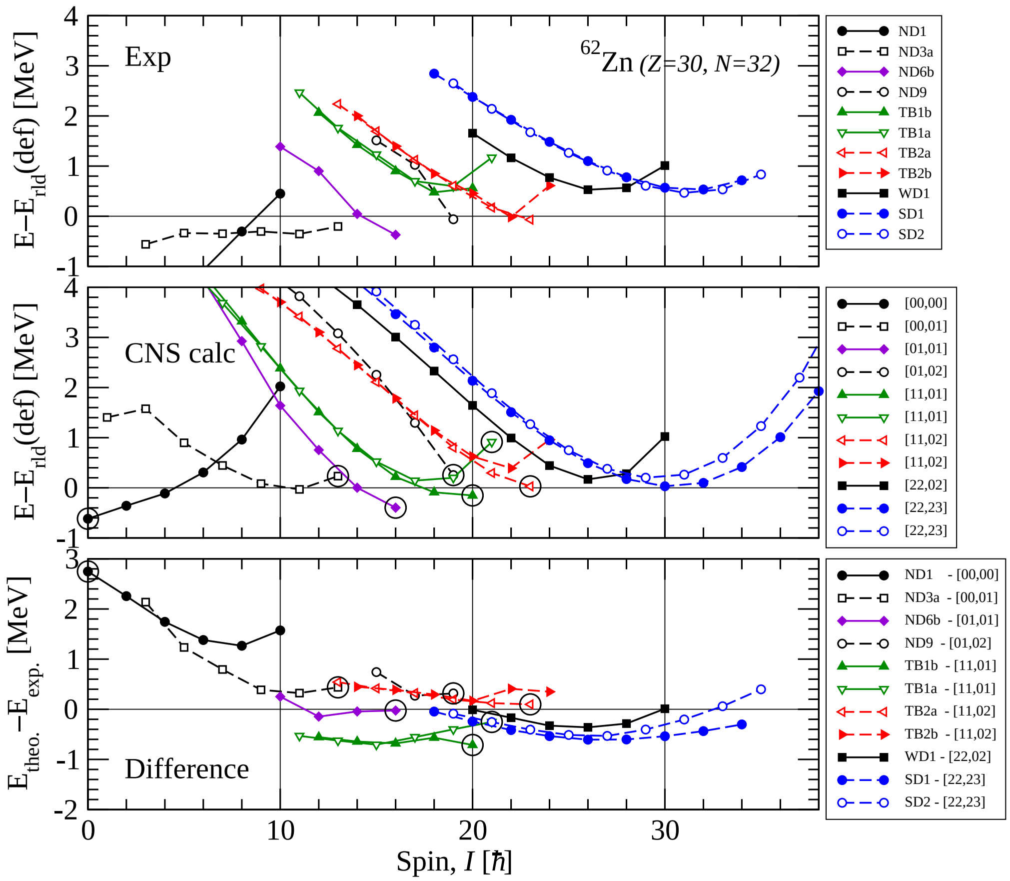

Figure 3. Comparison between some of the observed structures (cf. Fig. 1) and CNS predictions for ^{62}Zn. The top panel illustrates the experimental results where the bands are labeled according to Fig. 1. The middle panel shows the chosen predicted bands. The bottom panel plots the energy difference between the prediction and observation.

panel shows the experimental energies relative to the rotating liquid drop energy. The middle panel shows selected calculated bands, and the lower panel indicates the difference between the experimental and calculated bands. If perfect agreement between the theoretical and experimental bands existed, the values in the lower panel would be equal to zero. One can note that a constant energy difference in the lower panel implies that the experimental transition energies are reproduced by the calculated band. The previously known terminating bands TB1 and TB2 are in agreement with the [11,01] and [11,02] configurations. The well-deformed band WD1 is assigned to the [22,02] configuration, whereas the two superdeformed bands SD1 and SD2 are assigned as signature partners of the [22,23] configuration. The other well-deformed bands (WD2-WD10) are typically formed with three particles in the $1g_{9/2}$ shell and two $1f_{7/2}$ holes, while the superdeformed bands have three to four $1f_{7/2}$ holes and four to six $1g_{9/2}$ particles. More details about the band configurations are discussed in Ref. [20].

References

[1] I.-Y. Lee, Nucl. Phys. **A520**, 641c (1990).
[2] D.G. Sarantites *et al.*, Nucl. Instr. Meth. **A381**, 418 (1996).
[3] W. Reviol *et al.*, Phys. Rev. C **65**, 034309 (2002).
[4] D. Rudolph *et al.*, Phys. Rev. Lett. **96**, 092501 (2006).
[5] E.K. Johansson *et al.*, Phys. Rev. C **77**,064316 (2008).
[6] E.K. Johansson *et al.*, Phys. Rev. C **80**, 014321 (2009).
[7] C.-H. Yu *et al.*, Phys. Rev. C **65**, 061302(R) (2002).
[8] D.A. Torres *et al.*, Phys. Rev. C **78**, 054318 (2008).
[9] D. Rudolph *et al.*, Phys. Rev. Lett. **80**, 3018 (1998).
[10] C. Andreoiu *et al.*, Eur.Phys. J. A**14**, 317 (2002).
[11] C. Andreoiu *et al.*, Phys. Rev. Lett. **91**, 232502 (2003).
[12] C. Andreoiu *et al.*, Phys. Rev. C **62**, 051301(R) (2000).
[13] L.-L. Andersson *et al.*, Eur. Phys. J. A**36**, 251 (2008).
[14] C.E. Svensson *et al.*, Phys. Rev. Lett. **82**, 3400 (1999).
[15] C.-H. Yu *et al.*, Phys. Rev. C **60**, 031305(R) (1999).
[16] C.E. Svensson *et al.*, Phys. Rev. Lett. **79**, 1233 (1997).
[17] C.E. Svensson *et al.*, Phys. Rev. Lett. **80**, 2558(1998).
[18] L.-L. Andersson *et al.*, Phys. Rev. C **79**, 024312 (2009).
[19] D. Karlgren *et al.*, Phys. Rev. C **69**, 034330 (2004).
[20] J. Gellanki *et al.*, submitted to Phys. Rev. C.
[21] J. Gellanki *et al.*, Phys. Rev. C **80**, 051304(R) (2009).
[22] M. Devlin *et al.*, Nucl. Instr. Meth. **A383**, 506 (1996).
[23] C.E. Svensson *et al.*, Nucl. Instr. Meth. **A396**, 288 (1997).
[24] D. C. Radford, Nucl. Instr. Meth. **A361**, 297 (1995).
[25] J. Theuerkauf, S. Esser, S. Krink, M. Luig, N. Nicolay, O. Stuch, H. Wolters, Program Tv, University of Cologne, unpublished.
[26] C.J. Chiara *et al.*, Nucl. Instr. Meth. **A523**, 374 (2004).
[27] D. Seweryniak *et al.*, Nucl. Instr. Meth. **A340**, 353 (1994).
[28] T. Bengtsson and I. Ragnarsson, Nucl. Phys. **A436**, 14 (1985).
[29] A. V. Afanasjev, D. B. Fossan, G. J. Lane, and I. Ragnarsson, Phys. Rep. **322**, 1 (1999).
[30] B. G. Carlsson and I. Ragnarsson, Phys. Rev. C **74**, 011302(R) (2006).
[31] D.R. Inglis, Phys. Rev. **96**, 1059 (1954).
[32] D.R. Inglis, Phys. Rev. **103**, 1786 (1956).

Paper III

Extensive γ-ray spectroscopy of rotational band structures in $^{62}_{30}Zn_{32}$

J. Gellanki,[1] D. Rudolph,[1] I. Ragnarsson,[2] L.-L. Andersson,[1,*] C. Andreoiu,[1,†] M.P. Carpenter,[4] J. Ekman,[1,‡] C. Fahlander,[1] E.K. Johansson,[1,§] W. Reviol,[5] D.G. Sarantites,[5] D. Seweryniak,[4] C.E. Svensson,[3] J.C. Waddington,[3]

[1] *Department of Physics, Lund University, S-22100 Lund, Sweden*

[2] *Division of Mathematical Physics, LTH, Lund University, S-22100 Lund, Sweden*

[3] *Department of Physics, University of Guelph, Guelph, Ontario, N1G 2W1, Canada*

[4] *Physics Division, Argonne National Laboratory, Argonne, Illinois 60439, U.S.A. and*

[5] *Chemistry Department, Washington University, St. Louis, Missouri 63130, U.S.A.*

(Dated: December 6, 2011)

A detailed experimental study of the ^{62}Zn nucleus has been performed by combining the data sets from four fusion-evaporation reaction experiments. Apart from the previously published data, the present results include nine new rotational band structures and two more superdeformed bands. The Gammasphere Ge-detector array in conjunction with the 4π charged-particle detector array Microball allowed for the detection of γ-rays in coincidence with evaporated light particles. The deduced level scheme includes some 250 excited states, which are connected with 430 γ-ray transitions. Spins and parities of the excited states have been determined via directional correlations of γ-rays emitted from oriented states. The experimental characteristics of the rotational bands are analyzed and compared with results from Cranked Nilsson-Strutinsky calculations. The present analysis, combined with available experimental results in the $A \sim 60$ mass region, can be used to improve the current set of Nilsson parameters in the $\mathcal{N} = 3$ and $\mathcal{N} = 4$ oscillator shells.

PACS numbers: 21.60.Cs, 23.20.En, 23.20.Lv, and 27.40.+z

I. INTRODUCTION

The investigation of high angular momentum states in atomic nuclei has long been a topical question in nuclear structure physics. Here, reliable and comprehensive high-spin studies of neutron-deficient nuclei in the mass $A \sim 60$ region require extra efforts, because of different experimental challenges compared with heavier nuclei. With the combination of advanced γ-ray and particle-detector arrays such as GAMMASPHERE [1] and Microball [2] these difficulties can be handled, and resulted in several nuclear structure highlights in $N \sim Z$, $A \sim 60$ nuclei such as, to name but a few, discrete-energy particle decay-out transitions [3–6], quests for isospin $T = 0$ pairing [7, 8], record-high rotational frequencies [9], or 'complete' high-spin excitations schemes comprising coexisting spherical, deformed and superdeformed states [10, 11].

High-spin collectivity in the $A \sim 60$ mass region is induced by particle-hole excitations across the spherical shell gap at particle number $N = Z = 28$. A limited number of holes in the $1f_{7/2}$ orbital and excitation of one or more nucleons into $1g_{9/2}$ intruder orbital above the ^{56}Ni closed core gives rise to nuclear structure phenomena associated with collective excitations, including superdeformation [10–18], favored and unfavored band termination [19–21], as well as bands with strong magnetic dipole transitions [22, 23]. Unlike in other mass regimes, almost all rotational bands in the mass $A \sim 60$ region could be connected with the low-spin spherical states in the first minimum of the nuclear potential, let it be by γ rays or proton- or α-decay lines.

Previously published data on ^{62}Zn includes low- and medium-spin structures and two terminating bands [17, 20]. Our most recent study highlighted three superdeformed bands together with one well-deformed band [18]. The present paper may be viewed as the summarising high-spin spectroscopy study of ^{62}Zn. The resulting level scheme comprises some 250 energy levels and 430 γ-ray transitions. An overview of the proposed decay scheme of ^{62}Zn is sketched in Fig. 1. The proposed maximum spin is $I = 35\ \hbar$ at an excitation energy of $E_x = 42.5$ MeV; numbers comparable only to ^{58}Ni [9]. Apart from the previous results, the present level scheme includes a number of low-spin, normally deformed structures, nine new highly-deformed rotational bands, and last but not least two additional superdeformed bands.

Following a brief description of the underlying experiments and analysis tools in Sec. II, the results concerning the different structures of the complex decay scheme of Fig. 1 are presented thoroughly in Sec. III. Finally, the experimentally observed states are systematically discussed in the framework of the cranked Nilsson-Strutinsky approach in Sec. IV, thereby adding some new information to the previously published results [18, 20].

*Present address: Helmholtz-Institut Mainz, D-55099 Mainz, Germany.

†Present address: Chemistry Department, Simon Fraser University, Burnaby, BC, V5A 1S6, Canada.

‡Present address: Malmö högskola, S-20506 Malmö, Sweden.

§Present address: XXX

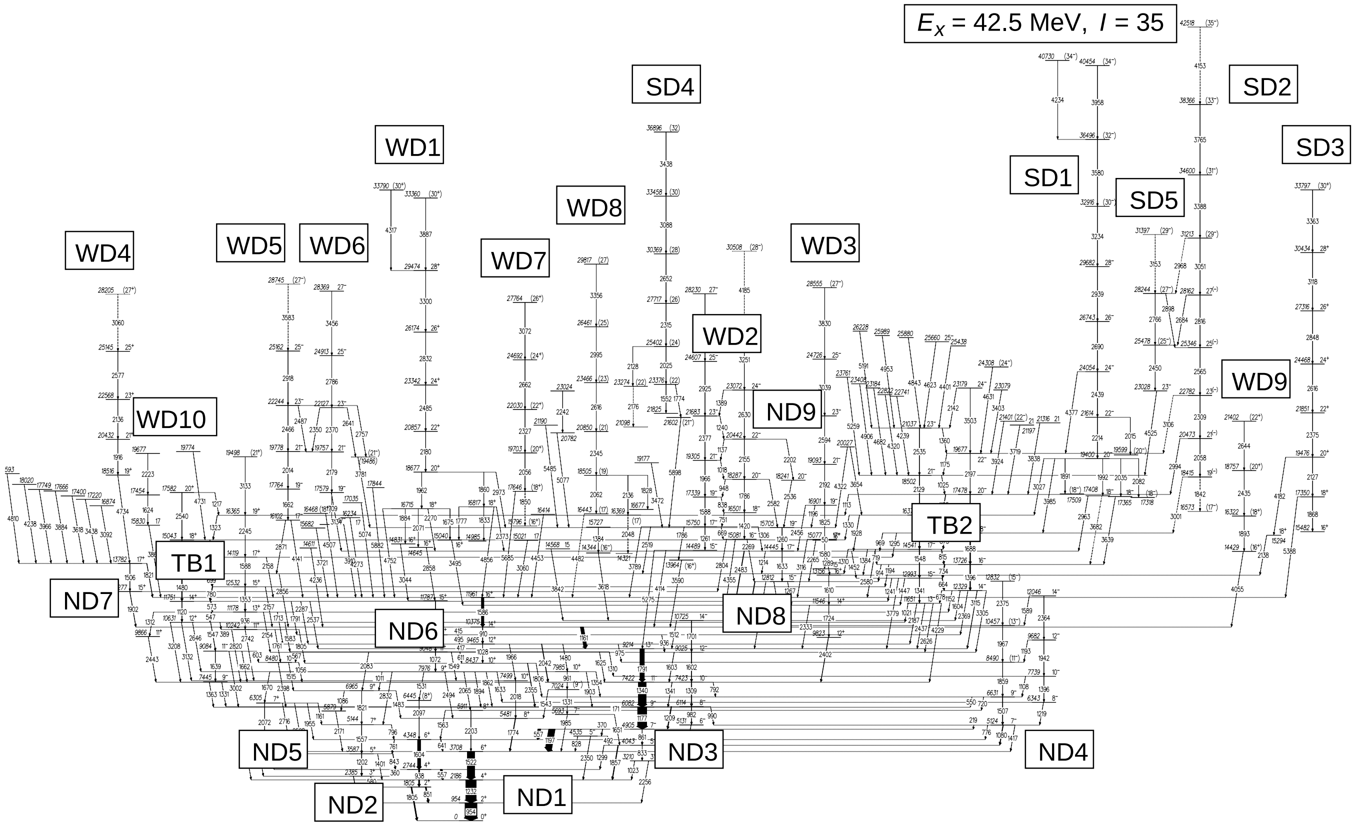

FIG. 1: Proposed high-spin level scheme of ^{62}Zn. Due to the complexity of the level scheme, spins, parities, and energies of the excited states as well as labels of γ-ray transitions are generally too small to be readable. The structures are labeled according to the descriptions and discussions in the text. Detailed decay schemes of each structure or band are presented in subsequent figures.

II. EXPERIMENTAL DETAILS AND ANALYSIS PROCEDURES

The results presented in this paper originate from the combined statistics from four different experiments carried out with the Gammasphere Ge-detector array [1] at Argonne and Lawrence Berkeley National Laboratories. A brief description is given below. More detailed explanations about the experiments are, for example, provided in Refs. [10, 24, 25].

In brief, one experiment used the fusion-evaporation reaction ^{40}Ca(^{28}Si,1α2p)^{62}Zn at a beam energy of 122 MeV. The target had an isotopic enrichment of 99.975 % and a thickness of 0.5 mg/cm^2. ^{62}Zn nuclei were populated with $\approx$ 30% of the total fusion cross section. The experimental setup consisted of the Gammasphere array (103 Ge detectors at the time of experiment) in combination with the Microball charged-particle array [2] inside the target chamber. The Heavimet collimators were removed from the Ge-detector modules to provide γ-ray multiplicity and sum-energy measurements [26] as well as additional channel selectivity based on total energy conservation requirements [27]. The statistics from this experiment are denoted as 'data set 1'. In fact, data set 1 was the main source used to construct the level scheme of ^{62}Zn displayed in Fig. 1. The role of data set 1 is to identify the normally deformed, low- and high-spin rotational and, most importantly, superdeformed bands including their decay-out transitions.

Furthermore, three Gammasphere experiments have been performed using the fusion-evaporation reaction ^{28}Si(^{36}Ar,2p)^{62}Zn at a beam energies of about 140 MeV. Increasingly complex charged-particle detection systems were employed aiming at high-resolution particle-γ coincidence spectroscopy (see, e.g., Refs. [3, 11, 25] for more details), and arrays of neutron detectors replaced a number of Ge-detector modules at forward angles. In all these experiments, the Heavimet collimators were also removed. Hence, by applying specific selection criteria on the data (see below), the combined statistics of these three experiments (called 'data set 2') allowed to add the highest-spin states of the superdeformed bands – despite the fact that the relative yield for the production of ^{62}Zn residues is very small at such high compound nucleus excitation energies.

An event-by-event kinematical reconstruction of the momenta of the recoil nuclei [28] was performed for all four experiments. This implies a more accurate Doppler-shift correction of the γ-ray energies, leading to a significantly improved γ-ray energy resolution. The events were sorted offline into various E_γ projections, $E_\gamma - E_\gamma$ matrices, and $E_\gamma - E_\gamma - E_\gamma$ cubes subject to appropriate evaporated-particle conditions, including total γ-ray energy, charged-particle energy, and γ-ray multiplicity conditions for the ^{62}Zn reaction channel.

The analysis employed the Radware software package [29] and the spectrum analysis code Tv [30]. Low intensity or ambiguous transitions were confirmed by specific $\gamma\gamma$ matrices, which were preselected by γ rays originating from a certain rotational band or decay sequence within the complex ^{62}Zn level scheme. For data set 2, a special $\gamma\gamma$ matrix was created, which focused solely on high-lying entry states in ^{62}Zn; here, at least 14 detected γ rays with at least 16.5 MeV total energy and less than 19 MeV particle energy were required, similar to a procedure outlined in Ref. [9].

The main result of the $\gamma\gamma$ and $\gamma\gamma\gamma$-coincidence analysis is the decay scheme of ^{62}Zn, shown in Fig. 1. It is based on energy and coincidences relations, intensity balances and summed-energy relations. Excitation energies, γ-ray energies, relative γ-ray transition yields, angular correlation ratios, and multipolarity assignments are summarized in Table I.

Assignments of spins and parities of the excited levels were based on the analysis of the $1\alpha2p$-gated directional $\gamma\gamma$ correlations of oriented states (DCO-ratios). The Ge-detectors of Gammasphere were grouped into three "pseudo" rings called "30", "53", and "83", which correspond to an average angle for the respective set of detectors while accounting for γ-ray emission symmetry with respect to the 90°-plane perpendicular to the beam. Matrices for three combinations of the angles were created, namely 30-83, 30-53, and 53-83; for instance, for the latter γ-rays detected at 53° were sorted on one axis and those detected at 83° placed on the other axis of the correlation matrix.

The determination of the most discriminating DCO-ratios, R_{DCO}(30-83), was attempted for all experimentally observed γ-ray transitions, while special emphasis was given to pronounced transitions such as, for example, those linking the deformed or superdeformed rotational bands to the normally deformed low-spin part of the ^{62}Zn level scheme. However, due to limited statistics, the DCO-ratios of some of the γ rays could not be evaluated. The R_{DCO}(30-83)-values were extracted according to the formula

$$R_{DCO} = \frac{I(\gamma_1 \text{ at } 30^\circ;\ \text{gated with } \gamma_2 \text{ at } 83^\circ)}{I(\gamma_1 \text{ at } 83^\circ;\ \text{gated with } \gamma_2 \text{ at } 30^\circ)}, \qquad (1)$$

with I denoting the intensities of γ rays in the respective γ-ray coincidence spectra.

The DCO-ratios given in Table I were obtained by using known or in the course of the analysis deduced stretched $E2$ transitions as gating transitions (see, for example, Refs. [31–33] for the theoretical background and practical procedures). In this case, for observed stretched $\Delta I = 2$ transitions $R_{DCO}(30\text{-}83) = 1.0$ is expected. For pure stretched $\Delta I = 1$ transitions, $R_{DCO}(30\text{-}83) \sim 0.6$. However, $\Delta I = 1$ transitions can show deviations due to quadrupole admixtures, i.e., non-zero $\delta(E2/M1)$ mixing ratios. $M2$ and higher multipole orders than quadrupole transitions are neglected due to their significantly reduced decay probabilities. Non-stretched $\Delta I = 0$ transitions yield typically $R_{DCO}(30\text{-}83) = 0.9$, i.e. numbers similar to stretched $E2$ transitions. Nevertheless, since the γ-ray decay path in nuclei populated via fusion-evaporation reactions follows the yrast line, $\Delta I = 0$ transitions are rare and usually have small relative intensities. Moreover, for complex level schemes like the one proposed for ^{62}Zn, parallel γ-ray decay branches, often put additional constraints on possible spin- and parity assignments to the excited states

An analysis of mixing ratios, $\delta(E2/M1)$, was performed for several $\Delta I = 1$ transitions based on DCO-ratios arising from the three different angle combinations. The phase conservation of Rose and Brink [34] is applied, and the procedure follows the one outlined in Ref. [33]. In particular, the alignment coefficients, α_2, were estimated through the relation

$$\alpha_2 = 0.55 + 0.02 \cdot E_x \text{ [MeV]}, \Delta\alpha_2 = \pm 0.05 \qquad (2)$$

while limited to a maximum of $\alpha_2 < 0.90$. In case of non-unique solutions of $\delta(E2/M1)$, they are provided in Table I as either two values or estimates, or as a range of possible values (cf. Ref. [33]).

III. RESULTS

The level scheme of ^{62}Zn as obtained in the present study is sketched in Fig. 1 with all relevant numbers summarized in Table I. It should be stressed and noted here that the amount of coincidence statistics paired with the spectroscopic resolving power of the experimental setup allowed for unambiguous placements of γ rays with relative intensities down to the level of 10^{-4}.

The figure indicates both the low-spin normally deformed (ND1-ND7) part of the level scheme, the previously published two terminating band structures TB1 and TB2 [20], highly deformed rotational structures (Q1-Q9), as well as the recently highlighted three superdeformed and one well-deformed band structures (SD1-SD3 and WD1) [18]. It includes in addition one more superdeformed band structure (SD4).

In the following, the different sections of the extensive new decay scheme are introduced and described by means of a few selected γ-ray spectra and R_{DCO}-values. All rotational bands were connected to the low-spin normally deformed states by one or several linking transitions. This allowed for either firm, but in some cases only for tentative spin and parity assignments to the lowest

TABLE I: The energies of excited states in ^{62}Zn, the transitions energies and relative intensities of the γ rays placed in the level scheme, the DCO-ratios of three different angle combinations, the deduced mixing ratios, and the spins and parities of the initial and final states of the γ rays.

E_x (keV)	E_γ (keV)	I_{rel} (%)	Gate[a] X^Y	R_{DCO} 30°-83°	30°-53°	53°-83°	$\delta(E2/M1)$	Mult. Ass.	I_i^π ($\hbar$)	I_f^π ($\hbar$)
				ND1-ND7						
954.0(3)	953.9(3)	10000(300)	1232	0.93(4)				$E2$	2^{+b}	0^+
1804.7(3)	850.9(3)	980(29)	1604	0.93(6)				$\Delta I=0$	2^{+b}	2^+
	1805.0(5)	851(44)	1604	1.12(9)				$E2$	2^+	0^+
2186.2(3)	1231.9(3)	8780(260)	954	1.12(5)				$E2$	4^{+b}	2^+
2384.6(3)	580.1(2)	205(6)	1604	0.36(7)	0.57(8)	0.68(5)	$\approx 0.15; \approx 2.1$	$E2/M1$	3^{+b}	2^+
	1430.6(6)	277(14)	1557	0.84(9)	1.05(9)	0.95(8)	-0.30($^{7}_{6}$)	$E2/M1$	3^+	2^+
2743.8(3)	359.5(2)	171(5)	1604	0.39(4)	0.74(7)	0.70(5)	0.13($^{10}_{7}$)	$E2/M1$	4^{+b}	3^+
	557.3(3)	1730(130)	1604	0.80(5)[c]				$\Delta I=0$	4^+	4^+
	938.4(4)	987(43)	1604	0.98(5)				$E2$	4^+	2^+
3209.9(4)	1023.4(5)	42(5)	1177	0.50(18)				$E1$	3^{-b}	4^+
	2256.1(16)	12(2)						$E1$	3^-	2^+
3586.9(4)	843.2(3)	374(19)	1557	0.28(2)	0.58(5)	0.54(4)	$\approx 0.39; \approx 1.9$	$E2/M1$	5^{+b}	4^+
	1202.2(5)	355(18)	1557	1.04(6)				$E2$	5^+	3^+
	1400.7(11)	8(2)						$E2/M1$	5^+	4^+
3707.7(3)	1521.6(4)	6240(190)	954	1.14(5)				$E2$	6^{+b}	4^+
4043.2(4)	833.3(3)	56(4)	1177	1.03(19)				$E2$	5^{-b}	3^-
	1299.4(5)	187(9)	1177	0.63(6)				$E1$	5^-	4^+
	1857.4(7)	598(27)	1232	0.66(4)				$E1$	5^-	4^+
4231.1(6)	643.9(8)	7(1)						$\Delta I=0$	5^{+d}	5^+
	1487.1(15)	5(1)						$E2/M1$	5^+	4^+
	1845.8(17)	8(3)						$E2$	5^+	3^+
	2044.8(18)	8(1)						$E2/M1$	5^+	4^+
4348.2(4)	640.6(2)	360(11)	1522	0.95(8)				$\Delta I=0$	6^{+b}	6^+
	761.4(2)	261(8)	1202	0.53(6)	0.66(9)	0.73(7)	0.07($^{10}_{8}$)	$E2/M1$	6^+	5^+
	1604.4(4)	2650(90)	954	1.19(5)[c]				$E2$	6^+	4^+
4535.4(4)	492.4(2)	39(5)						$\Delta I=0$	5^-	5^-
	827.7(4)	57(7)	1522	0.39(11)				$E1$	5^-	6^+
	2349.8(9)	190(14)	1232	0.64(5)[c]				$E1$	5^-	4^+
4904.9(4)	369.7(2)	248(7)	1177	0.92(7)				$E2$	7^{-b}	5^-
	556.9(5)	2480(130)	1522	0.59(3)				$E1$	7^-	6^+
	861.4(3)	259(8)	1177	1.01(11)				$E2$	7^-	5^-
	1196.8(6)	5310(160)	1177	0.57(2)				$E1$	7^-	6^+
5124.1(4)	219.3(2)	42(3)	1507	0.87(11)				$\Delta I=0$	7^{-b}	7^-
	775.8(7)	9(1)						$E1$	7^-	6^+
	1080.4(4)	543(22)	1507	1.14(8)				$E2$	7^-	5^-
	1416.8(6)	148(10)	1507	0.53(7)				$E1$	7^-	6^+
5131.4(5)	1088.0(4)	133(8)	1309	0.32(5)	0.71(8)	0.38(6)	$0.1 < \delta < 3.1$	$E2/M1$	6^{-b}	5^-
5144.0(4)	795.8(3)	113(8)	1604	0.39(9)	0.65(12)	0.58(10)	0.23($^{32}_{13}$);2.6($^{19}_{10}$)	$E2/M1$	7^+	6^+
	1557.2(6)	324(15)	1072	1.12(10)				$E2$	7^+	5^+
5481.4(6)	1773.8(7)	491(34)	1232	1.10(8)				$E2$	8^{+b}	6^+
5693.4(8)	1650.9(12)	21(2)	1857	0.94(29)				$E2$	7^-	5^-
	1985.1(16)	17(4)	1522	0.41(17)				$E1$	7^-	6^+
5878.8(8)	2171.0(9)	35(4)								6^+
5910.7(5)	1562.8(9)	6(2)						$E2$	8^{+d}	6^+
	2203.2(11)	28(3)						$E2$	8^+	6^+
6081.7(5)	171.0(3)	17(3)						$E1$	9^{-b}	8^+
	1176.7(4)	7710(230)	1791	1.03(5)				$E2$	9^-	7^-
6113.7(5)	981.8(4)	86(7)	1602	1.30(32)				$E2$	8^{-b}	6^-
	990.2(6)	21(4)	1309	0.62(9)				$E2/M1$	8^-	7^-
	1208.8(5)	626(28)	1309	0.96(5)	1.19(6)	0.86(5)	-0.35(5);-2.8($^{4}_{5}$)	$E2/M1$	8^-	7^-
6304.5(6)	1160.8(11)	9(4)						$\Delta I=0$	7^{+d}	7^+
	1954.9(17)	8(1)						$E2/M1$	7^+	6^+
	2073.0(12)	13(1)						$E2$	7^+	5^+
	2597.6(17)	13(1)						$E2/M1$	7^+	6^+
	2716.3(16)	23(1)	1072	0.94(16)				$E2$	7^+	5^+

TABLE I: Continued.

E_x (keV)	E_γ (keV)	I_{rel} (%)	Gate[a]	R_{DCO} 30°-83°	30°-53°	53°-83°	$\delta(E2/M1)$	Mult. Ass.	I_i^π ($\hbar$)	I_f^π ($\hbar$)
6343.0(7)	1219.0(7)	85(4)	1080	0.31(3)	0.67(5)	0.57(4)	$0.22(^{12}_{8})$;2.3(6)	$E2/M1$	8^-	7^-
6444.9(10)	2097.1(12)	45(3)	1604	0.81(34)				$(E2)$	(8^+)	6^+
6631.1(5)	549.6(8)	8(1)						$\Delta I=0$	9^-[b]	9^-
	720.5(10)	11(1)						$E1$	9^-	8^+
	1507.2(6)	411(21)	1080	1.05(6)				$E2$	9^-	7^-
6964.8(6)	1085.8(11)	16(3)							9^+	
	1483.3(13)	8(2)						$E2/M1$	9^+	8^+
	1821.0(10)	74(5)	1557	1.15(8)				$E2$	9^+	7^+
7024.3(8)	1331.2(9)	41(5)	1480	0.97(7)[c]				$(E2)$	(9^-)	7^-
	1543.1(13)	18(4)	1774	0.40(10)[c]				$(E1)$	(9^-)	8^+
7422.4(5)	1340.4(4)	6580(210)	1177	1.05(5)				$E2$	11^-[b]	9^-
7422.9(5)	791.7(8)	11(1)	1701	0.44(10)				$E2/M1$	10^-[b]	9^-
	1309.3(5)	584(37)	1701	0.97(5)				$E2$	10^-	8^-
	1341.4(7)	203(36)	1701	0.94(7)[c]				$E2/M1$	10^-	9^-
7444.9(6)	1331.1(9)	14(3)						$E2/M1$	9^-	8^-
	1363.3(5)	29(2)	1639	1.13(12)				$\Delta I=0$	9^-	9^-
7499.2(8)	2017.8(9)	159(8)	1774	1.03(8)				$E2$	10^+[b]	8^+
7739.1(6)	1108.2(4)	108(4)	1080	0.55(6)				$E2/M1$	10^-	9^-
	1396.4(10)	55(3)	1080	0.88(9)				$E2$	10^-	8^-
7975.6(5)	1011.0(9)	8(1)						$\Delta I=0$	9^+[b]	9^+
	1531.2(13)	8(1)						$(E2/M1)$	9^+	(8^+)
	1632.6(12)	33(5)	1072	0.66(38)				$E1$	9^+	8^-
	1670.4(7)	45(2)	1072	1.32(22)				$E2$	9^+	7^+
	1862.2(13)	24(3)	1072	0.66(7)				$E1$	9^+	8^-
	1894.2(8)	46(3)	1072	1.01(13)				$\Delta I=0$	9^+	9^-
	2065.0(18)	17(3)	1072	0.83(14)				$E2/M1$	9^+	8^+
	2831.9(14)	104(9)	1072	1.16(10)				$E2$	9^+	7^+
7985.0(7)	961.0(9)	51(6)	911	0.42(9)				$(E1)$	10^+	(9^-)
	1353.6(12)	9(3)						$E1$	10^+	9^-
	1902.7(17)	16(5)						$E1$	10^+	9^-
8437.1(6)	1806.0(17)	9(2)						$E1$	10^+[b]	9^-
	2354.9(12)	328(19)	1028	0.67(5)				$E1$	10^+	9^-
8480.1(6)	1056.1(6)	25(3)	1340	0.57(15)				$\Delta I=1$	10	11^-
	1515.3(15)	8(2)						$\Delta I=1$	10	9^+
	2398.3(17)	14(2)						$\Delta I=1$	10	9^-
8489.9(8)	1859.0(11)	121(5)	1080	0.74(5)[c]				$(E2)$[e,f]	(11^-)	9^-
9024.6(6)	1601.7(7)	483(37)	1309	1.02(6)[c]				$E2$	12^-	10^-
	1602.7(8)	211(24)	1701	0.82(5)[c]				$E2/M1$	12^-	11^-
9047.9(5)	566.6(6)	27(3)	911	0.68(8)				$\Delta I=1$	11^+[b]	10
	610.9(6)	26(3)	911	0.42(12)				$E2/M1$	11^+	10^+
	1072.2(7)	290(11)	911	1.08(6)				$E2$	11^+	9^+
	1310.0(8)	50(4)						$E1$	11^+	10^-
	1625.0(9)	149(6)	911	0.59(4)				$E1$	11^+	10^-
	1548.6(12)	11(2)	911	0.58(18)				$E2/M1$	11^+	10^+
	2083.0(18)	13(1)	911					$E2$	11^+	9^+
9083.6(6)	603.2(7)	16(3)	1177					$\Delta I=1$	11^-	10
	1638.7(8)	67(5)	1177	0.93(7)[c]				$E2$	11^-	9^-
	1661.7(10)	35(4)						$\Delta I=0$	11^-	11^-
	3002.1(12)	54(3)						$E2$	11^-	9^-
9213.8(6)	1791.3(6)	3760(130)	1177	1.08(5)				$E2$	13^-[b]	11^-
9464.8(5)	416.9(2)	151(5)	1586	0.44(9)[c]				$E2/M1$	12^+[b]	11^+
	974.8(10)	15(3)						$E1$	12^+	11^-
	1027.6(4)	216(11)	1586	0.90(10)				$E2$	12^+	10^+
	1479.8(9)	83(6)	1586	0.96(16)				$E2$	12^+	10^+
	1965.5(18)	9(2)						$E2$	12^+	10^+
	2042.5(11)	432(18)	1586	0.51(5)				$E1$	12^+	11^-
9681.8(11)	1192.7(13)	11(1)						$E2/M1$	12^-	(11^-)
	1942.0(14)	18(2)	1080	0.97(17)				$E2$	12^-	10^-

TABLE I: Continued.

E_x (keV)	E_γ (keV)	I_{rel} (%)	Gate^a	R_{DCO} 30°-83°	30°-53°	53°-83°	$\delta(E2/M1)$	Mult. Ass.	I_i^π ($\hbar$)	I_f^π ($\hbar$)
9823.0(8)	2401.7(9)	290(9)	1724	0.63(6)				$E1$	12^{+d}	11^-
9866.0(9)	2442.9(13)	45(1)	1353	0.46(10)				$E1$	11^+	10^-
9959.9(6)	495.1(5)	14(2)						$E2/M1$	13^+	12^+
	911.2(8)	381(18)	1072	1.08(6)				$E2$	13^+	11^+
	935.7(8)	119(6)	1309	0.72(5)				$E1$	13^+	12^-
10374.7(6)	414.8(4)	27(2)	1586	0.44(9)^c				$E2/M1$	14^{+b}	13^+
	909.6(6)	463(19)	1028	1.01(8)				$E2$	14^+	12^+
	1160.9(5)	2710(90)	1586	0.54(3)				$E1$	14^+	13^-
10456.9(13)	1966.9(15)	107(7)	1080	1.12(11)				$E2$	(13^-)	(11^-)
10725.4(7)	1511.6(7)	57(6)	1791	0.59(5)	0.91(8)	0.86(6)	$-0.11(^{6}_{5})$	$E2/M1$	14^-	13^-
	1701.0(9)	292(13)	1309	1.09(6)				$E2$	14^-	12^-
11546.0(7)	1723.7(7)	112(5)	1340	1.09(6)				$E2$	14^+	12^+
	2333.1(13)	62(4)	1791	0.53(9)				$E1$	14^+	13^-
11786.7(10)	1826.7(9)	348(14)	911	1.07(4)				$E2$	15^+	13^+
11961.2(7)	1586.4(5)	2170(70)	1340	1.05(5)^c				$E2$	16^{+b}	14^+
12046.2(15)	1589.2(13)	32(3)						$(E2/M1)^{e,f}$	(14^-)	13^-
	2364.5(19)	9(1)						$(E2)$	(14^-)	12^-
12276.7(8)	1901.8(7)	245(15)	1791	0.35(3)	0.55(6)	0.43(4)	$0.26(^{9}_{7}); 2.5(^{7}_{6})$	$E2/M1$	15^+	14^+
12812.4(7)	1266.9(5)	80(5)	1633	0.64(9)				$E1$	15^{-b}	14^+
	2355.4(20)	6(2)						$E2$	15^-	13^-
	2436.9(9)	482(22)	1340	0.68(4)				$E1$	15^-	14^+
	3597.1(22)	11(1)						$E2$	15^-	13^-
12831.5(18)	2374.6(14)	25(2)						$(E2)^e$	(15^-)	(13^-)
13156.3(8)	1610.3(10)	75(4)	1724	1.40(15)				$E2$	16^+	14^+
13782.4(9)	1505.6(8)	63(3)	910	1.14(17)				$E2$	17^+	15^+
	1821.3(5)	283(16)	1586	0.35(3)	0.43(4)	0.45(4)	$0.26(^{9}_{7}); 1.7(^{10}_{7})$	$E2/M1$	17^+	16^+
14343.9(12)	3618.4(10)	17(2)	1701	0.95(19)				$(E2)$	(16^-)	14^-
14444.9(6)	718.8(3)	112(5)	1396	0.55(6)	0.92(9)	0.96(9)	$-0.10(^{7}_{6})$	$E2/M1$	17^{-b}	16^-
	1214.2(10)	12(1)						$E1$	17^-	16^+
	1288.8(8)	22(5)						$E1$	17^-	16^+
	1452.1(12)	10(1)						$E2$	17^-	15^-
	1632.8(7)	208(11)	1791	0.91(9)				$E2$	17^-	15^-
	2483.4(12)	492(30)	1586	0.52(3)				$E1$	17^-	16^+
14567.8(22)	3842.4(21)	22(3)	1701	0.66(9)				$\Delta I = 1$	15	14^-
14610.5(29)	4235.8(28)	25(5)								14^+
15020.8(19)	3059.6(18)	37(2)	1586	0.75(10)				$\Delta I = 1$	17	16^+
15682.2(25)	3721.0(24)	9(1)								16^+
15704.6(7)	1259.6(4)	344(15)	1633	1.04(11)				$E2$	19^-	17^-
15727.4(19)	1383.5(14)	13(1)								16^-
16234.4(33)	4273.2(32)	17(1)	1586	0.58(10)				$\Delta I = 1$	17	16^+
16414.0(27)	4452.8(26)	13(2)								16^+
16467.8(29)	4506.6(28)	29(2)	1586	0.86(18)				$(E2)^e$	(18^+)	16^+
16874.2(25)	3091.8(23)	11(2)								17^+
17035.2(33)	5074.0(32)	11(2)								16^+
17220.0(28)	3437.6(27)	8(2)								17^+
17400.1(28)	3617.7(27)	8(2)								17^+
17665.9(26)	3883.5(25)	19(2)								17^+
17748.8(32)	3966.4(31)	9(1)								17^+
17843.6(43)	5882.4(42)	3(1)								16^+
18020.3(35)	4237.9(34)	12(1)								16^+
18592.6(37)	4810.2(36)	9(1)								17^+
19177.0(25)	3472.4(24)	12(1)								19^-
20781.9(42)	5077.3(41)	5(1)								19^-
21189.7(49)	5485.1(42)	4(1)								19^-
23024.2(46)	2242.3(19)	3(1)								

TABLE I: Continued.

E_x (keV)	E_γ (keV)	I_{rel} (%)	Gate[a]	R_{DCO} 30°-83°	30°-53°	53°-83°	$\delta(E2/M1)$	Mult. Ass.	I_i^π ($\hbar$)	I_f^π ($\hbar$)
				TB1						
10241.9(6)	1761.3(15)	13(2)						$\Delta I=1$	11^{+b}	10
	1804.7(15)	14(3)						$E2/M1$	11^+	10^+
	2742.2(18)	34(4)	1774	1.10(16)				$E2/M1$	11^+	10^+
	2819.9(19)	27(3)	936	0.97(13)				$\Delta I=0$	11^+	11^-
10630.7(6)	388.8(4)	98(4)	1120	0.59(8)	0.93(15)	0.70(9)	$-0.06(^{9}_{8})$	$E2/M1$	12^{+b}	11^+
	1547.2(6)	243(8)	1120	0.59(5)				$E1$	12^+	11^-
	1582.6(12)	13(2)						$E2/M1$	12^+	11^+
	2645.6(21)	12(3)						$E2$	12^+	10^+
	3132.1(19)	29(3)	1120	1.11(23)				$E2$	12^+	10^+
	3208.4(18)	63(3)	1120	0.54(8)				$E1$	12^+	11^-
11177.9(6)	547.2(2)	505(13)	1353	0.71(4)	0.92(5)	0.79(4)	-0.16(4)	$E2/M1$	13^{+b}	12^+
	936.1(7)	107(5)	TB1	0.86(7)				$E2$	13^+	11^+
	1311.8(9)	33(4)						$E2$	13^+	11^+
	1712.2(13)	19(4)						$E2/M1$	13^+	12^+
	2154.0(14)	55(4)	1353	0.43(7)[c]				$E1$	13^+	12^-
11751.2(6)	573.3(2)	448(13)	TB1	0.63(5)	0.90(7)	0.80(4)	$-0.12(^{5}_{4})$	$E2/M1$	14^{+b}	13^+
	1120.0(11)	294(8)	TB1	1.29(12)				$E2$	14^{+b}	12^+
	2286.6(18)	16(3)						$E2$	14^+	12^+
	2537.4(14)	121(8)	1480	0.59(11)[c]				$E1$	14^+	13^-
12531.6(6)	780.4(3)	537(16)	1120	0.64(5)	1.09(10)	0.82(6)	$-0.15(^{6}_{5})$	$E2/M1$	15^{+b}	14^+
	1353.3(8)	427(14)	1588	1.01(5)				$E2$	15^+	13^+
	2156.9(17)	36(5)						$E2/M1$	15^+	14^+
13231.1(6)	699.4(3)	501(15)	1353	0.69(4)	0.84(5)	0.73(5)	$-0.11(^{5}_{4})$	$E2/M1$	16^{+b}	15^+
	1479.6(7)	687(22)	1120	1.04(12)				$E2$	16^+	14^+
	2856.2(21)	39(4)						$E2$	16^+	14^+
14119.1(7)	888.0(4)	296(9)	1480	0.68(7)	0.92(8)	0.85(5)	$-0.18(^{6}_{5})$	$E2/M1$	17^{+b}	16^+
	1587.7(10)	195(6)	TB1	1.28(11)[c]				$E2$	17^+	15^+
	2157.7(20)	42(5)	1586	0.74(9)[c]				$E2/M1$	17^+	16^+
15042.7(7)	923.6(5)	233(8)	1588	0.67(6)	1.01(8)	0.81(6)	-0.18(5)	$E2/M1$	18^{+b}	17^+
	1811.3(8)	261(9)	1120	1.26(10)				$E2$	18^+	16^+
16365.2(9)	1322.8(9)	181(12)	1811	0.47(6)	0.85(8)	0.76(8)	-0.04(6)	$E2/M1$	19^{+b}	18^+
	2245.3(15)	96(6)	1120	1.15(22)				$E2$	19^+	17^+
17582.4(12)	1217.3(11)	65(5)	2245	0.76(12)				$E2/M1$	20^{+b}	19^+
	2539.7(14)	165(13)	1811	1.10(11)				$E2$	20^+	18^+
19498.1(25)	3132.9(23)	26(2)						$(E2)$[f]	(21^+)	19^+
19773.8(39)	4731.1(38)	8(2)								18^+
				TB2						
11651.3(6)	1021.2(11)	8(3)						$E1$	13^{-b}	12^+
	2187.0(19)	9(2)						$E1$	13^-	12^+
	2436.1(16)	31(5)						$\Delta I=0$	13^-	13^-
	2626.3(16)	31(2)						$E2/M1$	13^-	12^-
	4228.0(28)	59(6)	1340	1.30(21)				$E2$	13^-	11^-
12329.2(6)	678.0(3)	143(5)	1396	0.72(6)	0.84(7)	0.90(8)	-0.15(5)	$E2/M1$	14^{-b}	13^-
	1151.6(7)	31(2)	1396	0.42(7)				$E1$	14^-	13^+
	1604.1(13)	16(5)						$\Delta I=0$	14^-	14^-
	2369.4(17)	23(4)						$E1$	14^-	13^+
	3115.2(18)	240(19)	1396	0.93(10)				$E2/M1$	14^-	13^-
	3304.9(14)	11(2)						$E2$	14^-	12^-
12992.7(6)	663.7(3)	527(16)	1548	0.61(4)	0.88(5)	0.81(5)	-0.12(4)	$E2/M1$	15^{-b}	14^-
	1241.4(7)	105(6)	1548	0.54(6)				$E1$	15^-	14^+
	1341.4(8)	163(51)	1688	1.01(8)[c]				$E2$	15^-	13^-
	1446.8(10)	14(2)						$E1$	15^-	14^+
	3779.3(29)	18(4)	1791	0.85(18)				$E2$	15^-	13^-
13726.0(6)	733.5(3)	662(15)	1688	0.60(4)	0.82(5)	0.74(5)	$-0.07(^{4}_{3})$	$E2/M1$	16^{-b}	15^-
	913.6(5)	57(5)	1688	0.67(8)	0.94(10)	0.96(12)	-0.16(6)	$E2/M1$	16^-	15^-
	1193.9(9)	53(8)	1688	0.62(6)[c]				$E1$	16^-	15^+
	1396.4(7)	634(21)	1688	0.97(7)				$E2$	16^-	15^-

TABLE I: Continued.

E_x (keV)	E_γ (keV)	I_{rel} (%)	Gate[a]	R_{DCO} 30°-83°	30°-53°	53°-83°	$\delta(E2/M1)$	Mult. Ass.	I_i^π ($\hbar$)	I_f^π ($\hbar$)
14540.9(6)	814.9(4)	469(15)	1396	0.64(4)	0.92(5)	0.77(4)	-0.14(4)	$E2/M1$	17^-[b]	16^-
	1309.6(9)	91(5)	2064	0.59(5)[c]				$E1$	17^-	16^+
	1384.2(10)	21(3)						$E1$	17^-	16^+
	1548.3(7)	581(22)	2064	1.18(15)				$E2$	17^-	15^-
	2580.7(14)	186(7)	2064	0.69(6)				$E1$	17^-	16^+
15414.1(7)	873.2(4)	312(10)	2064	0.72(4)	0.88(5)	0.77(5)	-0.16(4)	$E2/M1$	18^-[b]	17^-
	969.3(6)	189(6)	2064	0.69(6)	1.08(9)	0.68(7)	-0.19(10); $-6.8(^{13}_{53})$	$E2/M1$	18^-	17^-
	1295.0(8)	67(5)						$E1$	18^-	17^+
	1688.4(7)	706(25)	2064	0.96(4)				$E2$	18^-	16^-
16372.7(7)	959.0(5)	359(16)	1688	0.77(7)[c]	0.86(8)	0.84(8)	$-0.19(^{8}_{7})$	$E2/M1$	19^-	18^-
	1329.6(9)	37(3)						$E1$	19^-	18^+
	1831.4(8)	506(16)	TB2	1.15(10)				$E2$	19^-	17^-
	1927.6(10)	222(8)	1633	1.14(10)				$E2$	19^-	17^-
17477.8(8)	1105.1(6)	345(13)	1688	0.69(13)				$E2/M1$	20^-[b]	19^-
	1112.6(12)	9(1)						$E1$	20^-	19^+
	2063.8(10)	503(17)	TB2	1.00(8)				$E2$	20^-	18^-
18502.0(9)	1024.6(6)	101(5)	2064	0.85(6)	0.82(6)	0.67(5)	-0.18(9)	$E2/M1$	21^-[b]	20^-
	2129.1(11)	437(14)	TB2	1.04(10)				$E2$	21^-	19^-
19676.5(10)	1174.8(6)	99(6)	TB2	[c]				$E2/M1$	22^-[b]	21^-
	2197.0(13)	171(8)	TB2	1.03(11)				$E2$	22^-	20^-
20026.7(24)	3654.2(30)	15(2)								19^-
	4321.8(37)	5(2)								19^-
21036.8(11)	1360.2(5)	72(4)	TB2	0.53(7)[c]				$E2/M1$	23^-[b]	22^-
	2535.0(13)	163(6)	TB2	0.98(14)				$E2$	23^-	21^-
21196.7(32)	3719.2(31)	21(1)	TB2	0.61(19)				$\Delta I = 1$	21	20^-
21316.1(30)	3838.3(29)	24(2)	TB2	0.73(10)				$\Delta I = 1$	21	20^-
21401.3(30)	3923.5(29)	35(2)	TB2	0.96(10)				$(E2)$	(22^-)	20^-
22741.3(41)	4239.3(40)	10(2)								21^-
22822.4(34)	4320.4(33)	15(2)								21^-
23079.2(27)	3402.7(25)	21(2)								22^-
23179.1(16)	2142.2(16)	27(2)						$E2/M1$	24^-[b]	23^-
	3502.7(21)	65(5)	TB2	1.33(19)				$E2$	24^-	22^-
23184.2(39)	4682.2(38)	8(2)								21^-
23407.8(44)	4905.8(43)	6(1)								21^-
23761.3(45)	5259.3(44)	4(1)								21^-
24307.7(38)	4631.2(37)	18(2)	TB2	1.26(14)[c]				$(E2)$	$(24)^-$	22^-
25438.1(40)	4401.3(38)	5(1)								23^-
25660.2(33)	4623.4(26)	20(3)	TB2	1.16(15)				$E2$	25^-	23^-
25880.1(38)	4843.3(36)	11(1)								23^-
25989.4(41)	4952.7(39)	8(1)								23^-
26227.9(43)	5191.1(41)	8(1)								23^-
					WD1					
14644.6(14)	2858.3(20)	22(3)						$E2/M1$	16^+[d]	15^+
14831.2(13)	3043.5(21)	24(4)						$E2/M1$	16^+[d]	15^+
15040.3(12)	3494.8(25)	7(1)						$E2$	16^+[d]	14^+
16715.2(11)	1675.3(11)	20(2)						$E2$	18^+	16^+
	1883.7(10)	28(3)	WD1a	1.27(10)				$E2$	18^+	16^+
	2070.7(12)	51(3)	2180	1.11(13)				$E2$	18^+	16^+
	2270.5(17)	11(1)						$E2$	18^+	16^+
	4752.4(38)	13(2)	WD1a	1.36(18)				$E2$	18^+	16^+
16817.4(12)	1776.9(8)	65(4)	WD1b	1.04(14)				$E2$	18^+	16^+
	1832.7(9)	38(3)							18^+	
	2372.7(19)	12(1)						$E1$	18^+	17^-
	4856.4(32)	13(2)						$E2$	18^+	16^+
18677.3(12)	1859.7(10)	105(5)	WD1b	0.90(7)[c]				$E2$	20^+	18^+
	1962.3(11)	97(4)	WD1b	1.09(10)				$E2$	20^+	18^+
	2972.8(25)	8(2)						$E1$	20^+	19^-
20857.1(17)	2179.8(12)	195(7)	WD1b	1.04(10)				$E2$	22^+	20^+

TABLE I: Continued.

E_x (keV)	E_γ (keV)	I_{rel} (%)	Gate[a]	R_{DCO} 30°-83°	30°-53°	53°-83°	$\delta(E2/M1)$	Mult. Ass.	I_i^π ($\hbar$)	I_f^π ($\hbar$)
				WD2						
23341.7(22)	2484.6(14)	185(6)	WD1b	0.95(10)				$E2$	24^+	22^+
26173.9(30)	2832.2(20)	85(4)	WD1b	0.94(9)				$E2$	26^+	24^+
29473.7(40)	3299.8(26)	35(3)	WD1b	1.17(17)				$E2$	28^+	26^+
33360.4(50)	3886.7(31)[g]	11(2)						$(E2)$[f]	(30^+)	28^+
33790.5(52)	4316.8(34)[g]	9(2)						$(E2)$[f]	(30^+)	28^+
13964.4(13)	3589.7(17)	41(3)	910	1.46(37)				$(E2)$	(16^+)	14^+
14489.4(11)	4114.2(30)	12(1)	1791	0.69(15)				$E1$	15^-	14^+
	5275.0(35)	9(1)						$E2$	15^-	13^-
15081.2(9)	2269.2(14)	16(2)						$E2/M1$	16^-	15^-
	2803.9(17)	17(1)						$E1$	16^-	15^+
	4355.4(26)	38(2)	1701/1602	1.06(9)				$E2$	16^-	14^-
15750.2(8)	668.9(6)	17(2)						$E2/M1$	17^-	16^-
	1260.7(8)	78(6)	1966	1.09(10)				$E2$	17^-	15^-
	1306.0(11)	15(1)						$\Delta I=0$	17^-	17^-
	1785.7(14)	13(1)						$(E1)$	17^-	(16^+)
	2518.6(17)	21(3)						$E1$	17^-	16^+
	3788.7(22)	23(1)	1586	0.49(9)				$E1$	17^-	16^+
16500.7(9)	750.6(6)	11(1)						$E2/M1$	18^-	17^-
	1419.6(10)	98(9)	WD2b	1.01(15)				$E2$	18^-	16^-
17338.8(9)	838.2(5)	19(2)	1966	0.83(14)				$E2/M1$	19^-	18^-
	1587.5(9)	109(8)	1966	1.00(5)[c]				$E2$	19^-	17^-
18240.6(14)	2535.1(16)	41(3)	1260	0.43(6)				$E2/M1$	20^-	19^-
18286.9(10)	948.1(10)	7(2)						$E2/M1$	20^-	19^-
	1786.3(9)	161(9)	WD2b	1.10(8)				$E2$	20^-	18^-
	2581.8(15)	42(3)	1260	0.75(10)				$E2/M1$	20^-	19^-
19305.1(11)	1018.9(11)	9(1)						$E2/M1$	21^-	20^-
	1966.4(10)	173(7)	WD2a	1.10(10)				$E2$	21^-	19^-
20442.0(12)	1136.8(11)	7(2)						$E2/M1$	22^-	21^-
	2155.4(13)	172(7)	WD2b	1.00(10)				$E2$	22^-	20^-
	2201.6(17)	31(2)	WD2b	0.98(8)				$E2$	22^-	20^-
21682.5(14)	1240.5(13)	6(2)						$E2/M1$	23^-	22^-
	2377.3(13)	117(5)	WD2a	0.94(9)				$E2$	23^-	21^-
23072.1(16)	1388.4(14)	12(2)						$E2/M1$	24^-	23^-
	2630.2(15)	162(8)	WD2b	1.04(10)				$E2$	24^-	22^-
24607.1(22)	2924.6(17)	95(5)	WD2a	1.21(11)				$E2$	25^-	23^-
26323.4(24)	3251.3(18)	77(4)	WD2b	0.90(9)				$E2$	26^-	24^-
28229.7(40)	3622.6(33)	18(2)	WD2a	1.00(10)				$E2$	27^-	25^-
30508.3(44)	4185.0(37)	5(1)						$(E2)$[f]	(28^-)	26^-
				WD3						
15076.7(11)	1580.1(18)	11(2)						$(E2)$[f]	17^-	(15^-)
	2264.7(17)	8(2)						$E2$	17^-	15^-
	3116.2(18)	33(2)	1586	0.67(7)				$\Delta I=1$	17^-	16^+
16901.4(11)	1196.0(13)	9(3)						$\Delta I=0$	19^-	19^-
	1824.7(11)	95(4)	WD3	0.92(8)[c]				$E2$	19^-	17^-
	2456.2(20)	15(4)						$E2$	19^-	17^-
19093.2(16)	2192.0(12)	101(5)	WD3	0.97(10)				$E2$	21^-	19^-
21687.0(22)	2593.8(14)	75(4)	WD3	1.17(8)				$E2$	23^-	21^-
24725.6(28)	3038.6(18)	39(3)	WD3	1.03(16)				$E2$	25^-	23^-
28555.1(42)	3829.5(31)	7(2)						$(E2)$[f]	(27^-)	25^-
				WD4						
18516.4(29)	4734.0(28)	13(2)	WD4	1.20(25)				$E2$	19^+	17^+
20432.2(31)	1915.8(11)	52(4)	WD4	0.99(19)				$E2$	21^+	19^+
22567.7(34)	2135.5(14)	34(3)	WD4	1.06(10)				$E2$	23^+	21^+
25145.1(38)	2577.4(16)	16(2)	WD4	1.04(19)				$E2$	25^+	23^+
28205.3(45)	3060.2(25)	5(2)						$(E2)$[f]	(27^+)	25^+
				WD5 and WD6						
15869.8(20)	3908.9(31)	4(1)						$(E1)$	(17^-)	16^+
16101.9(16)	2870.8(22)	7(2)						$E1$[d]	17^-	16^+
	4141.0(29)	17(2)	1586	0.51(10)				$E1$	17^-	16^+

TABLE I: Continued.

E_x (keV)	E_γ (keV)	I_{rel} (%)	Gate[a]	R_{DCO} 30°-83°	30°-53°	53°-83°	$\delta(E2/M1)$	Mult. Ass.	I_i^π ($\hbar$)	I_f^π ($\hbar$)
17578.7(19)	1709.1(17)	9(2)						$(E2)^f$	19^-	(17^-)
	3134.4(26)	18(4)	2178	1.08(31)				$E2$	19^-	17^-
17764.3(17)	1662.4(10)	60(4)	WD6	1.15(10)				$E2$	19^-	17^-
19486.1(19)	3780.8(25)	29(3)	1260	1.19(27)				$E2$	21^-	19^-
19757.2(19)	2178.6(13)	45(4)	WD5	1.14(10)				$E2$	21^-	19^-
19777.8(18)	2013.5(13)	72(5)	WD6	1.12(11)				$E2$	21^-	19^-
22127.2(18)	2349.5(13)	33(2)	WD6	1.13(13)				$E2$	23^-	21^-
	2370.0(11)	40(3)	WD5	1.13(7)				$E2$	23^-	21^-
	2640.7(22)	7(2)						$E2$	23^-	21^-
22243.6(19)	2465.7(14)	43(3)	WD6	1.08(17)				$E2$	23^-	21^-
	2486.8(21)	3(1)						$E2$	23^-	21^-
	2757.4(23)	6(2)						$E2$	23^-	21^-
24912.7(24)	2785.5(16)	58(4)	WD5	0.93(14)				$E2$	25^-	23^-
25162.1(26)	2918.5(17)	32(2)	WD6	0.86(13)				$E2$	25^-	23^-
28369.1(35)	3456.4(25)	23(3)	WD5	1.27(46)				$(E2)$	(27^-)	25^-
28745.2(42)	3583.1(33)	5(2)						$(E2)^f$	(27^-)	25^-
				WD7						
17646.2(39)	1850.2(16)	11(2)						$(E2)^f$	(18^+)	(16^+)
	5685.0(38)	6(1)						$(E2)^e$	(18^+)	16^+
19702.6(41)	2056.4(14)	53(6)	WD7	1.16(16)[c]				$E2$	(20^+)	(18^+)
22030.0(44)	2327.0(15)	43(4)	WD7	1.18(10)[c]				$E2$	(22^+)	(20^+)
24692.3(47)	2662.3(18)	30(2)	WD7	1.04(26)				$E2$	(24^+)	(22^+)
27763.8(55)	3071.5(28)	7(1)						$(E2)^f$	(26^+)	(24^+)
16368.9(46)	2047.7(20)	8(2)							$(17)^f$	
				WD8						
16443.3(39)	4482.1(38)	5(2)						$\Delta I = 1^e$	(17)	16^+
18505.1(43)	1828.0(17)	12(2)							(19)	
	2061.8(19)	11(2)						$(E2)^f$	(19)	(17)
	2136.2(16)	18(2)						$(E2)^f$	(19)	(17)
20850.4(47)	2345.4(19)	31(2)						$(E2)^f$	(21)	(19)
23466.1(52)	2615.6(22)	27(2)						$(E2)^f$	(23)	(21)
26460.7(57)	2994.6(17)	14(1)						$(E2)^f$	(25)	(23)
29817.2(65)	3356.4(32)	4(1)						$(E2)^f$	(27)	(25)
				WD9						
14428.9(20)	4055.0(27)	48(4)	910	1.46(37)				$(E2)^e$	(16^+)	14^+
16322.1(19)	1893.4(11)	18(2)						$(E2)^f$	(18^+)	(16^+)
18757.4(25)	2435.3(15)	13(2)						$(E2)^f$	(20^+)	(18^+)
21401.6(32)	2644.2(20)	6(1)						$(E2)^f$	(22^+)	(20^+)
				WD10						
15829.9(24)	3869.0(27)	30(2)	1586	0.68(15)				$\Delta I = 1$	17	16^+
17453.8(27)	1623.9(13)	16(2)								17
19677.1(33)	2223.3(19)	12(3)								
				SD1						
17365.1(18)	3638.7(33)	5(1)						$E2$	18^-	16^-
17407.5(16)	2962.9(28)	6(1)	SD1	0.74(22)				$E2/M1$	18^-	17^-
	3682.0(34)	3(1)						$E2$	18^-	16^-
19399.9(15)	1891.3(15)	12(1)						$(E2)^f$	20^-	(18^-)
	1992.5(14)	18(1)	SD1					$E2^d$	20^-	18^-
	2034.7(14)	15(2)						$E2^d$	20^-	18^-
	2081.7(17)	9(1)						$(E2)^f$	20^-	(18^-)
	3027.4(24)	8(2)						$E2/M1$	20^-	19^-
	3984.9(31)	11(1)	SD1	1.12(39)				$E2$	20^-	18^-
21614.3(16)	2014.9(13)	13(2)						$(E2)^f$	22^-	(20^-)
	2214.4(9)	106(8)	SD1	0.99(13)				$E2$	22^-	20^-
24053.6(18)	2439.3(10)	131(7)	SD1	0.92(6)[c]				$E2$	24^-	22^-
	4377.1(34)	7(1)						$E2$	24^-	22^-
26743.4(22)	2689.9(12)	81(6)	SD1	0.99(10)				$E2$	26^-	24^-
29682.3(28)	2938.8(18)	28(2)	SD1	0.85(13)				$E2$	28^-	26^-

TABLE I: Continued.

E_x (keV)	E_γ (keV)	I_{rel} (%)	Gate[a]	R_{DCO} 30°-83°	30°-53°	53°-83°	$\delta(E2/M1)$	Mult. Ass.	I_i^π ($\hbar$)	I_f^π ($\hbar$)
32916.3(38)	3234.0(25)	7(2)						$(E2)^f$	(30^-)	28^-
36496.1(49)	3579.8(31)[g]	5(1)						$(E2)^f$	(32^-)	(30^-)
40454.4(61)	3958.3(37)[g]	3(1)						$(E2)^f$	(34^-)	(32^-)
40729.8(63)	4233.7(40)[g]	2(1)						$(E2)^f$	(34^-)	(32^-)
				SD2 and SD5						
18415.0(17)	1842.0(13)	6(1)						$(E2)^f$	$19^{(-)}$	(17^-)
	2093.2(16)	4(1)						$(\Delta I = 1)$	$19^{(-)}$	(18^+)
	3002.9(26)	5(1)						$(E2/M1)$	$19^{(-)}$	18^-
20472.6(17)	2057.8(12)	31(5)	SD2	1.02(21)				$E2$	$21^{(-)}$	$19^{(-)}$
	2994.0(30)	6(1)	SD2	0.61(20)				$\Delta I = 1$	$21^{(-)}$	20^-
22781.8(18)	2309.2(14)	45(4)	SD2	0.98(20)				$E2$	$23^{(-)}$	$21^{(-)}$
	3105.5(29)	9(1)						$\Delta I = 1$	$23^{(-)}$	22^-
23028.0(27)	4525.3(35)	24(2)	TB2	1.11(10)				$E2$	23^-	21^-
25346.4(22)	2564.8(14)	50(5)	SD2	1.06(7)				$E2$	$25^{(-)}$	$23^{(-)}$
25478.2(27)	2450.1(13)	18(2)						$(E2)^f$	(25^-)	23^-
28162.2(28)	2683.7(19)	5(2)						$(E2)$	$27^{(-)}$	(25^-)
	2815.7(18)	26(3)	SD2	0.85(22)				$E2$	$27^{(-)}$	$25^{(-)}$
28243.9(26)	2765.6(17)	7(2)						$(E2)^f$	(27^-)	(25^-)
	2897.7(21)	7(1)						$(E2)^f$	(27^-)	$25^{(-)}$
31212.8(36)	2967.8(22)	3(2)						$(E2)^f$	(29^-)	(27^-)
	3050.6(23)	10(2)						$(E2)^f$	(29^-)	$27^{(-)}$
31396.8(35)	3152.9(23)	8(2)						$(E2)^f$	(29^-)	(27^-)
34600.4(45)	3387.6(26)[g]	3(1)						$(E2)^f$	(31^-)	(29^-)
38365.8(56)	3765.4(34)[g]	2(1)						$(E2)^f$	(33^-)	(31^-)
42518.4(68)	4152.6(39)[g]	1(1)						$(E2)^f$	(35^-)	(33^-)
				SD3						
15294.2(16)	2138.0(15)	13(2)						$E2$	18^{+d}	16^+
17349.6(28)	1867.9(11)	31(3)	SD3	0.90(20)				$E2$	18^+	16^+
	5387.9(41)	17(2)	SD3	0.96(18)				$E2$	18^+	16^+
19476.4(28)	2126.8(12)	75(5)	2375	0.92(9)				$E2$	20^+	18^+
	4183.5(31)	7(1)						$E2$	20^+	18^+
21851.1(30)	2374.7(12)	77(6)	SD3	1.04(10)				$E2$	22^+	20^+
24467.5(33)	2616.4(14)	52(4)	SD3	1.00(9)				$E2$	24^+	22^+
27316.0(37)	2848.5(17)	23(3)	SD3	1.27(14)				$E2$	26^+	24^+
30433.7(43)	3117.7(21)	10(1)	SD3	0.86(24)				$E2$	28^+	26^+
33796.9(50)	3363.2(25)	3(1)	SD3					$(E2)^f$	(30^+)	28^+
				SD4						
21602.3(47)	5897.7(46)	3(1)						$(E2)^e$	(21^-)	19^-
23273.6(52)	2175.6(18)	17(3)							(22)	
23376.4(49)	1551.8(13)	17(2)							(22)	
	1774.1(12)	12(2)	SD4	0.59(8)				$\Delta I = 1$	(22)	(21^-)
25401.8(50)	2025.4(13)	41(3)	SD4	1.19(19)				$E2$	(24)	(22)
	2128.2(13)	38(4)	SD4	1.23(12)				$E2$	(24)	(22)
27717.2(52)	2315.4(14)	97(5)	SD4	1.13(13)				$E2$	(26)	(24)
30369.5(56)	2652.3(19)	58(4)	SD4	0.90(13)				$E2$	(28)	(26)
33457.8(61)	3088.3(24)	21(3)						$(E2)^f$	(30)	(28)
36896.3(68)	3438.4(32)[g]	6(2)						$(E2)^f$	(32)	(30)

[a]Gate on the transitions TB1: sum of 936, 1120, 1353, 1480, 1811 and 2245 keV; TB2: sum of 1396, 1548, 1688, 1831, 2064 and 2129 keV; WD1a: sum of 1962 and 2180 keV; WD1b: sum of 1860, 1962, 2180, 2485 and 2832 keV. WD2a: sum of 1261, 1588, 1966 and 2377 keV; WD2b: sum of 1420, 1786, 2155 and 2630 keV; WD3: sum of 1825, 2192, 2594 and 3039 keV; WD4: sum of 1916, 2136 and 2577 keV; WD5: sum of 2179, 2370 and 2786 keV; WD6: sum of 1662, 2014 and 2466 keV; WD7: sum of 2056, 2327 and 2662 keV; SD1: sum of 1992, 2214, 2439 and 2690 keV; SD2: sum of 2058, 2309, 2565 and 2816 keV; SD3: sum of 2127, 2375, 2616 and 2848 keV; SD4: sum of 1552, 2025, 2315 and 2652 keV;

[b]Taken from or in accordance with published data.

[c]Doublet structure.

[d]Fixed due to a stretched $E2$ cascade.

[e]Based on yrast arguments.

[f]Based on regular rotational structure.

[g]Transitions from data set 2.

states in the bands. Tentative spin and parity assignments to the states near the top of the bands are based on their regular rotational behavior.

A. The normally deformed region

Figure 2 provides the low-spin normally deformed (ND) part of the level scheme. In addition to the known low-spin skeleton marked ND1, ND2, ND3, and ND6, a rather irregular structure ND5, a band-like structure ND4, and a relatively intense extension of the medium-spin ^{62}Zn skeleton (ND7, ND8, ND9) are suggested. The proposed ND parts, i.e. Fig. 2 and the associated first three pages of Table I, are consistent with previous studies [35–38], but extend them noticeably. A brief summary of the results is given below, while a more complete analysis can be found in Ref. [39].

The structures ND1 and ND2 mark the well-estabished positive-parity backbone of the even-even nucleus ^{62}Zn with the yrast and yrare $I = 0, 2, 4, 6\ \hbar$ cascades. ND2 is accompanied by a signature $\alpha = 1$ sequence of $I = 3, 5, 7\ \hbar$ states with $E2$ transitions amongst them and mixed $E2/M1$ transitions connecting to the even-spin states of ND2.

At some 5 MeV excitation energy, the yrast line is taken over by the negative-parity sequence ND3, which comprises nearly degenerate signature $\alpha = 1$ (favored in energy) and signature $\alpha = 0$ (unfavored) sequences up to spin $I = 14\ \hbar$ and $E_x \lesssim 11$ MeV. Hence, in the range $E_x \sim$ 5-9 MeV the γ-ray flux amongst positive-parity states becomes more and more fragmented and rather irregular (ND5). Apart from the 1774-keV, $8^+ \to 6^+$ transition, the relative yield of all such γ-rays is on the level of a percent or less. Here, the 4231-keV, 5^+ state in ND5 is a good example for a definite assignment of spin and parity despite the lack of angular correlation data of both feeding or depopulating transitions; the fact that only a stretched $E2$ 1670-2072-1846-keV γ-ray cascade can connect the known 7976 keV, 9^+ (ND6) and 2385 keV, 3^+ (ND2) levels ensures the 5^+ label of the 4231-keV state.

Both ND1, ND2, ND3, and ND5 connect towards the somewhat more regular positive-parity sequence ND6, which terminates in the yrast 11787-keV, 15^+ (newly observed) and 11961-keV, 16^+ levels. The latter decays via the 1586-1161-keV, $E2$-$E1$ cascade towards the 9214-keV, 13^- yrast state of ND3. These two γ rays mark the end of transitions with relative intensities in excess of 10%. Thus, in particular the 1586-keV $E2$ line is a valuable source for assessing DCO-ratios of many of the weak connections (cf. Figs. 1 and 2) towards the rotational bands. For instance, it is possible to determine a DCO-ratio even for such weak transitions as the 4507-keV line, $R_{DCO} = 0.86(18)$, which in combination with yrast arguments tentatively suggests the state at 16468 keV to have spin-parity of (18^+).

Next to ND6, the previously unobserved three γ-ray transitions at 1506, 1821, and 1902 keV lead to the yrast 17^+ state at 13782 keV, which terminates this ND7 sequence. The DCO-ratios of both the 1821- and 1902-keV lines clearly point at mixed $E2/M1$ character, while the number available for the 1506-keV transition is consistent with a stretched $E2$ assignment. It is also interesting to note that the $\delta(E2/M1)$ mixing ratios for the 1821 and 1902 keV transitions are very similar; either moderate ($\delta \approx 0.3$) or significant ($\delta \approx 2.0$) quadrupole mixture is seen. Similar to the 11961-keV, 16^+ state, the 13782-keV level is also fed by several 3-5 MeV high-energy γ-ray transitions.

The newly identified structure ND4 consists of two signature partner bands of negative parity. At the bottom, ND4 is energetically located some 200-300 keV above the yrast negative-parity cascade ND3, while the more rotational-like behavior of ND4 compared to ND3 leads to an increasing yrare character, manifesting in quickly decreasing yields of the transitions found to belong to ND4. The 7^- spin-parity assignment to the band head of ND4 follows straight from the stretched $E2$ character of the 1080 keV connection to the 4043-keV 5^- state of ND3 and the $\Delta I = 1$ type of the 1417-keV decay into the yrast 6^+ level at 3708 keV (ND1). With the help of the distinct mixed $\Delta I = 1$ character of the 1219-keV transition [$R_{DCO} = 0.31(3)$, $\delta \approx 0.2$ or $\delta \approx 2.0$], 8^- of the 6343-keV level can be easily established. The spin-parity assignments along the band follow the derived DCO-ratios and are based the rotational-like behavior towards the top of ND4.

Several γ-ray cascades lead to the yrast 19^- state at 15705 keV (ND9). The 1260-1633-2437-keV and 1260-2483-1586-keV branches into the yrast 14^+ state at 10375 keV are in accordance with Ref. [20], while the decay paths via the positiv-parity states at 13156, 11546, and 9823 keV into the yrast 11^- level at 7422 keV are newly established (ND8). The DCO-ratios of the 2402-keV, $12^+ \to 11^-$ and 1267-keV, $15^- \to 14^+$ transitions are in agreement with stretched dipole transitions, while the connections of ND8 and ND9 to various other structures of the complete level scheme [cf. Fig. 1] constrain the parities of the concerned states; for example, the plain existence of the 3598-keV $E2$ branch from the 12812-keV state calls for its negative-parity assignment.

B. The terminating bands TB1 and TB2

TB1 and TB2 are previously known [20] terminating band structures. The present results are consistent with the earlier data, but contain more information. More details beyond what is described here are provided in Ref. [39].

In brief, structure TB1 comprises two bands TB1a and TB1b, which are signature partners. The bands consist of about equally intense $E2$ transitions and connecting $E2/M1$ transitions, on the level of some 5% relative yield. The latter all have noticable mixing ratios on the level of $\delta(E2/M1) \sim -0.1$-0.2 (cf. Table I). In Ref. [20], posi-

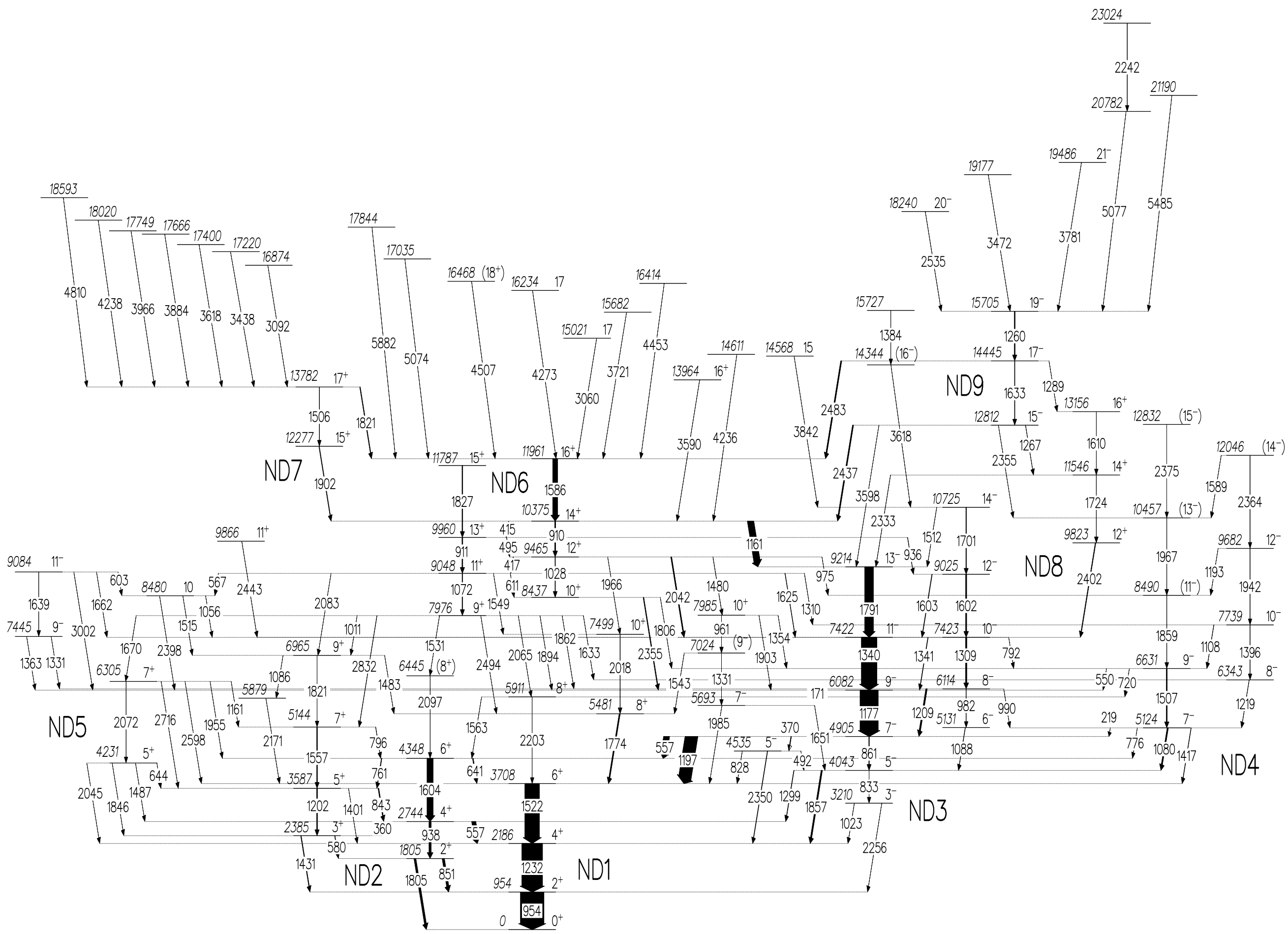

FIG. 2: Normally deformed region of the proposed level scheme of ^{62}Zn. Energy labels are in keV. See text for details.

tive parity was tentatively assigned to the states in TB1. Current results confirm the parity of TB1a and TB1b by several linking transitions, which are connected to the established low-spin region. The fact that the spin $I = 12\,\hbar$ 10631-keV state decays into established 10^+, 11^+, and 11^- states in the ND regime leaves, in conjunction with the DCO ratios of some of the corresponding transitions, only room for a positive-parity assignment. Similarly, the extended decay pattern of the 13^+, 11178-keV level supports this assignment. The maximum spin of TB1 is $I^\pi = 21^+\,\hbar$ at $E_x = 19.5$ MeV for structure TB1a (signature $\alpha = 1$) and $I^\pi = 20^+\,\hbar$ at $E_x = 17.6$ MeV for structure TB1b (signature $\alpha = 0$).

Structure TB2 consists also of two signature partner bands with about equally intense $E2$ transitions inside each signature band and $E2/M1$ transitions between them. Similar to TB1, the relative yield of transitions is on average some 5%, not least because TB2 turns out to be yrast in the spin range $I \sim$ 20-23 $\hbar$. Previously unobserved weak transitions connect TB2 with TB1, and in line with the arguments given above, the complex decay pattern of primarily the $I = 14$ 12329-keV and $I = 15$ 12993-keV states, combined with DCO-ratios of some of the corresponding transitions, leads to a definite negative-parity assignment of TB2 [39]. This assignment is underpinned with the 969-719-914 bypass between TB2 and ND9 as well as the relatively intense 1928-keV $E2$ transition connecting the 16373-keV level in TB2 with the 14445-keV level associated with ND9.

The spin ranges up to $I^\pi = 23^-\,\hbar$ at $E_x = 21.0$ MeV for structure TB2a (signature $\alpha = 1$) and $I^\pi = 24^-\,\hbar$ at $E_x = 23.2$ MeV for structure TB2b (signature $\alpha = 0$). In addition, there are some 15 isolated states observed which, though seemingly not giving rise to any band-like structure, decay into TB2 via high-energy γ-ray transitions in the range $E_\gamma \sim$ 3.4-5.3 MeV.

C. The band WD1

This band has been introduced in Ref. [18]. Signature $\alpha = 0$ and positive parity has been established, with the band covering a spin range of $I =$ 16-30 $\hbar$ and an energy range of $E_x \sim$ 15-34 MeV. Below the 20^+ 18677-keV level, the band forks into several branches and connects mainly towards the 16^+ yrast state at 11961 keV (ND6).

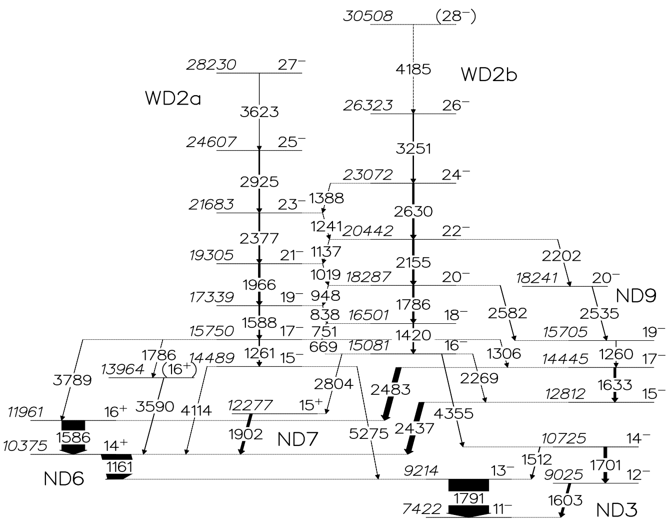

FIG. 3: Decay scheme of band WD2 of the level scheme of ^{62}Zn. Energy labels are in keV and tentative levels and transitions are dashed. The widths of the arrows correspond to the relative intensities of the γ rays.

D. The band WD2

WD2 is the only well-deformed coupled band in the decay scheme of ^{62}Zn. It consists of two signature partner bands illustrated in Fig. 3. The signature $\alpha = 1$ band (WD2a) on the left hand side of Fig. 3 covers the spin range $I = 15$-$27\ \hbar$, and the signature $\alpha = 0$ band (WD2b) $I = 16$-$28\ \hbar$, lying roughly between 15 and 30 MeV excitation energy. The topmost transition in WD2b at 4185 keV is very weak and only tentatively place based on the analysis of the $\gamma\gamma\gamma$ cube.

The relative yields of the in-band quadrupole transitions amount to some 1-2%, while the inter-band dipole transitions are about one order of magnitude less intense. The former are observed with good statistics in the spectra displayed in Fig. 4(a) (WD2a) and 4(b) (WD2b). The most intense dipole connection at 838 keV is highlighted in the inset of Fig. 4(b), which is a γ-ray spectrum in coincidence with the low-lying $E2$ transitions in WD2b (1420 or 1786 keV) and the high-lying $E2$ transitions in WD2a (1966, 2377, or 2925 keV). The $21^- \rightarrow 20^-$ connection at 1018 keV is also weakly seen. Indirect evidence for the dipole connections are the weak but visible peaks at energies corresponding to quadrupole transitions of WD2b in the spectrum focusing on WD2a and vice versa. These are marked with stars in Fig. 4.

WD2 is linked into several parts of the medium-spin level scheme of ^{62}Zn: connections are observed into ND3, ND6, ND7, ND9, as well as a 2519-keV transition between the 15750-keV state in WD2a and the 13231-keV state in TB1 (not included in Fig. 3 for claritity). Starting with WD2a, a rather intense transition at 3789 keV connects the 15750-keV state with the yrast 16^+ state at 11961 keV. The DCO-ratio of this transition points at dipole character, i.e. the level at 15750 keV has spin $I = 17\ \hbar$, likewise the weaker 4114-keV conncetion between the yrast 10375-keV 14^+ state of ND6 and the 14489-keV state in WD2a. Since this state also decays via a 5275-keV γ line into the yrast 13^- level at 9214 keV (ND3), the negative parity assignment to WD2 becomes mandatory. Furthermore, the $E2$ character of the relatively intense 4355-keV link between the lowest state in WD2b and the 10725-keV 14^- level in ND3 confirms the negative-parity assignment.

Coincidences with the 4355-keV transition and any of the four lower members of WD2b are illustrated by the gray spectrum in Fig. 4(b). The WD2b quadrupole transtions up to the 3251-keV line are visible with decreasing yield, but in particular a peak at 1701 keV is

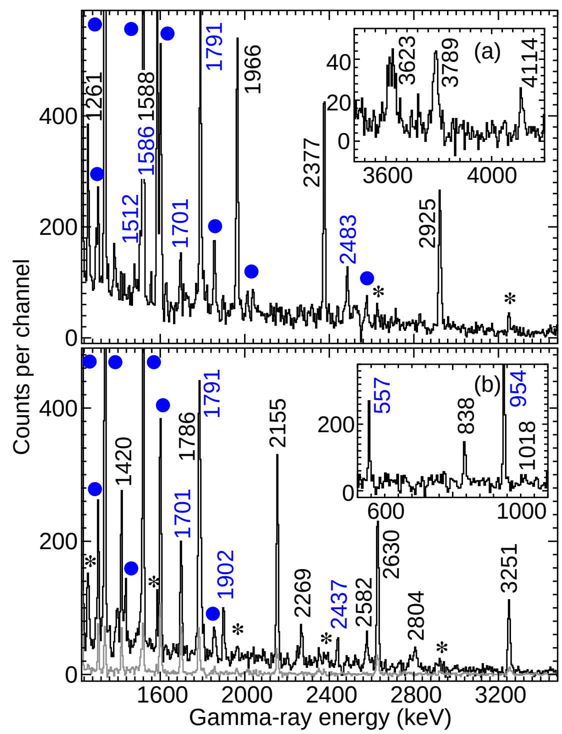

FIG. 4: (Color online) (a) Sum of γ-ray spectra in coincidence with any combination of one of the 1261, 1588, and 1966-keV transitions and one of the 1261, 1588, 1966, 2377, 2925, and 3623-keV transitions placed in WD2a. (b) WD2b is displayed by the sum of γ-ray spectra in coincidence with any combination of one of the 1420, 1786, 2155, and 2630-keV transitions and one of the 1420, 1786, 2155, 2630, and 3251-keV transitions with the spectrum in black. The gray spectrum is in coincidence with one of these four band members and the 4355-keV decay-out transition. The inset shows the low-energy part of a spectrum in coincidence with the 1420 or 1786-keV transitions belonging to WD2b and the 1966, 2377, or 2925-keV transitions placed in WD2a. Energy labels are in keV, and blue labels or filled circles indicate transitions belonging to the ND part of the ^{62}Zn level scheme. The peaks marked with stars indicate quadrupole transitions of WD2b in part (a) and WD2a in part (b). The binning is 4 keV per channel for all spectra.

clearly observed, which corresponds to the $14^- \rightarrow 12^-$ transition in ND3. Together with a similarly clean spectrum of the above mentioned 3789-keV link, both energetic positioning and spin-parity assignments of WD2 are simple. Moreover, the parallel 2804-1902-keV and 2289-2437-keV sequences connect the 15081-keV level in WD2b with the 10375-keV yrast state via levels associated with ND7 and ND9, respectively. The corresponding peaks are clearly seen in Fig. 4(b). Similarly, 2582- and 2202-keV transitions form $E2$ connections between WD2b and ND9.

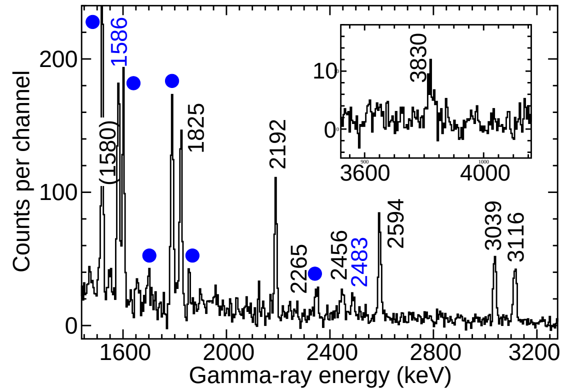

FIG. 6: (Color online) Gamma-ray spectrum in coincidence with any combination of two out of the four main members of the band WD3 at 1825, 2192, 2594, and 3039 keV. The inset shows the high-energy part of the spectrum. Energy labels are in keV, and blue labels or filled circles indicate transitions belonging to the ND part of the ^{62}Zn level scheme. The binning is 4 keV per channel.

E. The band WD3

Figures 5 and 6 show the results of band WD3. A sequence of six $E2$ transitions at 1580 (tentative), 1825, 2192, 2594, 3039 and 3830 keV is observed on top of the 13497-keV state. The relative yield of the central part of WD3 amounts to about 1%. The main and rather intense link at 3116 keV (cf. Fig. 6) connects the 17^- level in WD3 with the 11961-keV 16^+ state in ND6. The $R_{DCO}(3116) = 0.67(7)$ is a clear sign for a $\Delta I = 1$ transition, and due to the 2265- and 2456-keV connections into structure ND9, the 3116-keV line must be a parity changing $E1$ transition, i.e. WD3 has negative parity. The DCO-ratios along the band are consistent with $E2$ character, while the spin-parity assignments of both the lowest and topmost level in WD3 are tentative based on the presumed rotational character.

The spectrum in Fig. 6 illustrates the summed spectra of the coincidences with any combination of the transitions at 1825, 2192, 2594, and 3038 keV. The inset shows an apparent 3830 keV line placed on top of WD3, while a closer inspection reveals a shoulder on the left-hand side of the intense 1586-keV peak (ND6), which is absent in comparable spectra of other well-deformed bands. A tailored $\gamma\gamma\gamma$ analysis gives additional evidence for a tentative line at 1580 keV at the bottom of WD3. Next to other transitions in the lower yrast part of the ND decay scheme of ^{62}Zn (filled circles), the transitions at 2456, 2483, and 3116 keV can be seen, which determine the placement of WD3.

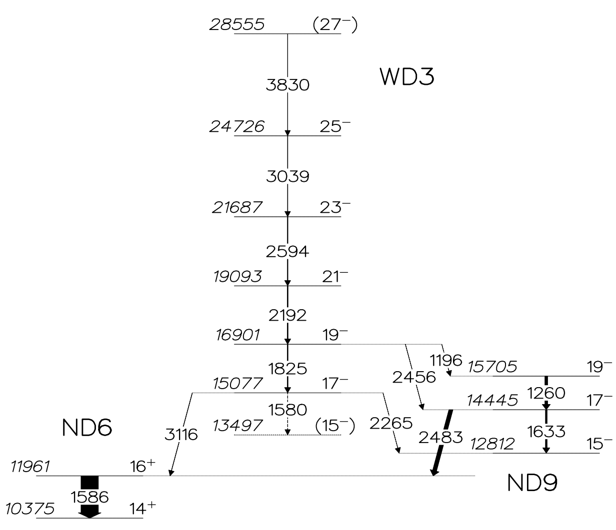

FIG. 5: Decay scheme of band WD3 of the level scheme of ^{62}Zn. Energy labels are in keV and tentative levels and transitions are dashed. The widths of the arrows correspond to the relative intensities of the γ rays.

F. The band WD4

Structure WD4 is illustrated in Figs. 7 and 8. It is formed by a set of states starting from the 19^+ level at 18516 keV to the tentative (27^+) level at 28205 keV. The band decays into the 17^+ state at 13782 keV (ND7) via the 4734-keV linking transition. In combination with yrast considerations, the DCO-ratio of the latter, $R_{DCO}(4734) = 1.20(25)$, defines the spin and parity assignment of the 18516-keV state. Thereafter, the DCO-ratios are consistent with $E2$ character along the band except for the topmost, tentative 3060-keV line.

The γ-ray spectrum in black in Fig. 8 is taken in coincidence with the 4734 keV decay-out transition of WD4. The three band members at 1916, 2136, and 2577 keV are clearly seen, as well as the transitions at 1506, 1586, 1821, and 1902 keV, which define the decay paths of the 13782-keV state of ND7. The blue circles mark transitions further down in the ND yrast decay scheme of ^{62}Zn. With the exception of the 2577-keV line, all corresponding peaks are also seen in the gray spectrum, for which an additional coincidence with one of the above mentioned three WD4 members is required. In fact, the 1506- and 1821-keV lines become relatively more pronounced. Note

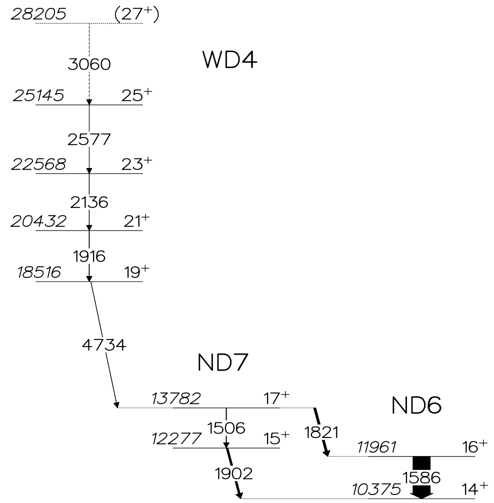

FIG. 7: Decay scheme of band WD4 of the level scheme of ^{62}Zn. Energy labels are in keV and tentative levels and transitions are dashed. The widths of the arrows correspond to the relative intensities of the γ rays.

that the band has a relative yield of some 0.5% and the high-energy link only 0.13%. Nevertheless, Fig. 8 unambiguously determines the WD4 decay path shown in Fig. 7. The transition at 3060 keV can only be added tentatively, based on Fig. 8 and additional studies with the $\gamma\gamma\gamma$ cube. The 4734-keV link is highlighted in the inset of Fig. 8, which is a spectrum in coincidence with one of the three WD4 members and either a second WD4 member or the 1821-keV transition from ND7.

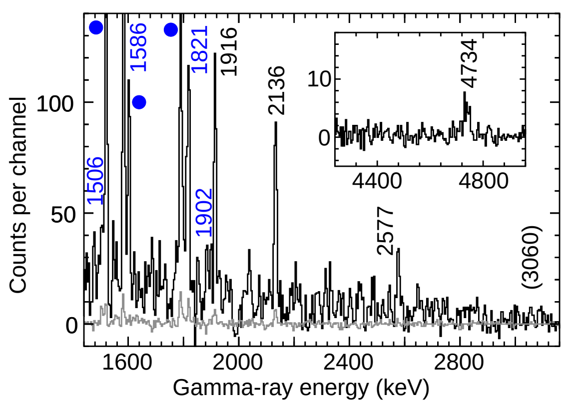

FIG. 8: (Color online) Gamma-ray spectrum in coincidence with the 4734 keV decay-out transition of WD4 (black). The gray spectrum demands an additional coincidence with one of the members of WD4 at 1916, 2136, or 2577 keV. The inset shows the relevant high-energy part of a spectrum in coincidence with one of these three WD4 members and either a second WD4 member or the 1821-keV transition (ND7). Energy labels are in keV, and blue labels or filled circles indicate transitions belonging to the ND part of the ^{62}Zn level scheme. The binning is 4 keV per channel.

G. The bands WD5 and WD6

WD5 is shown on the left hand side of Fig. 9. It is connected to WD6 drawn on the right hand side of the figure. WD5 and WD6 have relative yields of about 0.5% each. Both bands have signature $\alpha = 1$ and are found to carry negative parities. Hence, they interact at their closest approach in energy at around spin $I = 21\ \hbar$.

WD5 consists of a total of four well-defined $E2$ transitions at 1662, 2014, 2466, and 2918 keV, see Fig. 10(a), while the topmost transition at 3583 can only be tentatively suggested. On the contrary, the 4141-keV linking transition is clearly seen in the inset of Fig. 10(a), and its DCO-ratio $R_{DCO}(4141) = 0.51(10)$ is decisive for the spin assignment of both WD5 and WD6. The firm placement of the 4141-keV line between the 11961-keV 16^+ state of ND6 and the bottom state of WD5 at 16102 keV is ensured by the gray spectrum of Fig. 10(a), which is in coincidence with any of the four main WD5 members and the 4141-keV link. Note that the parity of the structure is defined by the existence of the 3134-keV transition as well as the weak side branch via the 19486-keV state into established states of ND9 (cf. Fig. 9).

The spectrum in Fig. 10(a) comprises also the connecting line towards WD6 at 2350 keV and, somewhat less pronounced, the 2786-keV member of WD6. The 3033-keV peak in Fig. 10(a) is set in square brackets; most likely it is a decay-out transition from the 16102-keV level of WD5. Its width is comparable to the 3134-keV peak in Fig. 10(b). However, due to lack of statistics it was not possible to make a firm placement in the decay scheme. The 2871-keV link into TB1 is very weak.

Figure 10(b) is the γ-ray spectrum illustrating WD6.

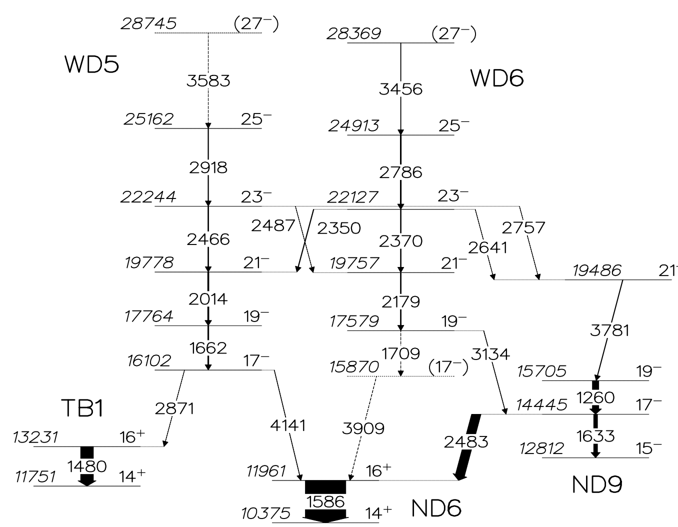

FIG. 9: Decay scheme of bands WD5 and WD6 of the level scheme of ^{62}Zn. Energy labels are in keV and tentative levels and transitions are dashed. The widths of the arrows correspond to the relative intensities of the γ rays.

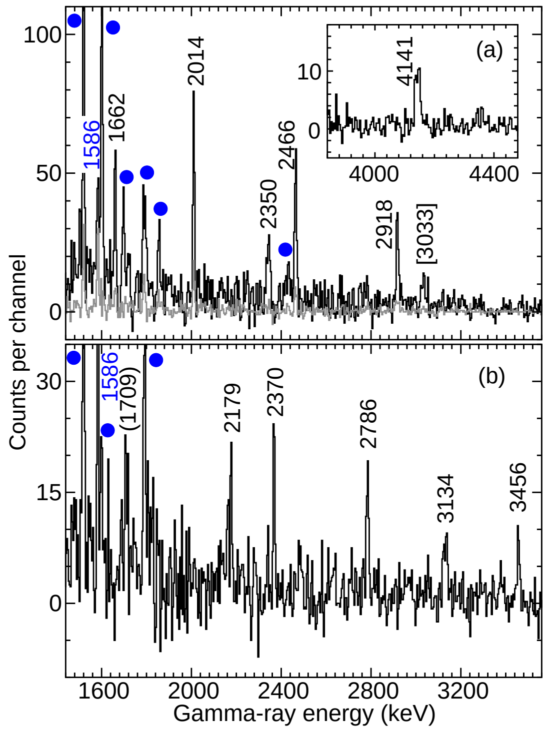

FIG. 10: (Color online) (a) Gamma-ray spectrum in coincidence with any combination of two out of the four main members of the band WD5 at 1662, 2014, 2466, and 2918 keV (black histogram). The inset shows the high-energy part of the spectrum. The gray spectrum is in coincidence with one of these four band members and the 4141-keV linking transition. (b) Gamma-ray spectrum in coincidence with any combination of two out of the three main members of the band WD6 at 2179, 2370, and 2786 keV. Energy labels are in keV, and blue labels or filled circles indicate transitions belonging to the ND part of the ^{62}Zn level scheme. The binning is 4 keV per channel.

It is the sum of coincidences with two out of the three central transitions at 2179, 2370, and 2786 keV. Despite the fact that the 1709-keV peak in Fig. 10(b) is apparent, it is not possible to firmly establish its placement at the bottom of WD6. It carries about half of the yield of the 3134-keV linking transition, the DCO-ratio of which is consistent with the spin and parity assignments of the states in WD5 and WD6.

H. Bands WD7 and WD8

Figure 11 illustrates the details of the decay pattern of bands WD7 and WD8. Both of them are linked into the ND6 yrast 16^+ state at 11961 keV. The weak 5685-keV linking transition of WD7 is shown in the inset of Fig. 12 and further evidenced in the triples analysis: A spectrum in coincidence with both this linking transition and any of the intense γ-ray lines in ND1 and ND3 reveals not only the 1586-keV transition of ND6 but, though weakly, also

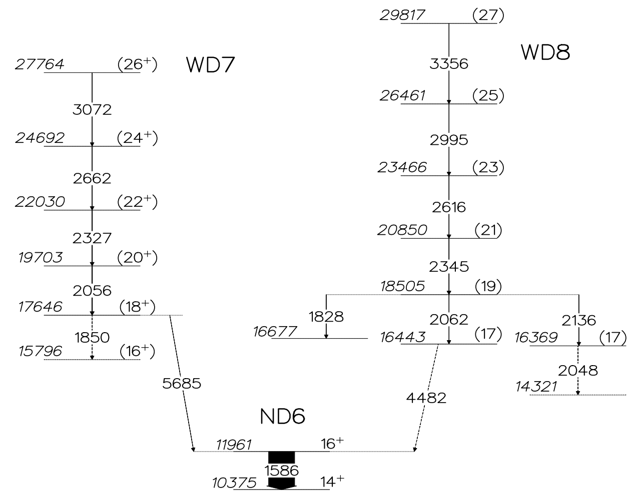

FIG. 11: Decay scheme of bands WD7 and WD8 of the level scheme of ^{62}Zn. Energy labels are in keV and tentative levels and transitions are dashed. The widths of the arrows correspond to the relative intensities of the γ rays.

the 2056 and 2327-keV transitions associated with WD7. The band itself is shown in the main spectrum of Fig. 12. It has about 0.4% relative yield and reaches up to an excitation energy of 28 MeV. Once more, the presence of the 1586-keV line as well as the absence of higher-lying transitions of the ND scheme of ^{62}Zn at, e.g. 2437 or 2483 keV, is obvious. The stars in Fig. 12 mark contaminating transitions arising from the 2058-keV line in SD2. The 1850-keV line is derived from a doublet structure with the 1857-keV $5^- \rightarrow 4^+$ transition but cannot be firmly established due to that. Small peaks at 2378 and 2529 keV can be seen in the spectrum of Fig. 12 as well.

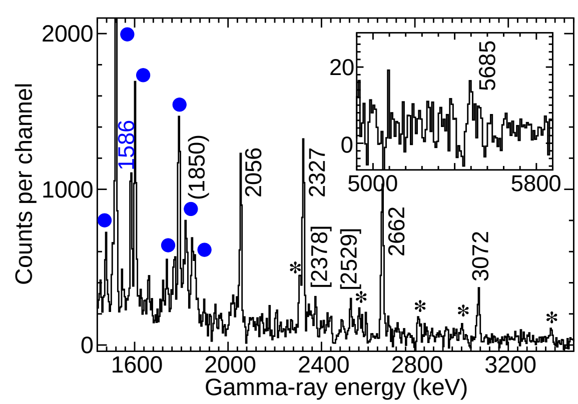

FIG. 12: (Color online) Gamma-ray spectrum in coincidence with the 2056, 2327, 2662, and 3072-keV transitions of WD7. The inset shows the high-energy part of the spectrum. Energy labels are in keV, and blue labels or filled circles indicate transitions belonging to the ND part of the ^{62}Zn level scheme. Stars mark small contaminating peaks arising from the 2058-keV line of SD2. The binning is 4 keV per channel for the main spectrum but 8 keV per channel for the inset.

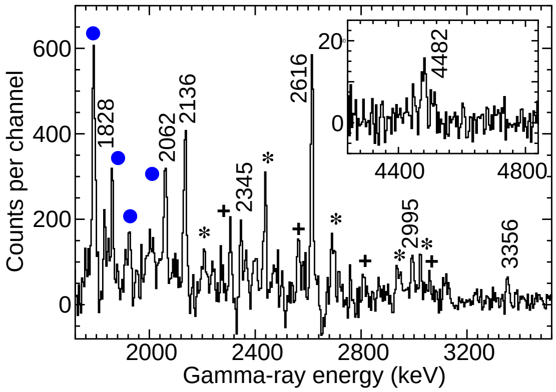

FIG. 13: (Color online) Gamma-ray spectrum in coincidence with the 2345- and 2995-keV transitions of WD8. The inset shows the high-energy part of the spectrum. Energy labels are in keV, and blue labels or filled circles indicate transitions belonging to the ND part of the ^{62}Zn level scheme. Stars mark contaminating peaks arising from unresolved coincidences of a line at 2341 keV with transitions belonging to SD1. Plus signs mark small contaminating peaks arising from the 2994 and 3001-keV decay-out lines of SD2. The binning is 4 keV per channel.

Lack of statistics prevents any firm conclusion on how and where they could be connected to WD7. A tentative spin and parity assignment is suggested based on the high transition energy and yrast arguments. DCO-ratios derived for the 2056-, 2327-, and 2662-keV transitions account for $E2$ character of these band members.

In case of WD8 it is difficult to provide a clean coincidence spectrum with sufficient statistics: The main band members at 2345 and 2616 keV have only 0.3% relative yield. The spectrum displayed in Fig. 13 is taken in coincidence with the 2345- and 2995-keV members of WD8. Along the band, peaks at 1828, 2062, 2136, and 2616 keV are evident, and a weak line at 3356 keV is also apparent. Weak contaminating peaks are present in the spectrum arising from an unresolved doublet structure at 2341 keV (SD1) and decay-out transitions at some 3 MeV associated with SD2. The 4482-keV decay-out transition of WD8 is highlighted in the inset of Fig. 13. Similar to the discussion on WD7 above, this line is confirmed in more detailed steps of the coincidence analysis but also too weak to provide a DCO ratio. Dipole character is proposed due to WD8 intensity-related yrast arguments, i.e. tentatively odd spin values for the band itself up to a spin $I = 27\ \hbar$ level at about 30 MeV excitation energy.

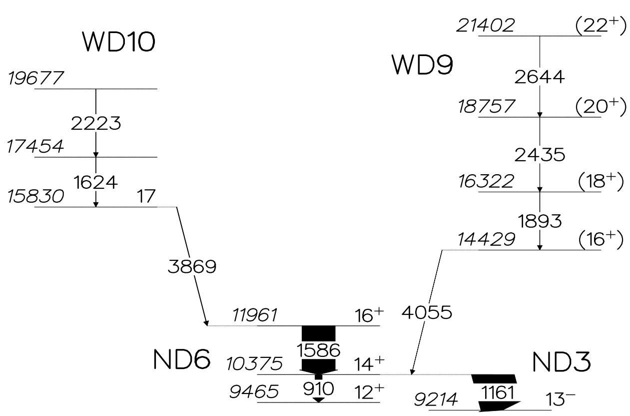

FIG. 14: Decay scheme of bands WD9 and WD10 of the level scheme of ^{62}Zn. Energy labels are in keV. The widths of the arrows correspond to the relative intensities of the γ rays.

I. Bands WD9 and WD10

The relatively short sequences WD9 and WD10 are shown in Fig. 14. WD9 comprises transitions at 1893, 2435, and 2644 keV, which are connected to the 10375-keV 14^+ yrast state (ND6). Despite minor contaminations with doublet transitions at 1891 and 1894 keV, the spectrum in Fig. 15(a) evidences WD9. The spectrum

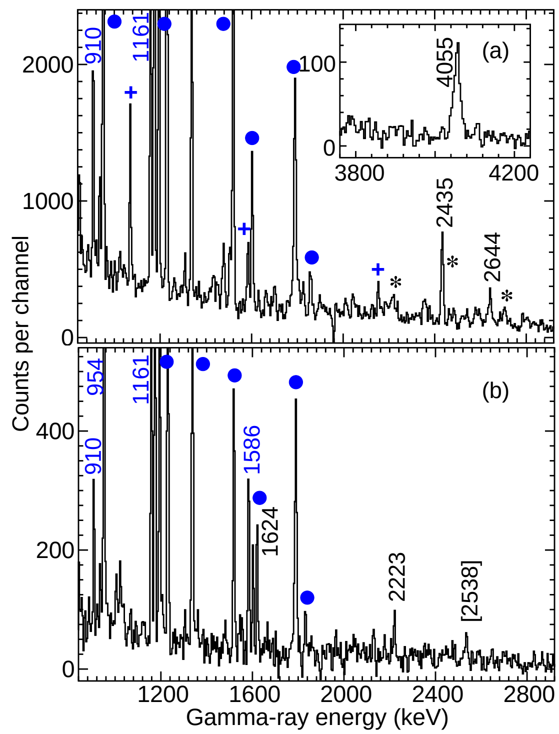

FIG. 15: (Color online) (a) Gamma-ray spectrum in coincidence with the 1893-keV transition of WD9. The inset shows the high-energy part of the spectrum. Blue plus signs mark contaminating peaks arising from a 1894-keV transition connecting the 9^+ state (ND6) with the 9^- level at 6082-keV (ND3). Stars mark small contaminating peaks arising from coincidences with the 1891-keV transition placed in the decay-out regime of SD1. (b) Gamma-ray spectrum in coincidence with the 3869-keV transition linking WD10 into the 16^+ yrast state (ND6). Energy labels are always in keV, and blue labels or filled circles indicate transitions belonging to the ND part of the ^{62}Zn level scheme. The binning is 4 keV per channel.

in coincidence with the 1893-keV line provides a clean and rather intense peak at 4055 keV, the DCO-ratio of which is consistent with stretched $E2$ character. This implies that WD9 has tentatively even spins and positive parity. The 2435 and 2644-keV transitions are also visible in Fig. 15(a) with decreasing yield. A more detailed $\gamma\gamma\gamma$ analysis involving transitions from the ND part of the level scheme in conjunction with the relatively intense 4055-keV link does unfortunately not provide any evidence for further transitions or connections to other deformed bands.

WD10 is illustrated in Fig. 15(b). The spectrum taken in coincidence with the 3869-keV link into the 16^+ yrast state of ND6 provides the relevant peaks at 910, 1161, and 1586 keV as well as the two band members at 1624 and 2223 keV, respectively. The transition belonging to the weak additional peak at 2538 keV may feed into the lowest level of WD10 at 15830 keV, since it is neither coincident with the 1624 nor the 2223 keV transition. The DCO-ratio of the 3869-keV line is clearly consistent with stretched dipole character. Hence, the 15830-keV state of WD10 has spin $I = 17\ \hbar$. The low yield of the band members or contaminating lines from other parts of the ^{62}Zn level scheme prevent any DCO-ratio measurements of the in-band transitions of WD9 and WD10.

J. The superdeformed bands SD1, SD2, and SD3

Apart from some minor adjustments of transition energies and intensities and in parts a few more transitions in the respective decay-out regime, the presentation of the superdeformed bands SD1, SD2, and SD3 is in accordance with Figs. 1-3 in Ref. [18]. SD1 has negative parity assigned and covers the spin range of $I = 18$-$34\ \hbar$ with maximum excitation in excess of 40 MeV. A comparatively extensive decay-out regime is established, likewise a forking at the very top with two parallel high-energy transitions at 3958 keV [18] and 4234 keV, respectively. SD2 is considered the $\alpha = 1$ signature partner of SD1 [18], involves a record-high discrete-energy state at 42.5 MeV excitation energy, and lies amongst the fastest rotating nuclei. SD2 is found to interact with a new, parallel sequence SD5 (see below). SD3 has signature $\alpha = 0$, positive parity, and spin values $I = 16$-30, and remains unchanged with respect to the previous publication [18].

K. The superdeformed bands SD4 and SD5

One more superdeformed structure labeled SD4 has been derived from data set 1. Furthermore, a sequence of levels interacting with the central section of SD2 could be observed, which is denoted SD5. The respective part of the high-spin level scheme of ^{62}Zn is shown in Fig. 16.

SD4 comprises a sequence of six (tentative) quadrupole

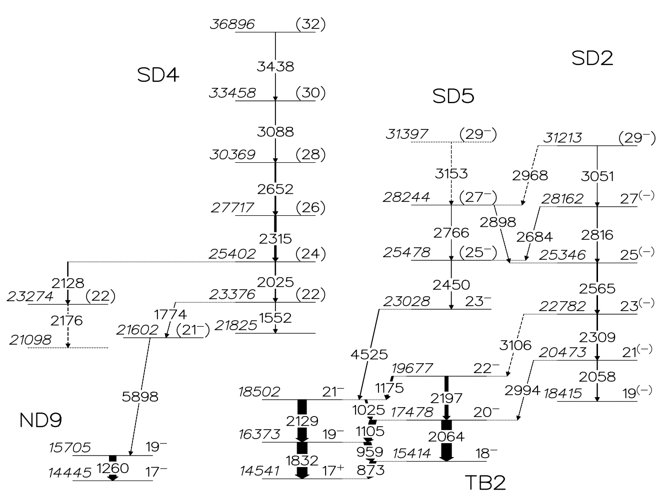

FIG. 16: Decay scheme of the superdeformed bands SD49 and SD5 of the level scheme of ^{62}Zn. Energy labels are in keV and tentative levels and transitions are dashed. The widths of the arrows correspond to the relative intensities of the γ rays.

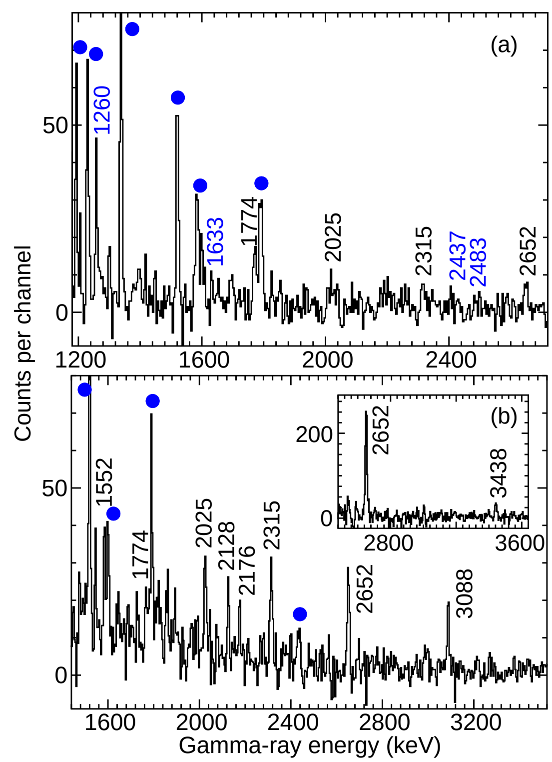

FIG. 17: (Color online) (a) Gamma-ray spectrum in coincidence with the 5898-keV decay-out transition of SD4. (b) Gamma-ray spectrum in coincidence with any combination of two out of the four main members of the band SD4 at 2025, 2315, 2652, and 3088 keV. The inset shows a portion of the spectrum in coincidence with the 3088-keV transition. Energy labels are in keV. Blue labels and filled circles mark transitions belonging to the ND part of the ^{62}Zn level scheme. The binning is 4 keV per channel.

transitions ranging from 1552 to 3438 keV. The two lowest transitions are paralleled with a 2176-2128-keV sequence, and the level at 23378-keV decay via a 1774-5898-keV cascade into the yrast 19^- state at 15705 keV in ND9. Based on yrast arguments, the nearly 6-MeV link is suggested to have quadrupole character, while the DCO-ratio measured for the transition at 1774 keV indicated dipole character. SD4 thus is associated with even-spin values in the range I = 20-32 $\hbar$ and excitation energies up to 37 MeV. The DCO-ratios of the four central transitions of SD4 are consistent with $E2$ character. Note that different from the previously published SD bands it has not been possible to add any transition on top of SD4 by investigating data set 2.

Figure 17 provides two γ-ray spectra considered relevant for the decay pattern of SD4. The spectrum in Fig. 17(a) is in coincidence with the 5898-keV linking transition. Besides intense peaks at, for example, 1197, 1232, 1340, or 1522 keV, Fig. 17(a) shows a distinct peak at 1260 keV, which marks the feeding into the already mentioned yrast 19^- state at 15705 keV in ND9, not least in conjunction with the weaker lines at 1633, 2437, and 2483 keV seen in that spectrum as well. Additionally, the lowest transitions towards and in SD4 are also observed at 1774, 2025, 2315, and 2652 keV with anticipated decreasing yield. The 1552-keV transition at the bottom of SD4, the 2128-2176-keV side branch, and the 3088- and topmost 3438-keV transitions are evidenced in the spectra displayed in Fig. 17(b): The main body of that spectrum is in coincidence with various combinations of transitions in SD4, while the inset shows a spectrum in coincidence with solely the 3088 keV transition. Here, the peaks for both the coincident feeding and depopulating transitions at 3438 and 2652 keV, respectively, can be seen.

Finally, Fig. 18 focuses on the newly observed band SD5, which is intimately related to the known SD2.

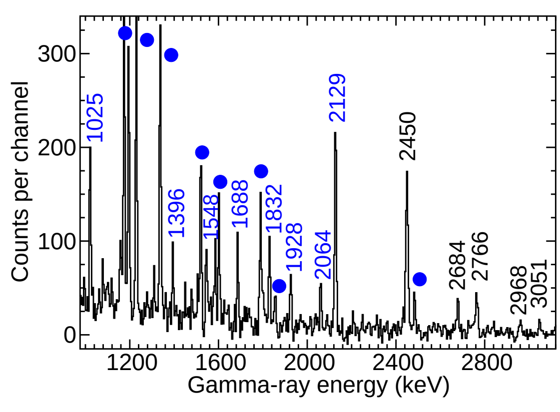

FIG. 18: (Color online) Gamma-ray spectrum in coincidence with the 4525-keV decay-out transition of SD5. Energy labels are in keV. Blue labels mark transitions associated with TB2 and blue filled circles mark transitions belonging to the ND part of the ^{62}Zn level scheme. The binning is 4 keV per channel.

Building on the 4525-keV $E2$ transition, which feeds the 21^- state at 18502 keV in TB2, transitions at 2450 2684, 2766, 2968, and 3051 keV are observed in coincidence with it. Lines at 2450, 2766, and (tentatively) 3153 keV form the in-band sequence of SD5, while the 2684- and 2968-keV transitions connect from SD2 into SD5. This is evidenced not only by the 3051-keV transition belonging to SD2, but also the corresponding 2898-keV transition, which forms the connection from SD5 into SD2 in the crossing regime at spin $I \sim$ 25-27 $\hbar$ (cf. Fig. 3(a) of Ref. [18]).

IV. DISCUSSION

V. SUMMARY

Acknowledgements

[1] I.-Y. Lee, Nucl. Phys. **A520**, 641c (1990).
[2] D.G. Sarantites *et al.*, Nucl. Instrum. Meth. **A381**, 418 (1996).
[3] D. Rudolph *et al.*, Phys. Rev. Lett. **80**, 3018 (1998).
[4] D. Rudolph *et al.*, Phys. Rev. Lett. **86**, 1450 (2001).
[5] D. Rudolph *et al.*, Phys. Rev. Lett. **82**, 3763 (1999).
[6] E.K. Johansson *et al.*, Phys. Rev. C **77**, 064316 (2008).
[7] C.-H. Yu *et al.*, Phys. Rev. C **60**, 031305(R) (1999).
[8] W. Satula, J. Dobaczewski, W. Nazarewicz, and M. Rafalski, Phys. Rev. C **81**, 054310 (2010).
[9] D. Rudolph *et al.*, Phys. Rev. Lett. **96**, 092501 (2006).
[10] C. Andreoiu *et al.*, Eur.Phys. J. A**14**, 317 (2002).
[11] E.K. Johansson *et al.*, Phys. Rev. C **80**, 014321 (2009).
[12] D. Rudolph *et al.*, J. Phys. G**37**, 075105 (2010).
[13] C. Andreoiu *et al.*, Phys. Rev. Lett. **91**, 232502 (2003).
[14] L.-L. Andersson *et al.*, Eur. Phys. J. A**36**, 251 (2008).
[15] C.E. Svensson *et al.*, Phys. Rev. Lett. **82**, 3400 (1999).
[16] L.-L. Andersson *et al.*, Phys. Rev. C **79**, 024312 (2009).
[17] C.E. Svensson *et al.*, Phys. Rev. Lett. **79**, 1233 (1997).
[18] J. Gellanki *et al.*, Phys. Rev. C **80**, 051304(R) (2009).
[19] J. Ekman *et al.*, Phys. Rev. C **66**, 051301(R) (2002).
[20] C.E. Svensson *et al.*, Phys. Rev. Lett. **80**, 2558 (1998).
[21] C.E. Svensson *et al.*, Phys. Lett. B**422**, 45 (1998).
[22] D.A. Torres *et al.*,Phys. Rev. C **78**,054318 (2008).
[23] D. Karlgren *et al.*, Phys. Rev. C **69**, 034330 (2004).
[24] C. Andreoiu *et al.*, Phys. Rev. C **62**, 051301(R) (2000).
[25] D. Rudolph *et al.*, Eur. Phys. J. A**14**, 137(2002).
[26] M. Devlin *et al.*, Nucl. Instrum. Meth. **A383**, 506 (1996).
[27] C.E. Svensson *et al.*, Nucl. Instrum. Meth. **A396**, 288 (1997).
[28] D. Seweryniak *et al.*, Nucl. Instrum. Meth. **A340**, 353 (1994).
[29] D.C. Radford, Nucl. Instrum. Meth. **A361**, 297 (1995).
[30] J. Theuerkauf, S. Esser, S. Krink, M. Luig, N. Nicolay, O. Stuch, H. Wolters, Program Tv, University of Cologne, unpublished.
[31] K.S. Krane, R.M. Steffen, and R.M. Wheeler, At. Data Nucl. Data Tables **11**, 351 (1973).
[32] M.K. Kabadiyski, K.P. Lieb, and D. Rudolph, Nucl. Phys. **A563**, 301 (1993).
[33] D. Rudolph *et al.*, Eur. Phys. J. A**4**, 115 (1999).
[34] H.J. Rose and D.M. Brink, Rev. Mod. Phys. **39**, 306 (1967).
[35] J.F. Bruandet, Tsan Ung Chan, M. Agard, J.P. Longequeue, C. Morand, and A. Giorni, Z. Phys. **A 279**, 69 (1976).
[36] L. Mulligan, R.W. Zurmühle, and D.P. Balamuth, Phys. Rev. C **19**, 1295 (1979).
[37] N.J. Ward, L.P. Ekström, G.D. Jones, F. Kearns, T.P. Morrison, O.M. Mustaffa, D.N. Simister, P.J. Twin, and R. Wadsworth, J. Phys. G**7**, 815 (1981).
[38] K. Furutaka *et al.*, Z. Phys. **A 358**, 279 (1997).
[39] J. Gellanki, Licentiate thesis, Lund University, LU-XXX (2011).